

# Bistatic High Frequency Radar Ocean Surface Cross Section for an Antenna on a Floating Platform

by

©Yue Ma, B. Eng., M. Eng.

A thesis submitted to the  
School of Graduate Studies  
in partial fulfilment of the  
requirements for the degree of  
Doctor of Philosophy

Faculty of Engineering and Applied Science  
Memorial University of Newfoundland

October 2017

St. John's

Newfoundland

# Abstract

Land-based high frequency surface wave radar (HFSWR) is an established sensor for ocean remote sensing. Placing an HFSWR on a floating platform has the advantage of mobility. However, antenna motion will distort the Doppler spectrum, which is used to extract ocean information and to detect the signatures of targets. In this thesis, significant effort has been expended on establishing radar cross section (RCS) models for a fixed receiver and a transmitter on a floating platform, analyzing the effect of the antenna motion, and developing a motion compensation method to eliminate the effect of the platform motion.

The first- and second-order monostatic RCSs of the ocean surface for the case of a pulsed dipole source on a floating platform have been previously derived in the literature, with the assumption that the platform motion is a single-frequency sinusoid. Following that work, the research in this thesis is extended to the bistatic case. The effect of platform motion on simulated Doppler spectra is considered for a variety of sea states. It is shown that the resulting motion-induced peaks are symmetrically distributed in the Doppler spectrum.

Following this work, the corresponding bistatic RCS models for a frequency modulated continuous waveform (FMCW) source are derived. Results show that the sidelobe level for an FMCW source is reduced with increasing extent of range bin.

To mimic real world scenarios, platform motion is next modelled as a combination of two cosine functions, based on existing research of realistic horizontal motions of moored floating platforms. RCSs incorporating a dual-frequency platform motion model are then developed. These can be extended to a general form incorporating a multi-frequency platform motion. It is found that the platform motion can be viewed as a modulator of the radar frequencies, with the modulation indices related to the amplitudes of the platform motion.

Finally, to mitigate the effect of platform motion on the Doppler spectra, a motion compensation method is proposed. This motion compensation method can be achieved by a deconvolution process. Calculations involving a RCS model, incorporating external noise, for an antenna on a floating platform are conducted in order to simulate field data and to examine this motion compensation method. The external noise is characterized as a white Gaussian zero-mean process. By using this newly-developed RCS model with external noise, motion compensation results under different sea states and signal-to-noise ratios (SNRs) are examined. The outcomes indicate that an iterative Tikhonov regularized deconvolution technique is superior to other compensation methods implemented in this study.

## Acknowledgements

Four years of PhD life has been a challenging journey to me, one filled with joy, sadness, excitement, and sometimes depression and confusion. At the end of my PhD, I would like to show my sincere gratitude to all of you for accompanying and helping me in my PhD journey.

Foremost, I would like to express my deepest gratitude to my supervisors, Dr. Eric Gill and Dr. Weimin Huang for their professional guidance and continuous encouragement in my research. Their attitude and enthusiasm to the research inspired me and helped me to overcome the difficulties in my research. They always taught me to read the original papers and care about all the detailed parts. They showed their patience and encouragement to me when I did poor work. They helped me grow up in many aspects, for example, in research, language and life. I feel greatly fortunate and honored to be a member of their group. I also appreciate them for their continuous support for my life. My work was supported in part by Natural Sciences and Engineering Research Council of Canada (NSERC) under Discovery Grants to W. Huang (NSERC 402313-2012, RGPIN-2017-04508 and RGPAS-2017-507962) and E. W. Gill (NSERC 238263-2010 and RGPIN-2015-05289) and by an Atlantic Innovation Fund Award (E. W. Gill, principal investigator). Next, I would like to show my thanks to my supervisory committee member, Dr. Cecilia Moloney, for giving me many valuable suggestions and comments on my research. Further, I honour the memory of Dr. John Walsh for his outstanding contribution to HF radar ocean remote sensing. My radar cross section models are developed based on his theoretical foundations. His work has given me the direction for my research.

Next, I would like to thank all the members of our radar group for giving me much good advice, helping and encouraging me to further explore this area. Also, I want to thank all the friends I met in St. John's, who accompanied me, played with me and brought a lot of joy to me.

Finally, thanks to my family for their love and support in my whole life. I miss you so much. Also thanks to my boyfriend, Xinlong Liu.

# Contents

<b>Abstract</b>	<b>ii</b>
<b>Acknowledgements</b>	<b>iv</b>
<b>List of Figures</b>	<b>x</b>
<b>List of Tables</b>	<b>xv</b>
<b>List of Symbols</b>	<b>xvi</b>
<b>1 Introduction</b>	<b>1</b>
1.1 Research Rationale . . . . .	1
1.2 Literature Review . . . . .	3
1.2.1 Radar Cross Section Models for an Antenna on a Floating Platform	3
1.2.2 Analysis of the Effect of the Platform Motion and Platform Motion Compensation Methods . . . . .	6
1.2.3 Walsh’s Scattering Theory and Monostatic Radar Cross Section Models . . . . .	10
1.3 The Scope of the Thesis . . . . .	18
<b>2 Bistatic Radar Cross Section for a Pulsed Source with an Antenna on a     Floating Platform</b>	<b>21</b>
2.1 Introduction . . . . .	21

2.2	The First-Order Radar Cross Section Model . . . . .	23
2.3	The Second-Order Radar Cross Section Model . . . . .	30
2.3.1	The Second-Order Hydrodynamic Contribution . . . . .	30
2.3.2	The Second-Order Electromagnetic Contribution . . . . .	31
2.3.3	Second-Order Radar Cross Section For Patch Scatter . . . . .	35
2.4	Comparisons of Antenna-Motion Incorporated Bistatic Radar Cross Sections with Earlier Models . . . . .	37
2.5	Simulation and Analysis . . . . .	41
2.6	Chapter Summary . . . . .	50
<b>3</b>	<b>Bistatic Radar Cross Section for an FMCW Source with an Antenna on a Floating Platform</b>	<b>53</b>
3.1	Introduction . . . . .	53
3.2	Radar Received Field Equations – FMCW source . . . . .	54
3.2.1	General First- and Second-Order Electric Field Equation . . . . .	54
3.2.2	Applications to an FMCW Radar . . . . .	55
3.3	Radar Cross Sections for an FMCW Source . . . . .	59
3.3.1	First-Order Radar Cross Section . . . . .	59
3.3.2	Second-Order Radar Cross Section . . . . .	60
3.4	Simulation and Analysis . . . . .	61
3.4.1	First-Order Radar Cross Section . . . . .	61
3.4.2	Second-Order Radar Cross Section . . . . .	64
3.5	Chapter Summary . . . . .	66
<b>4</b>	<b>Generalized Radar Cross Section Models with a More Realistic Platform Motion Model</b>	<b>68</b>
4.1	Introduction . . . . .	68
4.2	A More Realistic Platform Motion Model . . . . .	69

4.3	Monostatic Radar Cross Sections for a Platform Motion Model Incorporating Dual-Frequency and Single Direction . . . . .	70
4.3.1	The First-Order Radar Cross Section Model . . . . .	71
4.3.2	The Second-Order Radar Cross Section Model . . . . .	75
4.4	Bistatic Radar Cross Sections for a Platform Motion Model Incorporating Dual-Frequency and Single Direction . . . . .	75
4.4.1	The First-Order Radar Cross Section Model . . . . .	76
4.4.2	The Second-Order Radar Cross Section Model . . . . .	78
4.5	Radar Cross Sections for a More Complicated Platform Motion Model .	78
4.5.1	Platform Motion Model Having Multiple Frequencies . . . . .	78
4.5.2	Platform Motion Model Incorporating Surge and Sway Directions	79
4.6	Simulation and Analysis . . . . .	80
4.7	Chapter Summary . . . . .	93
<b>5</b>	<b>Motion Compensation for High Frequency Surface Wave Radar on a Floating Platform</b>	<b>95</b>
5.1	Introduction . . . . .	95
5.2	Radar Cross Sections . . . . .	96
5.3	Platform Motion Compensation Method . . . . .	96
5.4	Deconvolution Techniques . . . . .	99
5.4.1	Division in the Time Domain . . . . .	99
5.4.2	Transformation Matrix . . . . .	99
5.4.3	Tikhonov Regularization . . . . .	101
5.4.4	Iterative Tikhonov Regularization . . . . .	102
5.5	Radar Cross Sections with External Noise . . . . .	102
5.6	Examples of Motion Compensation Results . . . . .	104
5.7	Chapter Summary . . . . .	116

<b>6 Conclusion</b>	<b>118</b>
6.1 Summary . . . . .	118
6.2 Suggestions for Future Work . . . . .	122
<b>References</b>	<b>124</b>
<b>Appendix A A Stationary Phase Process for the First-Order Electric Field</b>	<b>135</b>
<b>Appendix B <math>\langle M(K, \theta_K, \tau, t) \rangle</math> for a Sinusoidal Antenna Motion Model</b>	<b>139</b>
<b>Appendix C A Stationary Phase Process for the Second-Order Electric Field</b>	<b>141</b>
<b>Appendix D Symmetrical Coupling Coefficient</b>	<b>144</b>

# List of Figures

1.1	The RCS derivation process block diagram. . . . .	12
1.2	General first-order bistatic scatter geometry including antenna motion. . .	13
1.3	General second-order bistatic scatter geometry with antenna motion. . .	17
2.1	A diagram of bistatic scatter for a fixed receiver and a transmitter on a floating platform. . . . .	22
2.2	Comparison of the first-order bistatic radar cross section for both transmitter and receiver fixed with that for a floating transmitter and a fixed receiver. . . . .	42
2.3	The effect of radial patch width on the first-order cross section. The patch width is (a) 2000 m, (b) 1000 m, (c) 500 m, (d) 250 m. . . . .	43
2.4	(a) The second-order bistatic hydrodynamic contribution without antenna motion. (b) The second-order hydrodynamic contribution with antenna motion. (c) The second-order electromagnetic contribution without antenna motion. (d) The second-order electromagnetic contribution with antenna motion. (e) The total bistatic radar cross section without antenna motion. (f) The total bistatic radar cross section with antenna motion. . .	45
2.5	Comparison of the total bistatic radar cross section for both transmitter and receiver fixed with that for a floating transmitter and a fixed receiver. . .	46

2.6	Comparison of the radar cross sections with floating platform for the monostatic case and for the bistatic case with bistatic angle of $30^\circ$ . Wind direction is $180^\circ$ , ellipse normal $\theta_N = 90^\circ$ for bistatic geometry and look direction $\theta_L = 60^\circ$ for monostatic geometry. . . . .	47
2.7	The effect of wind speed on bistatic radar cross section with floating transmitter and fixed receiver. The wind speed is (a) 20 knots, (b) 15 knots, (c) 10 knots. . . . .	48
2.8	The effect of wind direction on bistatic radar cross section with floating transmitter and fixed receiver. The wind direction is (a) $45^\circ$ , (b) $90^\circ$ , (c) $135^\circ$ , (d) $180^\circ$ , (e) $225^\circ$ , (f) $270^\circ$ with respect to the positive $x$ axis. The ellipse normal is $90^\circ$ with respect to the positive $x$ axis. . . . .	49
2.9	The effect of radar frequency on bistatic radar cross section with floating transmitter and fixed receiver. The radar frequency is (a) 25 MHz, (b) 15 MHz, (c) 7 MHz. . . . .	51
3.1	Comparison of the first-order radar cross sections for the FMCW waveform with that for the pulsed waveform. . . . .	62
3.2	Comparison of the sidelobe levels of the first-order radar cross sections for the pulsed and FMCW waveform. (a) $\Delta r = 0.5\Delta\rho$ and (b) $\Delta r = 10\Delta\rho$ . . . . .	64
3.3	The effect of the bandwidth on the first-order radar cross sections. . . . .	65
3.4	Second-order bistatic radar cross section with a transmitter on a floating platform. . . . .	66
4.1	Comparison of the first-order radar cross sections under a moderate sea state of $H_s = 2.06$ m (see text for other model parameters) for a fixed antenna with those for a floating antenna, respectively, incorporating a dual-frequency platform motion and (a) a single wave frequency platform motion; (b) a single low frequency platform motion. . . . .	82

4.2	Zoomed-in view of the positive Doppler spectrum (a) in Fig. 4.1(a); (b) in Fig. 4.1(b). . . . .	83
4.3	Comparison of the first-order positive Doppler spectra under an extremely high sea state of $H_s = 15.7$ m for a fixed antenna with that for a floating antenna. . . . .	85
4.4	Comparison of the total (including the first- and second-order) radar cross sections under a moderate sea state of $H_s = 2.06$ m for a fixed antenna with that for a floating antenna. . . . .	86
4.5	Comparison of the total radar cross sections under an extremely high sea state of $H_s = 15.7$ m for a fixed antenna with that for a floating antenna. . . . .	87
4.6	Comparison of the total radar cross sections incorporating a multi-frequency platform motion model under a moderate sea state 3 of $H_s = 2.06$ m for a fixed antenna with that for a floating antenna. . . . .	88
4.7	Comparison of the total radar cross sections considering both surge and sway directions under a moderate sea state 3 of $H_s = 2.06$ m for a fixed antenna with that for a floating antenna. . . . .	89
4.8	Comparison of bistatic radar cross sections under a high sea state of $H_s = 8$ m for a fixed antenna with that for a floating antenna. . . . .	90
4.9	Zoomed-in view of the negative Doppler spectrum in Fig. 4.8. . . . .	91
4.10	Comparison of bistatic radar cross sections for different bistatic angles with the platform motion direction of $0^\circ$ under environmental conditions associated with sea state 11. . . . .	92
4.11	Comparison of bistatic radar cross sections for different bistatic angles with the platform motion direction of $90^\circ$ under environmental conditions associated with sea state 11. . . . .	93

5.1	The squared values of sampling function and the Bessel functions with respect to $K$ . The radar operating frequency is 10 MHz, the platform motion amplitude is 5 m, and the motion direction is the same with the radar look direction. . . . .	97
5.2	A combined sea clutter and external noise Doppler spectrum. The radar operating frequency is 10 MHz with SNR = 60 dB. . . . .	105
5.3	An example of the platform motion compensation results for a single-frequency motion model having an amplitude of 1.228 m and a radian frequency of 0.127 Hz. (a) Comparison of the Doppler spectrum before compensation with that after compensation (b) A zoomed-in view of (a). . . . .	107
5.4	An example of the platform motion compensation results for a dual-frequency motion model having amplitudes of 2 m and 0.9 m, and radian frequencies of 0.05 rad/s and 0.63 rad/s, respectively. (a) Comparison of the Doppler spectrum before compensation with that after compensation (b) A zoomed-in view of (a). . . . .	108
5.5	An example of the platform motion compensation results for a dual-frequency motion model having amplitudes of 5.5 m and 0.4 m, and radian frequencies of 0.02 rad/s and 0.38 rad/s, respectively. This result is for an ill-conditioned transformation matrix by using the deconvolution technique A or B in Section 5.4. . . . .	109
5.6	An example of the platform motion compensation results for a dual-frequency motion model having amplitudes of 5.5 m and 0.4 m, and radian frequencies of 0.02 rad/s and 0.38 rad/s, respectively. This result is for an ill-conditioned transformation matrix by using the deconvolution technique of Tikhonov regularization. (a) Comparison of the Doppler spectrum before compensation with that after compensation (b) A zoomed-in view of (a). . . . .	110

5.7	An example of the platform motion compensation results for a dual-frequency motion model having amplitudes of 5.5 m and 0.4 m, and radian frequencies of 0.02 rad/s and 0.38 rad/s, respectively. This result is for an ill-conditioned transformation matrix by using the deconvolution technique D in Section 5.4. (a) Comparison of the Doppler spectrum before compensation with that after compensation (b) A zoomed-in view of (a). . . . .	113
5.8	An example of the platform motion compensation results for a dual-frequency motion model having amplitudes of 10 m and 5 m, and radian frequencies of 0.08 rad/s and 0.63 rad/s, respectively. (a) Comparison of the Doppler spectrum before compensation with that after compensation; (b) A zoomed-in view of (a); (c) Comparison of the compensation result with the Doppler spectrum for a fixed antenna. . . . .	115
A.1	Depiction of the bistatic geometry associated with stationary phase condition. . . . .	135

# List of Tables

2.1	Barge motion parameters [17] . . . . .	42
4.1	The radian frequencies and relative amplitudes of Bragg peaks and motion-induced peaks . . . . .	84
5.1	Radar system parameters [84] . . . . .	104
5.2	Root-mean-square differences between the “after compensation” and “fixed” cases in Figs. 5.3- 5.8 . . . . .	116

# List of Symbols

The page numbers here indicate the place of first significant reference. Only important symbols are explicitly referenced below, and all the symbol definitions are obvious from the context.

$E_n$  electric field in the normal direction (p. 12)

$\xi$  the rough surface (p. 12)

$\delta\vec{\rho}_0$  the transmitter displacement vector with  $\delta\rho_0$  and  $\theta_0$ , respectively, being the magnitude and the direction of  $\delta\vec{\rho}_0$  (p. 12)

$\rho$  planar distance from the transmitter to the receiver (p. 12)

$\rho'$  planar distance from the transmitter to the receiver including the displacement vector  $\delta\vec{\rho}_0$  (p. 12)

$\hat{\rho}$  a unit vector in the direction of  $\vec{\rho}$  (p. 13)

$C_0 = \frac{I\Delta l k^2}{j\omega\epsilon_0}$  the dipole constant (p. 13)

$\Delta l$  the length of a vertical dipole (p. 13)

$I$  the current of a vertical dipole (p. 13)

$\omega$  the radian frequency of a vertical dipole (p. 13)

$k$  the wavenumber of a vertical dipole (p. 13)

- $\epsilon_0$  the space permittivity for free space (p. 13)
- $\overset{xy}{*}$  a two-dimensional spatial convolution (p. 13)
- $F(\rho)$  the Sommerfeld attenuation function (p. 13)
- $\nabla = \hat{x} \frac{\partial}{\partial x} + \hat{y} \frac{\partial}{\partial y} + \hat{z} \frac{\partial}{\partial z}$  (p. 13)
- $j = \sqrt{-1}$  (p. 13)
- $P_{\vec{K}}$  Fourier coefficient of the rough surface (p. 13)
- $\vec{K}$  surface wave vector with  $K$  and  $\theta_K$ , respectively, being the magnitude and the direction of  $\vec{K}$  (p. 13)
- $\Sigma$  the summation symbol (p. 13)
- $I_0$  the peak current of the pulsed dipole (p. 14)
- $\omega_0$  the radian frequency of the pulsed dipole (p. 14)
- $k_0$  the wavenumber of the pulsed dipole (p. 14)
- $\eta_0$  the intrinsic impedance of free space (p. 14)
- $\Delta\rho$  width of a scattering patch for a pulsed radar (p. 14)
- $\tau_0$  the radar pulse duration (p. 14)
- $c$  the free space speed of light (p. 14)
- $Sa$  the sampling function (p. 14)
- $t$  time (p. 14)
- $R(\tau)$  autocorrelation of the time-domain electric field (p. 14)
- $\lambda_0$  the free space wavelength of the transmitted signal (p. 14)

- $G_r$  the gain of the receiving array (p. 14)
- $\tau$  the time interval between samples (p. 14)
- $*$  operation of complex conjugation (p. 14)
- $\langle \rangle$  operation of ensemble average (p. 14)
- $a$  the amplitude of the platform motion (p. 15)
- $\omega_p$  the frequency of the platform motion (p. 15)
- $\theta_{K_p}$  the direction of the platform motion (p. 15)
- $\sigma_{1mf}$  the first-order monostatic radar cross section for a pulsed source with an antenna on a floating platform (p. 15)
- $\omega_d$  the radian Doppler frequency (p. 15)
- $S_1(m\vec{K})$  the first-order ocean surface spectral power density with  $m$  being -1 for approaching ocean waves and 1 for receding waves (p. 15)
- $J_n$  a Bessel  $J$  function of order  $n$  (p. 15)
- $\delta$  the Dirac delta function (p. 15)
- $S_2(\vec{K}, \omega)$  the second-order ocean wave spectrum (p. 16)
- $H\Gamma$  the hydrodynamic coupling coefficient accounting for the coupling of two first-order ocean waves, whose wave vectors, radian frequencies and Fourier coefficients are  $\vec{K}_1, \vec{K}_2, \omega_1, \omega_2, P_{\vec{K}_1, \omega_1}$  and  $P_{\vec{K}_2, \omega_2}$ , respectively (p. 16)
- $E\Gamma_P$  the monostatic electromagnetic coupling coefficient (p. 17)
- $\Delta$  the intrinsic impedance of the surface (p. 17)
- $\sigma_{2mf}$  the second-order monostatic radar cross section for a pulsed source with an antenna on a floating platform (p. 18)

- $\Gamma_{P_m}$  the monostatic coupling coefficient (p. 18)
- $\phi$  the bistatic angle (p. 23)
- $\overset{t}{*}$  operation of convolution in the time domain (p. 23)
- $\mathcal{F}^{-1}$  inverse Fourier transform (p. 23)
- $h(\cdot)$  the Heaviside function (p. 23)
- $\phi_0$  the representative value of the bistatic angle  $\phi$  (p. 25)
- $\sigma_{1bf}$  the first-order bistatic radar cross section for a pulsed source with an antenna on a floating platform (p. 29)
- ${}_{SE}\Gamma_P$  the bistatic electromagnetic coupling coefficient (p. 35)
- $\Gamma_{P_b}$  the bistatic coupling coefficient (p. 35)
- $\sigma_{2bf}$  the second-order bistatic radar cross section for a pulsed source with an antenna on a floating platform (p. 37)
- $T_r$  the sweep interval for an FMCW waveform (p. 55)
- $\alpha$  the sweep rate for an FMCW waveform (p. 55)
- $B$  the sweep bandwidth for an FMCW waveform (p. 55)
- $\sigma_{1bff}$  the first-order bistatic radar cross section for an FMCW source with an antenna on a floating platform (p. 59)
- $\sigma_{2bff}$  the second-order bistatic radar cross section for an FMCW source with an antenna on a floating platform (p. 61)
- $\hat{\rho}_{p_x}$  the surge direction (p. 70)
- $\hat{\rho}_{p_y}$  the sway direction (p. 70)

- $a_{xi}$  the amplitude of the surge motion (p. 70)
- $a_{yl}$  the amplitude of the sway motion (p. 70)
- $\omega_{xi}$  the radian frequency of the surge motion (p. 70)
- $\omega_{yl}$  the radian frequency of the sway motion (p. 70)
- $\phi_{xi}$  the initial phase of the surge motion (p. 70)
- $\phi_{yl}$  the initial phase of the sway motion (p. 70)
- $\theta_{p_x}$  the direction of the surge motion (p. 71)
- $\sigma_{1mfd}$  the first-order monostatic radar cross section for a pulsed source incorporating a dual-frequency platform motion model (p. 75)
- $\sigma_{2mfd}$  the second-order monostatic radar cross section for a pulsed source incorporating a dual-frequency platform motion model (p. 75)
- $\sigma_{1bfd}$  the first-order bistatic radar cross section for a pulsed source incorporating a dual-frequency platform motion model (p. 77)
- $\sigma_{2bfd}$  the second-order bistatic radar cross section for a pulsed source incorporating a dual-frequency platform motion model (p. 78)
- $\theta_{p_y}$  the direction of the sway motion (p. 80)
- $h(t)$  the transfer function in the time domain (p. 98)
- $H(\omega_d)$  the Fourier transform of  $h(t)$  (p. 98)
- $\otimes$  the linear convolution operation (p. 98)
- $\mathcal{F}$  Fourier transform (p. 99)
- $\mathbf{H}_{matrix}$  the transformation matrix defined by the transfer function (p. 100)

$\mathbf{H}_{matrix}^{-1}$  the inverse of the transformation matrix  $H_{matrix}$  (p. 100)

$F_s(\omega)$  the power spectral density (p. 103)

$\varepsilon(\omega)$  random phase variable between 0 and  $2\pi$  (p. 103)

$s(t)$  a combined sea clutter and external noise signal (p. 103)

$c(t)$  the ocean clutter signal (p. 103)

$n(t)$  the external noise signal (p. 103)

### **List of Abbreviations**

HFSWR High Frequency Surface Wave Radar (p. 1)

HF High Frequency (p. 1)

SNR Signal to Noise Ratio (p. 5)

STAP Space Time Adaptive Processing (p. 7)

DOF Degrees of Freedom (p. 8)

RCS Radar Cross Section (p. 11)

FMCW Frequency Modulated Continuous Waveform (p. 18)

# Chapter 1

## Introduction

### 1.1 Research Rationale

Over the last four decades, techniques for remote sensing of the ocean surface using high frequency surface wave radar (HFSWR) [1] have matured considerably. HFSWR transmits a vertically polarized electromagnetic wave (from 3 to 30 MHz in frequency) that follows the curvature of the earth along the air-water interface. Due to low propagation loss of the high frequency (HF) signal along the ocean surface, these radar systems have the potential for ocean surface sensing over thousands of square kilometers [2], with typical radial resolutions of between a few hundred meters and a few kilometers [3]. Unlike conventional oceanic instruments, such as wave buoys, wave staffs and current meters, HFSWR can provide wide-area, all-weather and near-real-time surveillance. It is well known that HFSWR received signals contain a variety of oceanographic information, such as wind speed, wind direction, surface current fields, and significant wave height. Thus, an understanding and utilization of the received signals is crucial in estimating these parameters.

Based on the geometry of HFSWR, these systems can be divided into two types: monostatic radar (the transmitter and the receiver are collocated) and bistatic radar (the transmitter and the receiver are separated by a distance that is comparable to the expected

target distance). More recently, ocean remote sensing using bistatic configurations has gained increasing interest. For example, Gill *et al.* [4] developed an HFSWR bistatic radar cross section for scatter from a patch of ocean. An ocean wave spectrum inversion technique for bistatic HFSWR appears in [5]. Later, a method for extracting signatures of ship targets from broadened Bragg peaks of bistatic shipborne surface wave radar was proposed in [6]. Huang *et al.* [7] presented a technique to extract wind direction from bistatic HFSWR data. Although bistatic radar systems are typically more complex to implement than their monostatic counterparts, they have a number of advantages that make them well-suited for specific applications. Firstly, bistatic radar systems are flexible with respect to the deployment of the transmitter and the receiver, and the receiver is potentially simple and mobile. Secondly, the receiver requires little protection from the transmitter pulse, and the dynamic range requirement for a bistatic radar is less because there are no large-amplitude, close-range echoes. Thirdly, they are relatively immune to physical and electronic attack due to their inherent passivity and distributed property [8]. In recent years, combinations of monostatic radar with bistatic radar or multistatic radar (containing multiple spatially diverse monostatic radar or bistatic radar components) have been widely used to enlarge the radar coverage region [8].

Depending on the platform location(s) of an HFSWR, these systems can be classified as onshore (land-based) or offshore. Compared to offshore HFSWR, land-based HFSWR has an unavoidable disadvantage in that it has a more limited detection area. The method of mounting an antenna on a floating platform can be employed to enlarge the region of coverage for both oceanic observations and target detection. In order to obtain ocean information further from shore, platform-mounted remote sensing systems have been widely studied and used. For example, Lipa *et al.* [9] mounted an HFSWR on a semisubmersible oil exploration platform and showed the effect of the platform motion on the radar Doppler spectra. Later, Gurgel [10] analyzed and illustrated difficulties in operating a shipborne HFSWR. The effect of ship movement on target detection was also analyzed by using a shipborne HFSWR in [11]. Relevant experimentation

with a floating antenna appears in [12]. All of these studies indicate that if an HFSWR system is installed on a ship or a large floating platform with a mooring system, such as an oil exploration platform, motion effects cannot be ignored in interpreting the radar cross sections and extracting wave information. The platform motion will contaminate the Doppler spectrum, resulting in the obscuration of target and ocean information. Therefore, to properly understand the mechanism of the platform motion on the Doppler spectrum, it is necessary to develop radar cross section models for an antenna on a floating platform. In addition, in order to determine the feasibility of using an HFSWR on a floating platform, it is worth investigating a platform motion compensation method, i.e., a method of mitigating motion-induced sea clutter from the Doppler spectra.

## **1.2 Literature Review**

This section contains a discussion of previous work related to HFSWR when the antenna is mounted on a floating platform. The literature review is divided into three parts: (1) radar cross section models of the ocean surface when the antenna is on a floating platform; (2) analysis of the effect of the platform motion and the corresponding platform motion compensation method; (3) Walsh's scattering theory and more detail on his radar cross section models.

### **1.2.1 Radar Cross Section Models for an Antenna on a Floating Platform**

In order to accurately extract the oceanographic information from the Doppler spectra collected by a radar on a floating platform, it is necessary to develop the corresponding radar cross section models. A number of such models has been established under a variety of conditions.

Spillane *et al.* [13] first mounted an HFSWR system on a semisubmersible oil exploration platform. By using such a radar system, Lipa *et al.* [9] compared the extracted significant waveheight results with and without platform motion compensation. In both studies, the floating oil rig was restrained by a mooring system and assumed to move in response to long-period ocean waves. An accelerometer system was used to obtain real-time series data of the platform motion. In order to mitigate the effect of the platform motion on the Doppler spectrum, a relationship between the Fourier angular coefficients (used to express the radar cross section) in the presence of platform motion and the desired uncontaminated coefficients was derived in [9] based on the established HFSWR ocean surface scatter cross section models in [14] and [15]. Through this relation, significant waveheight results were then calculated and compared with and without the platform motion compensation. It was shown in [9] that platform motion causes sidebands of the first-order radar cross section to be superimposed on the second-order radar cross section. Therefore, unless compensated, the significant waveheight results, extracted by inverting the second-order radar cross section, will be overestimated.

In [16], Walsh presented a fundamental scattering theory for HFSWR with an antenna on a floating platform. Following this research, Walsh *et al.* [17] developed the first-order monostatic radar cross section where both the transmitter and the receiver were on a floating platform, and then extended this analysis to the second-order patch scatter cross section [18] and second-order foot scatter cross section [19]. Patch scatter indicates a double scatter at a surface patch, while foot scatter means one scatter occurs near the transmitter and another on a remote surface patch, or one scatter occurs on a remote patch of the ocean surface and another near the receiver. These models were established for an extremely narrow antenna beam and were found to consist of Bessel functions that occurred due to the assumed sinusoidal antenna motion model. In all studies, it was assumed that the platform motion was caused by the dominant ocean wave so that the amplitude and frequency of the sinusoidal motion were determined by the wind speed (sea state). Also, the direction of the platform motion was taken to be the same as the

wind direction. Simulation results, based on these derived models, were presented in [17–19] and showed that the antenna motion causes additional, symmetrically distributed peaks to appear in the Doppler spectrum. These motion-induced peaks contain less energy in the second-order radar cross section than those in the first-order radar cross section.

Following the research mentioned above, a general form of the first-order floating HFSWR model, without specifying a particular platform motion, was derived in [20] and [21]. This model was tested under a variety of platform motions and compared with the published results appearing in [11] and [17]. In addition, simulations were made with real platform motion data and compared with field data. Comparisons showed the simulation results were consistent with the experimental results.

Xie *et al.* [22] developed a first-order ocean surface RCS model for an HFSWR located on a ship having a constant forward speed. Experimental and simulation results showed that the first-order Bragg lines are spread in the spectrum because of the ship motion and the broad antenna beam. Later, a corresponding second-order shipborne HFSWR cross section with uniform linear ship motion was derived in [23]. Based on the derived shipborne RCSs and the spreading mechanism of the Bragg lines, a method for extracting ocean surface wind direction from shipborne HFSWR data was proposed and demonstrated in [24]. By using a single receiving sensor rather than a receiving array, wind directions of a large sea area covered by the broad beam antenna were obtained with an error of around  $2^\circ$  when signal to noise ratio (SNR) was above 15 dB. The ambiguity problem was resolved using the method proposed in [25]. Compared with the conventional method based on a land-based receiving array, this method was stated to be more easily realized with less system cost. Similarly, methods for ocean surface current extraction and ocean clutter spectrum estimation for shipborne HFSWR were developed in [26–28].

In order to make the RCS simulations reflect reality more closely, the characteristics of ship oscillation (including roll, pitch and yaw) were analyzed, and a model of the ship

oscillation was developed [29]. It was assumed that the ship oscillation in each dimension was independent and approximated a simple harmonic motion, whose frequency and amplitude are determined by the type of ship and the sea state. Then, a synthetic velocity model considering both ship velocity and ship oscillation was established. Based on this model, simulations were made to compare sea clutter spectra with and without ship oscillation. Comparisons showed that the oscillating movement of a ship has a significant influence on the sea clutter spectrum broadening, but that this effect can be ignored in the case of low sea states, for example, sea state 3 and less, when the HFSWR operating frequency was 15 MHz.

### **1.2.2 Analysis of the Effect of the Platform Motion and Platform Motion Compensation Methods**

From 1985 to 1992, a team at the University of Hamburg modified a Coastal Ocean Dynamic Applications Radar (CODAR) system [30] for shipborne operation. A combination of a land-based and a shipborne CODAR was used during the NORCSEX' 88 experiment to measure the surface current fields along the Norwegian coast [31]. Based on the data from these experiments, considerable research was published, for example, in [31–33].

Gurgel analyzed and highlighted difficulties in operating a shipborne HFSWR in [10] and [32]. Firstly, it is very difficult to handle the ship to keep the speed and direction constant and to measure the ship's movement accurately. Secondly, there may be a severe interaction between the ship's body and the receiving array. Thus, the arrangement of the receiving array is critical for minimizing the distortion of the antenna pattern. In addition, Gurgel suggested that it is crucial to develop a method to compensate for this distortion. Finally, it was found that the ship's pitch and roll movements cause amplitude and phase modulation of the sea echoes. Amplitude modulation is due to the deformation of the vertical polarization and the resulting change of the signal's

coupling to the sea. In addition, phase modulation is caused by the changing distance from the antenna to the scattering ocean patch, which turns out to be the major effect (the target signal was obscured by the extra peaks in the Doppler spectra). Therefore, a method to filter out the amplitude and phase modulation of the sea echoes due to the pitch and roll movements was found to be important. Some suggestions for operating a shipborne HFSWR in order to reduce the influence of the ship movement and improve the radar's working performance were also given in [10] and [32]. For example, it was suggested that an HFSWR system should be installed above the sea, as low as possible, to reduce the phase modulation caused by the pitch and roll movements. Following this research, Gurgel and Essen [33] discussed and evaluated the performance of a shipborne current mapping HFSWR. It was found that, with the ship navigation data provided by the satellite-supported Global Positioning System (GPS), the shipborne HFSWR could measure surface current velocities with an accuracy of 5 cm/s.

Howell and Walsh [34] described an inversion algorithm for nondirectional wave spectra using an omnidirectional antenna and presented measurements of ocean wave spectra from a ship-mounted HFSWR. Firstly, the omni-directional first- and second-order RCS models were developed based on the narrow-beam RCS models. Then, the effect of the ship motion, surface currents, and antenna pattern distortion due to the interaction of the antenna with nearby metal objects were discussed in [34]. For a sea state with 3.5 m significant wave height, the root mean square pitch and roll angles of the ship were recorded in [34] to be about  $1.5^\circ$ , which corresponded to a relatively small lateral displacement of around 7.5% of the Bragg wavelength for a monopole antenna operating at 25.4 MHz and situated 17 m above the sea surface. In this case, the ship motion was assumed to have little impact on the experimental data and could be ignored. Finally, the inversion algorithm was tested using the experimental data and showed a positive preliminary performance.

The effect of the movement of the radar platform on target detection was analyzed by using a shipborne HFSWR [35]. Following this research, field data collected by a

shipborne HFSWR system over the Yellow Sea of China was presented in [11]. The spreading regions of the first-order Bragg lines were illustrated, and this effect was seen to be closely related to the ship's velocity. Additionally, when the ship velocity is low, the spreading spectrum will appear as a bandpass spectrum; otherwise, it will be lowpass. Space-time adaptive processing (STAP) for a shipborne radar was introduced to suppress the spreading clutter and to improve the performance of target signal detection. The experimental data showed good agreement with the theoretical analysis. By using this experimental data, STAP was shown to work efficiently for sea clutter suppression.

Ji *et al.* [36] extended the research presented in [11] by developing a model with both the six degrees of freedom (DOF) motion of the ship and uniform forward motion. By analyzing the data derived from the model, it was concluded that the roll, pitch and yaw motions of the ship are dominant and account for the main impact on the HFSWR data. It was shown that the STAP technique successfully compensated for ship movement.

The STAP technique to compensate for the ship movement for shipborne HFSWR was demonstrated in [37]. The STAP technique is based on the radar wavelength, pulse repetition period and the velocity of the platform. A weight matrix or optimal filter was built, and then was multiplied with the radar received data. By using to advantage the notches or nulls of the filter response, the shifted Bragg peaks (i.e., only two shifted Bragg peaks in the spectra instead of a broad region of Bragg peaks) were removed from the Doppler spectra, so that the target signal would be more readily detected. In addition, STAP can be used to suppress the Bragg peaks (commonly called sea clutter), while not used to suppress the second-order peaks. This is because the magnitudes of the second-order peaks are relatively low and usually have little effect on the target signal.

Although STAP has been widely used to suppress sea clutter and improve the performance of target detection, it has some obvious disadvantages, one being that it requires a large amount of computation. Additionally, STAP is highly dependent on the ship motion model. The established ship motion model is usually developed from an empirical model with ideal assumptions, resulting in a reduced accuracy of the estimated spectrum.

Other compensation methods have also been proposed and used to mitigate the effect of the platform motion. For example, Wang *et al.* [38] derived a time-varying model for the steering vector of a phased array pulsed Doppler radar system with the antenna array on a floating platform. Six DOF oscillating motions of the platform were considered in the model as well as the forward motion of the platform. Through this model, a maximum likelihood motion compensation technique was applied to the received sensor array data, and then the expression for the beamformed outputs was obtained. These studies concluded that the motion compensation was robust to the yaw measurement error and the error of the six DOF motion in the beamformed output could be considered to be negligible when 10% measurement error was tolerable. The simulation results indicated that six oscillating motions caused no significant changes in the targets' responses under calm sea states (up to 3, gentle breeze), while the forward motion could cause spreading in the spectra.

Bourges *et al.* [39] put each element of the antenna array on a buoy, resulting in each element having a different movement. Only vertical displacement of the buoy motion was considered and the radiation pattern was studied in the azimuth plane. A sinusoidal function was used to model the swell motion (the buoys' dominant movement). The buoys' movements caused the changing of the nulls of the radiation pattern. Schelkunoff's zero placement method was introduced and applied to correct the disturbances caused in the radiation pattern by the buoys' movements. Then, two methods for correcting vertical deformations of the receiving array radiation pattern with the receiving array mounted on buoys were presented in [40]. Following this research, further analysis of the effect of the buoys' movements were conducted in [41] and [42]. The model of the buoys' movements was re-established and calculated from a realistic modeling of a sea surface. Both vertical and horizontal deformations of the receiving array were considered and analyzed. In a vertical displacement, the main disturbances come from the modification of the coupling in the array. For the horizontal displacement, the modification of the

inter-element spacing in the array resulted in the main disturbance. A real-time motion compensation method was provided to optimize the radiation pattern of the antenna array.

The majority of motion compensation methods have been proposed to correct for only the motion effect on the radiation pattern of the antenna array (see, for example, [39], [41] and [42]). However, the platform motion also has a significant effect on the Doppler spectra, for example, causing both spread Bragg peaks and the generation of motion-induced peaks. STAP is widely used to compensate for the effect of the motion on the Doppler spectra. The aim of STAP is to suppress the sea clutter information (mainly referring to the spread Bragg peaks) in the Doppler spectra and to improve ship detection performance. It achieves this by eliminating the clutter rather than by correcting. However, this approach is not appropriate for ocean remote sensing applications where it is required to compensate in order to retain the integrity of the first- and second-order ocean spectra. The motion compensation method proposed in this thesis aims to recover the motion-compensated Doppler spectra (i.e., to remove the motion-induced peaks in the Doppler spectra, and to recover the energy and the bandwidth of the first- and second-order peaks) for the purpose of extracting ocean information from the Doppler spectra. Additionally, while STAP is especially applied to compensate for linear motion effects, the motion compensation method in this study are applied to platform motions represented as a sum of sinusoidal functions.

### **1.2.3 Walsh's Scattering Theory and Monostatic Radar Cross Section Models**

In order to provide insight into the effect of platform motion on Doppler spectra, a radar cross section model incorporating platform motion is derived. The HFSWR cross section models of the ocean surface in this thesis are developed based on the Walsh's scattering theory and radar cross section models. Thus, it is necessary to review the HFSWR cross section models developed based on Walsh's scattering method.

In 1987, Walsh and Donnelly [43] derived the general expressions for the electromagnetic field for a surface with an arbitrary profile, including plane earth propagation, layered media propagation, mixed-path propagation and rough surface scattering. By considering the operation of a pulsed HF vertical dipole source and invoking the good conducting surface, small height and small slope assumptions [44], the first two orders of the backscatter radar cross sections were obtained. By adding a small displacement in the source term of the electric field equation to represent the antenna motion, the first- and second-order monostatic HFSWR cross sections of the ocean surface for a pulsed source with an antenna on a floating platform have since been developed [17–19]. In these later works, a sinusoidal function with a single frequency was used to describe the platform motion, or barge motion in the horizontal plane.

The general process of the monostatic radar cross section (RCS) model derivation used in [17–19] is summarized in Fig. 1.1. Firstly, the electric field equation is written as an asymptotic integral. Then, the time-invariant surface expression is specified and substituted into the electric field equation. In order to solve the complex integral, a stationary phase method is adopted [45]. The stationary phase method is mainly accomplished by a polar or elliptic coordinate transformation, depending on whether the scattering geometry is monostatic or bistatic, respectively. Next, the electric field equation is inversed Fourier transformed into the time domain, and a pulsed dipole is designated to be the exciting source. From pulse to pulse, the ocean surface is time varying, and consequently the rough surface function must be modified to account for this effect. Finally, taking the Fourier transform of the autocorrelations of the electric fields to calculate the power spectral density, the expression for the radar cross section can be obtained by comparing the power density with the standard radar range equation.

The second-order radar foot-scatter cross section model is not addressed in this thesis due to its lesser contribution to the total radar cross section [19]. Additionally, the peaks introduced by the second-order radar foot-scatter cross section are at 0 Hz and twice the Bragg peak frequencies in the Doppler spectra [46]. These peaks appear out

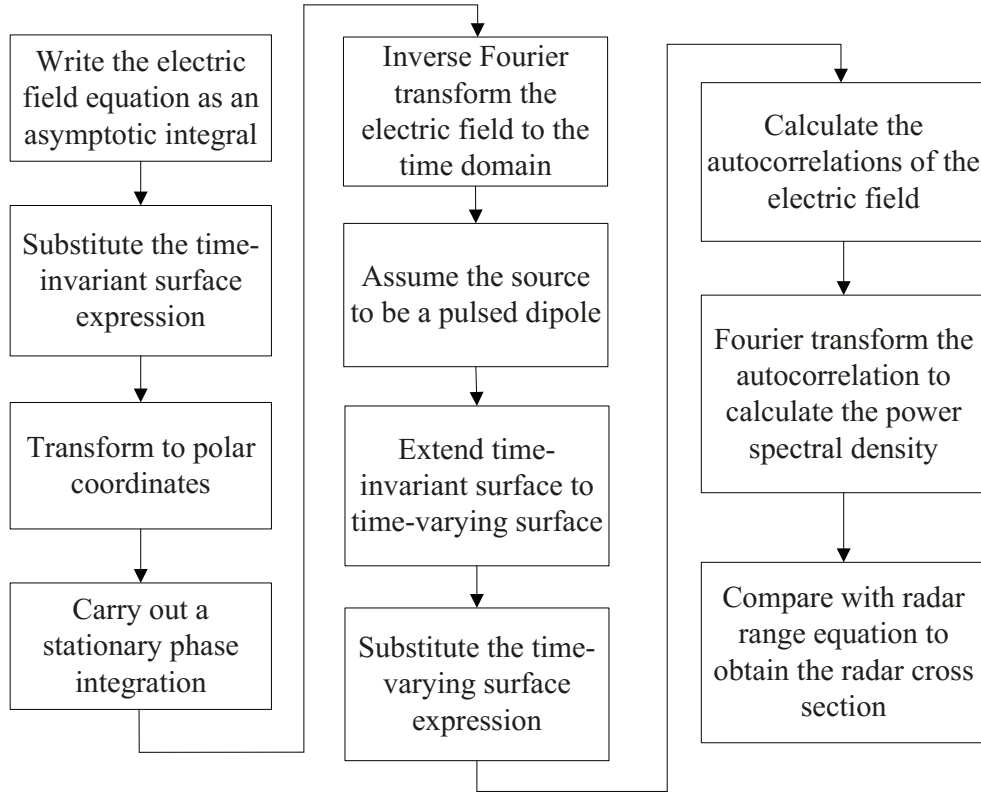


Fig. 1.1 The RCS derivation process block diagram.

of the Doppler region of interest for the purpose of ocean remote sensing. Thus, only the first-order [17] and second-order radar patch scatter [18] cross section models are reviewed below.

### 1.2.3.1 The First-Order Radar Cross Section Model

Under the assumption of a good conducting surface and imposing the usual small height and small slope constraints for the ocean waves, the HFSWR scattered field  $E_n$  for a floating transmitter can be written as [17], [18]

$$E_n - \left\{ \left( \nabla \xi \cdot \nabla E_n \right)^{xy} * \left( F(\rho) \frac{e^{-jk\rho}}{2\pi\rho} \right) \right\} = C_0 F(\rho) \frac{e^{-jk\rho'}}{2\pi\rho} \quad (1.1)$$

where  $\rho$  is the planar distance from the transmitter to the receiver  $(x, y)$  on the rough surface  $\xi$ , shown in Fig. 1.2, while  $\rho'$  is the distance from the transmitter to the receiver,

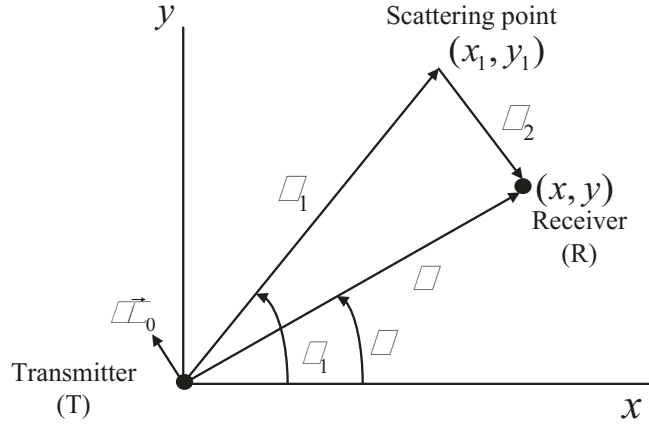


Fig. 1.2 General first-order bistatic scatter geometry including antenna motion.

incorporating the transmitter displacement vector  $\delta\vec{\rho}_0$ , and is given by

$$\rho' \approx \rho - \hat{\rho} \cdot \delta\vec{\rho}_0$$

where the hat indicates a unit vector. The dipole constant,  $C_0$ , is expressed as

$$C_0 = \frac{I\Delta l k^2}{j\omega\epsilon_0}$$

where the source is assumed to be a vertical dipole of length  $\Delta l$  carrying a current  $I$  whose radian frequency and wavenumber are  $\omega$  and  $k$ , respectively, in a space with permittivity  $\epsilon_0$ .  $\ast$  indicates two-dimensional spatial convolution and  $F(\rho)$  represents the Sommerfeld attenuation function [47].  $\nabla = \hat{x}\frac{\partial}{\partial x} + \hat{y}\frac{\partial}{\partial y} + \hat{z}\frac{\partial}{\partial z}$  with the hatted vectors being the unit vectors along the coordinate axes and  $j = \sqrt{-1}$ . A Neumann series solution of (1.1) gives the first-order received electric field for a fixed receiver and a floating transmitter as [17]

$$(E_n)_1 \approx \frac{kC_0}{(2\pi)^2} \sum_{\vec{K}} P_{\vec{K}} K \int_{x_1} \int_{y_1} \cos(\theta_1 - \theta_K) \frac{F(\rho_1)F(\rho_2)}{\rho_1\rho_2} \cdot e^{jk\delta\rho_0 \cos(\theta_1 - \theta_0)} e^{j\rho_1 K \cos(\theta_1 - \theta_K)} e^{-jk(\rho_1 + \rho_2)} dy_1 dx_1 \quad (1.2)$$

where  $\rho_1$ ,  $\rho_2$  and  $\theta_1$  are depicted in Fig. 1.2.  $\delta\rho_0$  and  $\theta_0$ , respectively, represent the magnitude and the direction of  $\delta\vec{\rho}_0$ , and  $\sum$  is the usual summation symbol. The time-

invariant rough surface  $\xi$ , which is represented by a Fourier series, may be expressed as

$$\xi(x, y) = \sum_{\vec{K}} P_{\vec{K}} e^{j\vec{\rho} \cdot \vec{K}}, \quad (1.3)$$

with  $P_{\vec{K}}$  being the Fourier coefficient for a surface component whose wave vector is  $\vec{K}$ ,  $K$  and  $\theta_K$  being, respectively, the magnitude and the direction of  $\vec{K}$ .

For a monostatic geometry, it may be shown, as in [17], that  $\rho_2 \approx \rho_1 - \delta \vec{\rho}_0 \cdot \hat{\rho}_1$ . By using this approximation and taking an inverse Fourier transform of  $(E_n)_1$ , after including a pulsed sinusoid dipole excitation, it may be shown that the time-domain version of (1.2) is

$$(E_n)_{1mf}(\rho_0) \approx -j\eta_0 \Delta l \Delta \rho I_0 k_0^2 \frac{F^2(\rho_0, \omega_0)}{(2\pi\rho_0)^{3/2}} e^{-j\frac{\pi}{4}} e^{jk_0 \Delta \rho} \cdot \sum_{\vec{K}} P_{\vec{K}} \sqrt{K} e^{jK\rho_0} e^{jK\delta\rho_0 \cos(\theta_K - \theta_0)} \text{Sa}\left[\frac{\Delta\rho}{2}(K - 2k_0)\right] \quad (1.4)$$

where  $I_0$ ,  $\omega_0$  and  $k_0$  are the peak current, the radian frequency and the wavenumber, respectively, of the pulsed dipole excitation.  $\eta_0$  represents the intrinsic impedance of free space.  $\rho_0 = \frac{c(t - \frac{\tau_0}{2})}{2}$  and the patch width  $\Delta\rho = \frac{c\tau_0}{2}$  depend on the radar pulse duration  $\tau_0$ .  $c$  is the free space speed of light and  $\text{Sa}(x) = \frac{\sin x}{x}$  represents the sampling function.

Next, to introduce surface time variation into the analysis, the rough ocean surface is represented as a zero-mean, stationary Gaussian process of arbitrary variance. The time-varying surface  $\xi$  is expressed as

$$\xi(x, y, t) = \sum_{\vec{K}, \omega} P_{\vec{K}, \omega} e^{j\vec{K} \cdot \vec{\rho}} e^{j\omega t}. \quad (1.5)$$

After introducing the time-varying ocean surface variation (1.5) into the received electric field (1.4), an autocorrelation of the time-domain electric field,  $R(\tau)$ , can be carried out as

$$R(\tau) = \frac{A_r}{2\eta_0} \langle (E_n)_1(t + \tau) (E_n)_1^*(t) \rangle \quad (1.6)$$

where  $A_r = (\lambda_0^2/4\pi)G_r$ , with  $\lambda_0$  being the free space wavelength of the transmitted signal and  $G_r$  being the gain of the receiving array.  $\tau$  represents the interval between samples.  $*$  and  $\langle \rangle$  represent the operations of complex conjugation and ensemble averaging, respectively.

In [17] and [18], it is assumed that the platform sway is caused by the dominant ocean wave so that

$$\delta\vec{\rho}_0 = a \sin(\omega_p t) \hat{\rho}_p \quad (1.7)$$

where  $a$  and  $\omega_p$  represent the motion amplitude and frequency, respectively.  $\hat{\rho}_p$ , set as the angle  $\theta_{K_p}$ , represents the direction of  $\delta\vec{\rho}_0$ .

After Fourier transforming the autocorrelation and comparing the power spectral density directly with the standard radar range equation, the first-order monostatic radar cross section,  $\sigma_{1mf}(\omega_d)$ , for an antenna on a floating platform may be written as [17]

$$\begin{aligned} \sigma_{1mf}(\omega_d) = & 2^3 \pi k_0^2 \Delta\rho \sum_{m=\pm 1} \int_K K^2 S_1(m\vec{K}) \text{Sa}^2 \left[ \frac{\Delta\rho}{2} (K - 2k_0) \right] \\ & \cdot \{ J_0^2 [aK \cos(\theta_K - \theta_{K_p})] \delta(\omega_d + m\sqrt{gK}) + \sum_{n=1}^{\infty} J_n^2 [aK \cos(\theta_K - \theta_{K_p})] \\ & \cdot [\delta(\omega_d + m\sqrt{gK} - n\omega_p) + \delta(\omega_d + m\sqrt{gK} + n\omega_p)] \} dK \end{aligned} \quad (1.8)$$

where  $\omega_d$  represents the radian Doppler frequency. The first-order ocean surface spectral power density is expressed by  $S_1(m\vec{K})$  with  $m$  being -1 for approaching ocean waves and 1 for receding waves.  $J_n$  represents a Bessel function of the first kind of order  $n$ , and  $\delta$  is the Dirac delta function.

### 1.2.3.2 The Second-Order Radar Cross Section Model

The second-order radar cross section contains both hydrodynamic and electromagnetic contributions. The second-order hydrodynamic contribution is caused by the signal from the transmitter being scattered once by second-order ocean waves before being received. The second-order electromagnetic contribution arises from double scattering

from first-order ocean waves. Equation (1.8) is the first-order radar cross section model and contains the first-order ocean wave spectrum  $S_1(\vec{K}, \omega)$ . The second-order ocean wave spectrum can be expressed as

$$S_2(\vec{K}, \omega) = 2 \int \int_{\substack{\vec{K}_1 + \vec{K}_2 = \vec{K} \\ \omega_1 + \omega_2 = \omega}} S_1(\vec{K}_1, \omega_1) S_1(\vec{K}_2, \omega_2) |_H \Gamma|^2 d\vec{K}_1 d\omega_1 \quad (1.9)$$

where  $_H \Gamma$  is the hydrodynamic coupling coefficient [48] accounting for the coupling of two first-order ocean waves, whose wave vectors and radian frequencies are  $\vec{K}_1$ ,  $\vec{K}_2$ ,  $\omega_1$  and  $\omega_2$ , respectively. By replacing  $S_1(\vec{K}, \omega)$  with  $S_2(\vec{K}, \omega)$ , (1.8) becomes the expression for the second-order hydrodynamic portion of the radar cross section of the ocean for the case of an antenna on a floating platform and may be written as

$$\begin{aligned} \sigma_{2mf}(\omega_d) = & 2^6 \pi^2 k_0^4 \sum_{m_1=\pm 1} \sum_{m_2=\pm 1} \int_0^\infty \int_{-\pi}^\pi |_H \Gamma|^2 S_1(m_1 \vec{K}_1) S_1(m_2 \vec{K}_2) K_1 \\ & \cdot \sum_{n=-\infty}^\infty J_n^2[aK \cos(\theta_K - \theta_{K_p})] \\ & \cdot \delta(\omega_d + m_1 \sqrt{gK_1} + m_2 \sqrt{gK_2} + n\omega_p) d\theta_{\vec{K}_1} dK_1. \end{aligned} \quad (1.10)$$

Following a similar procedure to that for the first-order case, the second-order received electric field,  $(E_n)_2$ , for a fixed receiver and a floating transmitter can also be simplified using a Neumann series to give [18]

$$\begin{aligned} (E_n)_2 \approx & \frac{k^2 C_0}{(2\pi)^3} \sum_{\vec{K}_1} \sum_{\vec{K}_2} P_{\vec{K}_1} P_{\vec{K}_2} \int_{A_2} \int_{A_1} (\vec{K}_1 \cdot \hat{\rho}_1) (\vec{K}_2 \cdot \hat{\rho}_{12}) e^{j\vec{K}_1 \cdot \vec{\rho}_1} e^{j\vec{K}_2 \cdot \vec{\rho}_2} \\ & \cdot e^{jk\hat{\rho}_1 \cdot \delta\vec{\rho}_0} F(\rho_1) F(\rho_{12}) F(\rho_{20}) \frac{e^{-jk(\rho_1 + \rho_{12} + \rho_{20})}}{\rho_1 \rho_{12} \rho_{20}} dA_1 dA_2 \end{aligned} \quad (1.11)$$

where  $P_{\vec{K}_1}$  and  $P_{\vec{K}_2}$  represent the Fourier coefficients of the first-order waves, which are associated with  $S_1(m_1 \vec{K}_1)$  and  $S_1(m_2 \vec{K}_2)$ , respectively. The geometric parameters  $\rho_1$ ,  $\rho_{12}$  and  $\rho_{20}$  are depicted in Fig. 1.3. In Cartesian coordinates,  $dA_1 = dx_1 dy_1$  and  $dA_2 = dx_2 dy_2$ . By applying the monostatic geometry, for which  $\rho_{20} \approx \rho_2 - \delta\vec{\rho}_0 \cdot \hat{\rho}_2$ , and the patch scatter assumption,  $\rho_{12} \ll \rho_1, \rho_2$ , the double integral in (1.11) can be

simplified. Following a similar analysis as was used to derive the first-order electric field for a pulsed dipole, the time domain result for the second-order electric field is

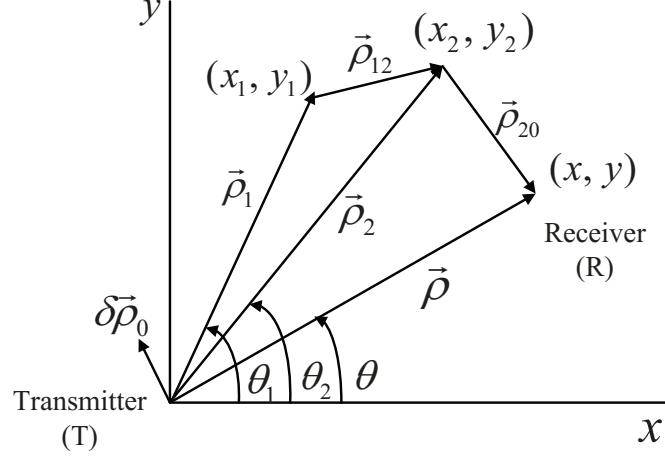


Fig. 1.3 General second-order bistatic scatter geometry with antenna motion.

$$(E_n)_{2mf}(\rho_0) \approx -j\eta_0\Delta l\Delta\rho I_0 k_0^2 \frac{F^2(\rho_0, \omega_0)}{(2\pi\rho_0)^{3/2}} e^{jk_0\Delta\rho} e^{-j\frac{\pi}{4}} \cdot \sum_{\vec{K}_1} \sum_{\vec{K}_2} E\Gamma_P P_{\vec{K}_1} P_{\vec{K}_2} \sqrt{K} e^{jK\rho_0} e^{jK\delta\rho_0 \cos(\theta_K - \theta_0)} \text{Sa}\left[\frac{\Delta\rho}{2}(K - 2k_0)\right] \quad (1.12)$$

where the electromagnetic coupling coefficient can be expressed as

$$E\Gamma_P(\vec{K}_1, \vec{K}_2) = \frac{jk_0}{2K^2} \frac{|\vec{K}_1 \times \vec{K}_2|^2}{k_0^2 - \vec{K}_1 \cdot \vec{K}_2} \left\{ 1 - j \frac{k_0(1 + \Delta)}{\sqrt{-\vec{K}_1 \cdot \vec{K}_2 + jk_0\Delta}} \right\} \quad (1.13)$$

with  $\Delta$  being the intrinsic impedance of the surface. From (1.12), a similar process to the first-order case is conducted to calculate the second-order electromagnetic portion of the radar cross section. Adding this electromagnetic contribution and the hydrodynamic result (1.10), the total second-order monostatic radar cross section of the ocean when the

antenna is on a floating platform may be written as [18]

$$\begin{aligned}
\sigma_{2mf}(\omega_d) = & 2^6 \pi^2 k_0^4 \sum_{m_1=\pm 1} \sum_{m_2=\pm 1} \int_0^\infty \int_{-\pi}^\pi |\Gamma_{P_m}|^2 S_1(m_1 \vec{K}_1) S_1(m_2 \vec{K}_2) K_1 \\
& \cdot \sum_{n=-\infty}^\infty J_n^2[aK \cos(\theta_K - \theta_{K_p})] \\
& \cdot \delta(\omega_d + m_1 \sqrt{gK_1} + m_2 \sqrt{gK_2} + n\omega_p) d\theta_{\vec{K}_1} dK_1
\end{aligned} \tag{1.14}$$

where  $\Gamma_{P_m} = E\Gamma_P + H\Gamma$ .

### 1.3 The Scope of the Thesis

In this thesis, HFSSWR cross section models of the ocean surface for the case of an antenna on a floating platform are investigated further based on the theoretical foundations developed by Walsh [16]. The outline of this thesis is as follows.

In Chapter 2, based on the general form of the received electric field [17, 18], the first- and second-order bistatic radar cross section models for a pulsed source with a fixed receiver and a transmitter on a floating platform are developed. Comparisons of these new bistatic models with earlier radar cross section models are then made. In order to investigate how antenna motion impacts the RCS, the corresponding Doppler spectra are simulated under a variety of sea states.

In Chapter 3, the first- and second-order bistatic radar cross section models with a fixed receiver and a transmitter on a floating platform are extended to a frequency modulated continuous waveform (FMCW) source. Based on established models, simulations are made to compare the Doppler spectra for an FMCW waveform with those for a pulsed waveform.

In Chapter 4, a more realistic platform motion model is proposed. In order to simplify the study, the platform motion model is considered to be a combination of two cosine functions in a single motion direction. Based on this newly-derived platform motion model, the corresponding monostatic and bistatic radar cross sections are developed. Fol-

lowing this research, radar cross sections are extended for a more complicated platform motion model by considering multiple frequencies and directions. The corresponding models are simulated and the impact of the antenna motion on the Doppler spectra is discussed.

In Chapter 5, a compensation method to mitigate the effect of the platform motion on the Doppler spectra is proposed. To simulate radar field data and examine this motion compensation method, radar cross section models with external white Gaussian noise are developed. Based on experimental platform motion data, radar cross sections are simulated under a variety of sea states and SNRs. The corresponding motion compensation results are obtained and evaluated.

In Chapter 6, a summary of the fundamental conclusions obtained from the research in this thesis is given. Additionally, several suggestions for future work are proposed.

The research presented in this thesis has been published or submitted for review in six refereed journal papers as listed below:

1. Y. Ma, E. W. Gill, and W. Huang, "First-order bistatic high-frequency radar ocean surface cross-section for an antenna on a floating platform," *IET Radar Sonar Navig.*, vol. 10, no. 6, pp. 1136-1144, 2016.

This paper provides the development of the first-order radar cross section model for a pulsed source with an antenna on a floating platform (Section 2.2).

2. Y. Ma, W. Huang, and E. W. Gill, "The second-order bistatic high frequency radar ocean surface cross section for an antenna on a floating platform," *Can. J. Remote Sens.*, vol. 42, no. 4, pp. 332-343, 2016.

This paper provides the development of the second-order radar cross section model for a pulsed source with an antenna on a floating platform (Section 2.3).

3. Y. Ma, W. Huang, and E. W. Gill, "Bistatic high frequency radar ocean surface cross section for an FMCW source with an antenna on a floating platform," *Int. J. Antennas Propag.*, vol. 2016, p. ID 8675964, 2016.

This paper provides the development of the radar cross section models for an FMCW source with an antenna on a floating platform (Chapter 3).

4. Y. Ma, W. Huang, and E. W. Gill, "High frequency radar ocean surface cross section incorporating a dual-frequency platform motion model," *IEEE J. Oceanic Eng.*, 2017. (in press)

This paper provides the development of the monostatic radar cross section models with a more realistic platform motion model (Section 4.3 and Section 4.5).

5. Y. Ma, E. W. Gill, and W. Huang, "Bistatic high frequency radar ocean surface cross section incorporating a dual-frequency platform motion model," *IEEE J. Oceanic Eng.*, 2017. (in press)

This paper provides the development of the bistatic radar cross section models with a more realistic platform motion model (Section 4.4).

6. E. W. Gill, Y. Ma, and W. Huang, "Motion compensation for high frequency surface wave radar on a floating platform," *IET Radar Sonar Navig.*, 2017. (in press)

This paper provides the development of the motion compensation method for HFSWR on a floating platform (Chapter 5).

## **Chapter 2**

# **Bistatic Radar Cross Section for a Pulsed Source with an Antenna on a Floating Platform**

### **2.1 Introduction**

The first- and second-order HFSWR bistatic cross sections of the ocean surface for a pulsed source with a fixed receiver and a distant transmitter on a floating platform are developed in this chapter. Previously presented equations (1.2) and (1.11) are the expressions for the bistatically received first- and second-order electric fields. By specifying a pulsed dipole as the source and using a three-dimensional Fourier series, whose coefficients are random variables, to represent a time-varying ocean surface, the electric field equation in the time domain can be deduced. From this, the power spectral density may be readily determined and the corresponding radar cross section can be derived by invoking the standard radar range equation.

In this chapter, the first- and second-order bistatic radar cross sections for a pulsed source with an antenna on a floating platform are presented. Using these newly-derived RCS models, corresponding simulations are conducted to investigate how the antenna

motion affects the bistatic HFSWR Doppler spectra. In Section 2.2, the derivation process of the first-order bistatic radar cross section for the case of a fixed receiver and a transmitter being mounted on a floating platform is outlined. The derivation of the second-order bistatic radar patch scatter cross section is presented in Section 2.3. It should be mentioned that only scattering from a portion of the ocean surface which is remote from both the transmitter and receiver – the patch scatter case – is addressed in this thesis. This means that, for the double scatter case, the two scattering points are very close to each other compared to the distances between them and the antennas. Section 2.4 contains a comparison of the radar cross section models developed in Section 2.2 and 2.3 with earlier models. Section 2.5 presents a number of simulations based on these newly-derived models and discusses their significance. A summary of the chapter appears in Section 2.6.

A simple diagram of bistatic scatter for an antenna on a floating platform is depicted in Fig. 2.1. In our study, the transmitter is an omnidirectional dipole on a floating platform. The receiver is an onshore phased antenna array.

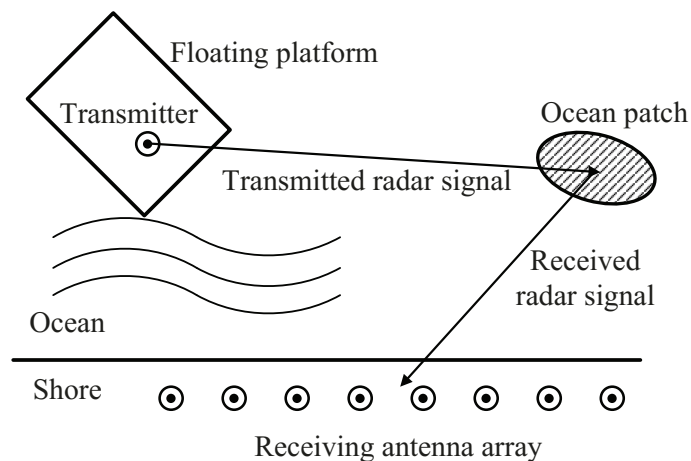


Fig. 2.1 A diagram of bistatic scatter for a fixed receiver and a transmitter on a floating platform.

## 2.2 The First-Order Radar Cross Section Model

### A. First-Order Field Equation

Bistatic HFSWR cross section for a stationary antenna has been previously derived in [49], and the electric field of form similar to (1.2) is solved by a stationary phase process. The detailed stationary phase process is provided in Appendix A. Using this approach, the double integral in (1.2) can be solved, and the bistatic received electric field reduces to [50]

$$(E_n)_{1bf} \approx \frac{\pm kC_0}{(2\pi)^{3/2}} \sum_{\bar{K}} P_{\bar{K}} \sqrt{K} e^{j\frac{\rho K}{2} \cos(\theta_K - \theta)} \int_{\rho/2}^{\infty} \frac{F(\rho_1)F(\rho_2)}{\sqrt{\rho_s[\rho_s^2 - (\rho/2)^2]}} e^{\mp j\frac{\pi}{4}} \cdot \sqrt{\cos \phi} e^{jk\delta\rho_0[\cos \phi \cos(\theta_K - \theta_0) + \sin \phi \sin(\theta_K - \theta_0)]} e^{j\rho_s[\pm K \cos \phi - 2k]} d\rho_s \quad (2.1)$$

where  $\rho_s = \frac{\rho_1 + \rho_2}{2}$  and  $\phi$  is the bistatic angle (see Fig. A.1).

### B. Time Domain Analysis Incorporating a Pulsed Dipole

An inverse Fourier transform ( $\mathcal{F}^{-1}$ ) of (2.1) yields the time domain result for the first-order electric field. It is known that  $\omega$  is the transformed frequency variable and  $kC_0$  is a function of  $\omega$ . Thus, the frequency domain expression corresponding to (2.1) can be written as

$$(E_n)_{1bf}(t) \approx \frac{\pm 1}{(2\pi)^{3/2}} \mathcal{F}^{-1}(kC_0) \overset{t}{*} \mathcal{F}^{-1} \left\{ \sum_{\bar{K}} P_{\bar{K}} \sqrt{K} e^{j\frac{\rho K}{2} \cos(\theta_K - \theta)} e^{\mp j\frac{\pi}{4}} \int_{\rho/2}^{\infty} \frac{F(\rho_1, \omega_0)F(\rho_2, \omega_0)}{\sqrt{\rho_s[\rho_s^2 - (\rho/2)^2]}} \sqrt{\cos \phi} \cdot e^{jk\delta\rho_0[\cos \phi \cos(\theta_K - \theta_0) + \sin \phi \sin(\theta_K - \theta_0)]} e^{j\rho_s[\pm K \cos \phi - 2k]} d\rho_s \right\}. \quad (2.2)$$

For a pulsed dipole source [51], it is shown that

$$\mathcal{F}^{-1}(kC_0) \approx -j\eta_0 \Delta I I_0 k_0^2 e^{j\omega_0 t} [h(t) - h(t - \tau_0)] \quad (2.3)$$

where  $h$  represents the Heaviside function. Moreover,

$$\begin{aligned} & \mathcal{F}^{-1} \left\{ e^{j\frac{\omega}{c}} \{ \delta\rho_0 [\cos\phi \cos(\theta_K - \theta_0) + \sin\phi \sin(\theta_K - \theta_0)] - 2\rho_s \} \right\} \\ &= \delta \left\{ t - \frac{2\rho_s}{c} + \frac{\delta\rho_0 [\cos\phi \cos(\theta_K - \theta_0) + \sin\phi \sin(\theta_K - \theta_0)]}{c} \right\}. \end{aligned} \quad (2.4)$$

Next, it is helpful to define

$$\begin{aligned} \delta\rho_{s0} &= \delta\rho_0 [\cos\phi \cos(\theta_K - \theta_0) + \sin\phi \sin(\theta_K - \theta_0)] \\ &= \cos(\phi - \theta_K + \theta_0) \end{aligned} \quad (2.5)$$

so that the convolution portion of (2.2) can be simplified as

$$\begin{aligned} & -j\eta_0 \Delta I I_0 k_0^2 e^{j\omega_0 t} [h(t) - h(t - \tau_0)] * \delta \left[ t - \frac{2\rho_s - \delta\rho_{s0}}{c} \right] \\ &= -j\eta_0 \Delta I I_0 k_0^2 e^{j\omega_0 (t - \frac{2\rho_s - \delta\rho_{s0}}{c})} \cdot [h(t - \frac{2\rho_s - \delta\rho_{s0}}{c}) - h(t - \frac{2\rho_s - \delta\rho_{s0}}{c} - \tau_0)]. \end{aligned} \quad (2.6)$$

From the property of the Heaviside function, it is known that

$$h\left(t - \frac{2\rho_s - \delta\rho_{s0}}{c}\right) - h\left(t - \frac{2\rho_s - \delta\rho_{s0}}{c} - \tau_0\right) = \begin{cases} 1, & \frac{c(t-\tau_0) + \delta\rho_{s0}}{2} < \rho_s < \frac{ct + \delta\rho_{s0}}{2}; \\ 0, & \text{otherwise.} \end{cases} \quad (2.7)$$

As in [52], in order to simplify the integral in (2.2), at this point it is useful to define

$$\rho_{0s} = \frac{\frac{ct}{2} + \frac{c(t-\tau_0)}{2}}{2} = \frac{c(t - \frac{\tau_0}{2})}{2} \quad (2.8)$$

and

$$\rho_s' = \rho_s - \rho_{0s} \quad (2.9)$$

Then,

$$\frac{-c\tau_0/2 + \delta\rho_{s0}}{2} < \rho_s' < \frac{c\tau_0/2 + \delta\rho_{s0}}{2}. \quad (2.10)$$

Gill [3] also notes that  $\rho_s \approx \rho_{0s}$  and  $\rho_{0s} \gg |\rho_s'|$ , so that the phase term  $\rho_s(\pm K \cos \phi)$  in (2.2) may be expanded as

$$\rho_s(\pm K \cos \phi) \approx \pm K(\rho_{0s} \cos \phi_0 + \rho_s' / \cos \phi_0) \quad (2.11)$$

where  $\phi_0$  is a representative value of the bistatic angle, associated with  $\rho_{0s}$ . Since  $\rho_1$  and  $\rho_2$  exist in the magnitude term and vary only slightly over the patch, they may be denoted by representative values,  $\rho_{01}$  and  $\rho_{02}$ , and may be removed from the integral. Similarly,  $\rho_{0s} = \frac{\rho_{01} + \rho_{02}}{2}$  indicates the representative value of  $\rho_s$ . In addition,  $\rho_{0s}$  is a constant in the integral, so that  $d\rho_s = d\rho_s'$ . By changing the integration variable accordingly, (2.2) becomes

$$\begin{aligned} (E_n)_{1bf}(t) \approx & \frac{-j\eta_0 \Delta H_0 k_0^2}{(2\pi)^{3/2}} \sum_{\vec{K}} P_{\vec{K}} \sqrt{K} e^{\mp j\frac{\pi}{4}} e^{j\frac{\rho K}{2} \cos(\theta_K - \theta)} e^{j\omega_0 t} (\pm \sqrt{\cos \phi_0}) \\ & \cdot \frac{F(\rho_{01}, \omega_0) F(\rho_{02}, \omega_0)}{\sqrt{\rho_{0s} [\rho_{0s}^2 - (\rho/2)^2]}} e^{j\pm K \rho_{0s} \cos \phi_0} \\ & \cdot \int_{\rho_s'} e^{j\pm K \rho_s' / \cos \phi_0} e^{-jk_0(2\rho_s - \delta\rho_{s0})} d\rho_s', \end{aligned} \quad (2.12)$$

and the integral in (2.12) can be written as

$$\begin{aligned} I(\rho_s) &= \int_{\rho_s'} e^{\pm jK \rho_s' / \cos \phi_0} e^{-jk_0(2\rho_s - \delta\rho_{s0})} d\rho_s' \\ &= e^{-jk_0 2\rho_{0s}} e^{jk_0 \delta\rho_{s0}} \int_{\frac{-c\tau_0/2 + \delta\rho_{s0}}{2}}^{\frac{c\tau_0/2 + \delta\rho_{s0}}{2}} e^{j\rho_s' (\pm K / \cos \phi_0 - 2k_0)} d\rho_s'. \end{aligned} \quad (2.13)$$

Defining  $\rho_s'' = \rho_s' - \frac{\delta\rho_{s0}}{2}$ , (2.13) reduces to

$$\begin{aligned}
I(\rho_s) &= e^{-jk_0 2\rho_{0s}} e^{jk_0 \delta\rho_{s0}} \int_{-\frac{c\tau_0}{4}}^{\frac{c\tau_0}{4}} e^{j(\rho_s'' + \frac{\delta\rho_{s0}}{2})(\pm K/\cos\phi_0 - 2k_0)} d\rho_s'' \\
&= e^{-jk_0 2\rho_{0s}} e^{\pm j\frac{K\delta\rho_{s0}}{2\cos\phi_0}} \int_{-\frac{c\tau_0}{4}}^{\frac{c\tau_0}{4}} e^{j\rho_s''(\pm K/\cos\phi_0 - 2k_0)} d\rho_s'' \\
&= e^{-jk_0 2\rho_{0s}} \Delta\rho \\
&\cdot \left\{ e^{j\frac{K\delta\rho_{s0}}{2\cos\phi_0}} \text{Sa}\left[\frac{\Delta\rho}{2}\left(\frac{K}{\cos\phi_0} - 2k_0\right)\right] + e^{-j\frac{K\delta\rho_{s0}}{2\cos\phi_0}} \text{Sa}\left[\frac{\Delta\rho}{2}\left(\frac{K}{\cos\phi_0} + 2k_0\right)\right] \right\}.
\end{aligned} \tag{2.14}$$

Since the surface wavenumber  $K$  cannot be negative,  $\text{Sa}\left[\frac{\Delta\rho}{2}\left(\frac{K}{\cos\phi_0} + 2k_0\right)\right]$  is much smaller than  $\text{Sa}\left[\frac{\Delta\rho}{2}\left(\frac{K}{\cos\phi_0} - 2k_0\right)\right]$  for any bistatic radar parameters and  $K$  of interest, the contribution of the  $\text{Sa}\left[\frac{\Delta\rho}{2}\left(\frac{K}{\cos\phi_0} + 2k_0\right)\right]$  term in (2.14) is negligible relative to that of the  $\text{Sa}\left[\frac{\Delta\rho}{2}\left(\frac{K}{\cos\phi_0} - 2k_0\right)\right]$  term. Substituting (2.14) into (2.12) and using

$$e^{j\omega_0 t} e^{-jk_0 2\rho_{0s}} = e^{j\omega_0(t - \frac{2\rho_{0s}}{c})} = e^{j\frac{\omega_0}{c}(ct - 2(\frac{c(t-\tau_0)}{2}))} = e^{jk_0 \Delta\rho}, \tag{2.15}$$

the final received field may thus be obtained as [50], [53]

$$\begin{aligned}
(E_n)_{1bf}(t) &\approx \frac{-j\eta_0 \Delta I I_0 k_0^2}{(2\pi)^{3/2}} \sum_{\vec{K}} P_{\vec{K}} \sqrt{K \cos\phi_0} e^{jk_0 \Delta\rho} \frac{F(\rho_{01}, \omega_0) F(\rho_{02}, \omega_0)}{\sqrt{\rho_{0s} [\rho_{0s}^2 - (\rho/2)^2]}} \\
&\cdot e^{-j\frac{\pi}{4}} e^{jK\rho_{0s} \cos\phi_0} e^{j\frac{K\delta\rho_0}{2\cos\phi_0} [\cos\phi_0 \cos(\theta_K - \theta_0) + \sin\phi_0 \sin(\theta_K - \theta_0)]} \\
&\cdot e^{j\frac{\rho K}{2} \cos(\theta_K - \theta)} \Delta\rho \text{Sa}\left[\frac{\Delta\rho}{2}\left(\frac{K}{\cos\phi_0} - 2k_0\right)\right].
\end{aligned} \tag{2.16}$$

### C. First-Order Radar Cross Section

In keeping with the analysis presented in [51], the time-varying ocean surface  $\xi(x, y, t)$  is expressed as in (1.5). Instead of using  $P_{\vec{K}}$  as for the time-invariant case,  $P_{\vec{K}, \omega}$  is used for the Fourier coefficient for the time-varying rough surface. It is assumed that different Fourier coefficients  $P_{\vec{K}, \omega}$  are uncorrelated. Thus, the ensemble average of the

time-varying Fourier coefficient can be derived as

$$\langle P_{\vec{K}, \omega} P_{\vec{K}', \omega'}^* \rangle = \begin{cases} S_1(\vec{K}, \omega) d\vec{K} d\omega, & \vec{K} = \vec{K}', \omega = \omega'; \\ 0, & \text{otherwise.} \end{cases} \quad (2.17)$$

Introducing the time-varying ocean surface variation (1.5) into the received electric field (2.16), and using (1.6) to calculate the autocorrelation of the time-domain electric field gives

$$\begin{aligned} R(\tau) &= \frac{\lambda_0^2 G_r \eta_0 \Delta l^2 I_0^2 k_0^4}{8\pi} \frac{\Delta \rho^2}{(2\pi)^3 \rho_{0s} [\rho_{0s}^2 - (\rho/2)^2]} \int_{\vec{K}} \int_{\omega} K \cos \phi_0 S(\vec{K}, \omega) e^{j\omega\tau} \\ &\cdot |F(\rho_{01}, \omega_0) F(\rho_{02}, \omega_0)|^2 \text{Sa}^2 \left[ \frac{\Delta \rho}{2} \left( \frac{K}{\cos \phi_0} - 2k_0 \right) \right] \\ &\cdot \left\langle e^{\frac{-jK}{2\cos \phi_0} \delta \rho_0(t) \cos \phi_0 \cos(\theta_K - \theta_0(t))} e^{\frac{jK}{2\cos \phi_0} \delta \rho_0(t+\tau) \cos \phi_0 \cos(\theta_K - \theta_0(t+\tau))} \right. \\ &\cdot \left. e^{\frac{-jK}{2\cos \phi_0} \delta \rho_0(t) \sin \phi_0 \sin(\theta_K - \theta_0(t))} e^{\frac{jK}{2\cos \phi_0} \delta \rho_0(t+\tau) \sin \phi_0 \sin(\theta_K - \theta_0(t+\tau))} \right\rangle d\omega d\vec{K}. \end{aligned} \quad (2.18)$$

Taking the Fourier transform of (2.18), with respect to  $\tau$ , results in the Doppler power spectral density being

$$\begin{aligned} P(\omega_d) &= \frac{\lambda_0^2 G_r \eta_0 \Delta l^2 I_0^2 k_0^4}{8\pi} \frac{\Delta \rho^2}{(2\pi)^3 \rho_{0s} [\rho_{0s}^2 - (\rho/2)^2]} \int_{\vec{K}} \int_{\omega} K \cos \phi_0 \\ &\cdot |F(\rho_{01}, \omega_0) F(\rho_{02}, \omega_0)|^2 S(\vec{K}, \omega) \text{Sa}^2 \left[ \frac{\Delta \rho}{2} \left( \frac{K}{\cos \phi_0} - 2k_0 \right) \right] \\ &\cdot \int_{\tau} e^{j\tau(\omega - \omega_d)} \langle M(K, \theta_K, \tau, t) \rangle d\tau d\omega d\vec{K} \end{aligned} \quad (2.19)$$

where  $\omega_d$ , the Doppler radian frequency, is the transform variable in the frequency domain and

$$\begin{aligned} M(K, \theta_K, \tau, t) &= e^{\frac{-jK}{2\cos \phi_0} \delta \rho_0(t) \cos \phi_0 \cos(\theta_K - \theta_0(t))} \cdot e^{\frac{jK}{2\cos \phi_0} \delta \rho_0(t+\tau) \cos \phi_0 \cos(\theta_K - \theta_0(t+\tau))} \\ &\cdot e^{\frac{-jK}{2\cos \phi_0} \delta \rho_0(t) \sin \phi_0 \sin(\theta_K - \theta_0(t))} \cdot e^{\frac{jK}{2\cos \phi_0} \delta \rho_0(t+\tau) \sin \phi_0 \sin(\theta_K - \theta_0(t+\tau))}. \end{aligned} \quad (2.20)$$

Since  $d\theta_N = d\theta_K$ , (2.19) can be normalized in a per unit area sense as

$$\begin{aligned}
\frac{P(\omega_d)}{dA} &= P(\omega_d) \frac{\rho_{0s}[\rho_{0s}^2 - (\frac{\rho}{2})^2]}{\Delta\rho d\theta_N(\rho_{01}\rho_{02})^2} \\
&= \frac{\lambda_0^2 G_r \eta_0 \Delta l^2 I_0^2 k_0^4}{8\pi} \frac{\Delta\rho}{(2\pi)^3(\rho_{01}\rho_{02})^2} \int_K \int_\omega K^2 \cos\phi_0 |F(\rho_{01}, \omega_0) F(\rho_{02}, \omega_0)|^2 \\
&\quad \cdot S(\vec{K}, \omega) \text{Sa}^2\left[\frac{\Delta\rho}{2}\left(\frac{K}{\cos\phi_0} - 2k_0\right)\right] \int_\tau e^{j\tau(\omega - \omega_d)} \langle M(K, \theta_K, \tau, t) \rangle d\tau d\omega dK,
\end{aligned} \tag{2.21}$$

which may be compared with the radar range equation to obtain the radar cross section

$$\begin{aligned}
\sigma_{1bf}(\omega_d) &= 2^3 k_0^2 \Delta\rho \int_K \int_\omega K^2 \cos\phi_0 S(\vec{K}, \omega) \text{Sa}^2\left[\frac{\Delta\rho}{2}\left(\frac{K}{\cos\phi_0} - 2k_0\right)\right] \\
&\quad \cdot \int_\tau e^{j\tau(\omega - \omega_d)} \langle M(K, \theta_K, \tau, t) \rangle d\tau d\omega dK.
\end{aligned} \tag{2.22}$$

Next, it is noted that the power spectral density for first-order gravity waves can be expressed as [54]

$$S_1(\vec{K}, \omega) = \frac{1}{2} \sum_{m=\pm 1} S_1(m\vec{K}) \delta(\omega + m\sqrt{gK}). \tag{2.23}$$

Substituting (2.23) into (2.22) gives

$$\begin{aligned}
\sigma_{1bf}(\omega_d) &= 2^2 k_0^2 \Delta\rho \sum_{m=\pm 1} \int_K \int_\omega K^2 \cos\phi_0 S_1(m\vec{K}) \delta(\omega + m\sqrt{gK}) \\
&\quad \cdot \text{Sa}^2\left[\frac{\Delta\rho}{2}\left(\frac{K}{\cos\phi_0} - 2k_0\right)\right] \int_\tau e^{j\tau(\omega - \omega_d)} \langle M(K, \theta_K, \tau, t) \rangle d\tau d\omega dK.
\end{aligned} \tag{2.24}$$

The presence of the Dirac delta function  $\delta(\cdot)$  allows the  $\omega$  integration to be completed immediately and (2.24) reduces to

$$\begin{aligned}
\sigma_{1bf}(\omega_d) &= 2^2 k_0^2 \Delta\rho \sum_{m=\pm 1} \int_K K^2 \cos\phi_0 S_1(m\vec{K}) \text{Sa}^2\left[\frac{\Delta\rho}{2}\left(\frac{K}{\cos\phi_0} - 2k_0\right)\right] \\
&\quad \cdot \int_\tau e^{-j\tau(m\sqrt{gK} + \omega_d)} \langle M(K, \theta_K, \tau, t) \rangle d\tau dK.
\end{aligned} \tag{2.25}$$

Here,  $\langle M(K, \theta_K, \tau, t) \rangle$  should be more closely investigated. In keeping with [17], it is assumed that the platform sway is caused by the dominant ocean wave. Then,  $\langle M(K, \theta_K, \tau, t) \rangle$  can be written in terms of Bessel functions of the first kind (see Appendix B) as

$$\begin{aligned} \langle M(K, \theta_K, \tau, t) \rangle = & \\ & J_0^2 \left\{ \frac{aK}{2} [\cos(\theta_K - \theta_{K_p}) + \tan \phi_0 \sin(\theta_K - \theta_{K_p})] \right\} \\ & + 2 \sum_{n=1}^{\infty} J_n^2 \left\{ \frac{aK}{2} [\cos(\theta_K - \theta_{K_p}) + \tan \phi_0 \sin(\theta_K - \theta_{K_p})] \right\} \cdot \cos(n\omega_p \tau). \end{aligned} \quad (2.26)$$

Setting  $2 \cos(n\omega_p \tau) = e^{jn\omega_p \tau} + e^{-jn\omega_p \tau}$ , the  $\tau$  integral in (2.25) may be completed to give [50], [53]

$$\begin{aligned} \sigma_{1bf}(\omega_d) & \\ & = 2^3 \pi k_0^2 \Delta \rho \sum_{m=\pm 1} \int_K K^2 \cos \phi_0 S_1(m\vec{K}) \text{Sa}^2 \left[ \frac{\Delta \rho}{2} \left( \frac{K}{\cos \phi_0} - 2k_0 \right) \right] \\ & \cdot \left\{ J_0^2 \left\{ \frac{aK}{2} |\cos(\theta_1 - \theta_{K_p}) / \cos \phi_0| \right\} \cdot \delta(\omega_d + m\sqrt{gK}) \right. \\ & + \sum_{n=1}^{\infty} J_n^2 \left\{ \frac{aK}{2} |\cos(\theta_1 - \theta_{K_p}) / \cos \phi_0| \right\} \\ & \cdot \left[ \delta(\omega_d + m\sqrt{gK} - n\omega_p) + \delta(\omega_d + m\sqrt{gK} + n\omega_p) \right] \} dK. \end{aligned} \quad (2.27)$$

It is worth noting that the argument of the Bessel function  $J(v)$  must be nonnegative. In the Bessel function argument,  $\cos(\theta_K - \theta_{K_p}) + \tan \phi_0 \sin(\theta_K - \theta_{K_p}) = \cos(\theta_1 - \theta_{K_p}) / \cos \phi_0$ , whose value may be determined by the angle between the sway motion direction and the direction of  $\vec{\rho}_1$ , if the bistatic angle is known. Since the antenna motion is described by a sinusoidal function, it is known that the sway motion for the direction of  $\theta_{K_p}$  and  $\theta_{K_p} + 180^\circ$  should be the same. Therefore, the absolute value may be used for the term in the argument of the Bessel functions.

Equation (2.27) is the final result for the first-order bistatic ocean surface radar cross section with a floating transmitter and a fixed receiver. Clearly, (2.27) contains an infinite

sum of Bessel functions. However, the third-order and higher-order Bessel functions affect the total cross section very little. For this reason, when simulating the cross section, only the Bessel functions up to the second-order (i.e.,  $n = 0, 1, 2$ ) are used.

## 2.3 The Second-Order Radar Cross Section Model

### 2.3.1 The Second-Order Hydrodynamic Contribution

The first-order bistatic electric field for scatter from a time-invariant rough surface  $\xi(\vec{\rho})$  for the case of a floating transmitter and a fixed receiver was previously derived in (2.16).

The Fourier coefficient for the second-order ocean waves can be expressed as [51]

$$P_{\vec{K},\omega} = \sum_{\substack{\vec{K}=\vec{K}_1+\vec{K}_2 \\ \omega=\omega_1+\omega_2}} H\Gamma P_{\vec{K}_1,\omega_1} P_{\vec{K}_2,\omega_2} \quad (2.28)$$

Introducing the time-varying ocean surface displacement  $\xi(x,y,t)$  in (1.5) with the Fourier coefficient  $P_{\vec{K},\omega}$  in (2.28) to replace the time-invariant case  $\xi(x,y)$  in (1.3), (2.16) becomes the expression for the second-order bistatic field for scatter from the ocean surface for the case of a floating transmitter and a fixed receiver

$$\begin{aligned} (E_n)_{2bf}(t) = & \frac{-j\eta_0\Delta l I_0 k_0^2}{(2\pi)^{3/2}} \sum_{\vec{K}_1,\omega_1} \sum_{\vec{K}_2,\omega_2} H\Gamma P_{\vec{K}_1,\omega_1} P_{\vec{K}_2,\omega_2} e^{j(\omega_1+\omega_2)t} \Delta\rho \sqrt{K \cos\phi_0} \\ & \cdot e^{j\frac{\rho K}{2} \cos(\theta_K - \theta)} e^{jk_0\Delta\rho} \frac{F(\rho_{02}, \omega_0) F(\rho_{020}, \omega_0)}{\sqrt{\rho_{0s}[\rho_{0s}^2 - (\rho/2)^2]}} e^{-j\frac{\pi}{4}} e^{jK\rho_{0s} \cos\phi_0} \\ & \cdot e^{jK\delta\rho_0[\cos\phi_0 \cos(\theta_K - \theta_0) + \sin\phi_0 \sin(\theta_K - \theta_0)]/(2 \cos\phi_0)} \\ & \cdot Sa\left[\frac{\Delta\rho}{2} \left(\frac{K}{\cos\phi_0} - 2k_0\right)\right]. \end{aligned} \quad (2.29)$$

## 2.3.2 The Second-Order Electromagnetic Contribution

### A. General Second-Order Field Equation

The general second-order HFSWR scattered field for an antenna on a floating platform (see equation (1.11)) is derived in [18]. Based on Fig. 1.3, the double integral in (1.11) is defined as

$$I = \int_{A_2} F(\rho_{20}) e^{j\vec{k}_2 \cdot \vec{\rho}_2} \frac{e^{-jk\rho_{20}}}{\rho_{20}} \cdot \int_{A_1} (\vec{K}_1 \cdot \hat{\rho}_1)(\vec{K}_2 \cdot \hat{\rho}_{12}) e^{j\vec{K}_1 \cdot \vec{\rho}_1} e^{jk\hat{\rho}_1 \cdot \vec{\delta}\rho_0} F(\rho_1) F(\rho_{12}) \frac{e^{-jk(\rho_1 + \rho_{12})}}{\rho_1 \rho_{12}} dA_1 dA_2, \quad (2.30)$$

and the  $A_1$  integral in (2.30) can be expressed as

$$I_1 = \int_{A_1} (\vec{K}_1 \cdot \hat{\rho}_1)(\vec{K}_2 \cdot \hat{\rho}_{12}) e^{j\vec{K}_1 \cdot \vec{\rho}_1} e^{jk\hat{\rho}_1 \cdot \vec{\delta}\rho_0} F(\rho_1) F(\rho_{12}) \frac{e^{-jk(\rho_1 + \rho_{12})}}{\rho_1 \rho_{12}} dA_1. \quad (2.31)$$

### B. Patch Scatter Field Equation

Following the analyses in [44] and [49], for patch scatter, it is clear that  $\rho_{12} \ll \rho_1, \rho_2$ .

With the relationship  $\vec{\rho}_1 = \vec{\rho}_2 - \vec{\rho}_{12}$ , it can be shown that

$$\rho_1 \approx \rho_2 - \hat{\rho}_2 \cdot \vec{\rho}_{12}. \quad (2.32)$$

By using the approximations  $\rho_1 \approx \rho_2$  and  $\theta_1 \approx \theta_2$  in the magnitude factor in the integral  $I_1$ , (2.31) may be written as

$$I_1 = K_1 K_2 \cos(\theta_2 - \theta_{\vec{K}_1}) F(\rho_2) \frac{e^{-jk\rho_2}}{\rho_2} e^{jk\hat{\rho}_2 \cdot \vec{\delta}\rho_0} e^{j\vec{K}_1 \cdot \vec{\rho}_2} \cdot \int_{\rho_{12}} \int_{\theta_{12}} F(\rho_{12}) \cos(\theta_{12} - \theta_{\vec{K}_2}) e^{-jk\rho_{12}} e^{j\vec{\rho}_{12} \cdot [k\hat{\rho}_2 - \vec{K}_1]} d\theta_{12} d\rho_{12} \quad (2.33)$$

where  $dA_1 = \rho_{12}d\theta_{12}d\rho_{12}$  has been applied. By defining  $\vec{K}_s(K_s, \theta_s) = k\hat{\rho}_2 - \vec{K}_1$ , the integral in (2.33) may be written as

$$I_{11} = \int_{\rho_{12}} \int_{\theta_{12}} F(\rho_{12}) \cos(\theta_{12} - \theta_{\vec{K}_2}) e^{-jk\rho_{12}} e^{j\rho_{12}K_s \cos(\theta_{12} - \theta_s)} d\theta_{12} d\rho_{12}. \quad (2.34)$$

Since

$$\cos(\theta_{12} - \theta_{\vec{K}_2}) = \cos(\theta_{12} - \theta_s) \cos(\theta_s - \theta_{\vec{K}_2}) - \sin(\theta_{12} - \theta_s) \sin(\theta_s - \theta_{\vec{K}_2}) \quad (2.35)$$

and the term  $\sin(\theta_{12} - \theta_s) \sin(\theta_s - \theta_{\vec{K}_2})$  is an odd function that will vanish in the  $\theta_{12}$  integral, (2.34) becomes

$$I_{11} = \int_{\rho_{12}} F(\rho_{12}) \cos(\theta_s - \theta_{\vec{K}_2}) e^{-jk\rho_{12}} \cdot \int_{\theta_{12}} \cos(\theta_{12} - \theta_s) e^{j\rho_{12}K_s \cos(\theta_{12} - \theta_s)} d\theta_{12} d\rho_{12}. \quad (2.36)$$

By using the definition of the Bessel function of the first kind, the  $\theta_{12}$  integral in (2.36) may be written as

$$\begin{aligned} & \int_0^{2\pi} \cos(\theta_{12} - \theta_s) e^{j\rho_{12}K_s \cos(\theta_{12} - \theta_s)} d\theta_{12} \\ &= \int_0^{2\pi} \cos(\theta) e^{j\rho_{12}K_s \cos(\theta)} d\theta \\ &= 2\pi j J_1(\rho_{12}K_s). \end{aligned} \quad (2.37)$$

Substituting this result into (2.36) gives

$$\begin{aligned} I_{11} &= 2\pi j \cos(\theta_s - \theta_{\vec{K}_2}) \int_{\rho_{12}} F(\rho_{12}) e^{-jk\rho_{12}} J_1(\rho_{12}K_s) d\rho_{12} \\ &= 2\pi j \cos(\theta_s - \theta_{\vec{K}_2}) G(K_s) \\ &= 2\pi j \hat{K}_s \cdot \hat{K}_2 G(K_s) \end{aligned} \quad (2.38)$$

where  $G(K_s) = \int_{\rho_{12}} F(\rho_{12}) e^{-jk\rho_{12}} J_1(\rho_{12}K_s) d\rho_{12}$ . Further substitution of (2.38) into (2.33) yields

$$I_1 = K_1 K_2 \cos(\theta_2 - \theta_{\vec{K}_1}) F(\rho_2) \frac{e^{-jk\rho_2}}{\rho_2} e^{j\vec{K}_1 \cdot \vec{\rho}_2} e^{jk\hat{\rho}_2 \cdot \vec{\delta}\rho_0} [2\pi j \hat{K}_s \cdot \hat{K}_2 G(K_s)]. \quad (2.39)$$

Introducing this form of  $I_1$  into (2.30) results in

$$I = 2\pi j \int_{A_2} F(\rho_2) F(\rho_{20}) \frac{e^{-jk(\rho_2 + \rho_{20})}}{\rho_2 \rho_{20}} e^{j(\vec{K}_1 + \vec{K}_2) \cdot \vec{\rho}_2} \cdot e^{jk\hat{\rho}_2 \cdot \vec{\delta}\rho_0} (\vec{K}_1 \cdot \hat{\rho}_2) (\hat{K}_s \cdot \vec{K}_2) G[K_s(\hat{\rho}_2, \vec{K}_1)] dA_2, \quad (2.40)$$

so that (1.11) may be cast as

$$(E_n)_{2bf} \approx \frac{-kC_0}{(2\pi)^2} \sum_{\vec{K}_1} \sum_{\vec{K}_2} P_{\vec{K}_1} P_{\vec{K}_2} \cdot \int_{y_2} \int_{x_2} (-k\chi) \frac{F(\rho_2) F(\rho_{20})}{\rho_2 \rho_{20}} e^{jk\hat{\rho}_2 \cdot \vec{\delta}\rho_0} e^{-jk(\rho_2 + \rho_{20})} e^{jK\rho_2 \cos(\theta_K - \theta_2)} dx_2 dy_2 \quad (2.41)$$

where  $\chi = j(\vec{K}_1 \cdot \hat{\rho}_2) (\hat{K}_s \cdot \vec{K}_2) \cdot G[K_s(\hat{\rho}_2, \vec{K}_1)]$  and  $\vec{K} = \vec{K}_1 + \vec{K}_2$ .

By transforming from Cartesian to elliptic coordinates and applying a stationary phase method (see Appendix C), the bistatic electric field expression for scatter from a time-invariant rough surface becomes

$$(E_n)_{2bf} = \frac{-kC_0}{(2\pi)^{\frac{3}{2}}} \sum_{\vec{K}_1} \sum_{\vec{K}_2} \frac{P_{\vec{K}_1} P_{\vec{K}_2}}{\sqrt{K}} e^{j\frac{\rho}{2} K \cos(\theta_K - \theta)} e^{\mp j\frac{\pi}{4}} \cdot \int_{\frac{\rho}{2}}^{\infty} \frac{(-k\chi) F(\rho_2) F(\rho_{20})}{\sqrt{\cos\phi}} \frac{e^{j\rho_s(\pm K \cos\phi - 2k)}}{\sqrt{\rho_s(\rho_s^2 - (\frac{\rho}{2})^2)}} \cdot e^{jk\delta\rho_0[\cos\phi \cos(\theta_K - \theta_0) + \sin\phi \sin(\theta_K - \theta_0)]} d\rho_s. \quad (2.42)$$

### C. Pulsed Radar Field Equation

Following the analysis given for a pulsed dipole source in [50] and [51], and taking the inverse Fourier transform of (2.42), the time domain result for the second-order electric

field is

$$\begin{aligned}
(E_n)_{2bf}(t) &= \frac{-j\eta_0\Delta I I_0 k_0^2}{(2\pi)^{3/2}} \sum_{\vec{K}_1} \sum_{\vec{K}_2} \frac{P_{\vec{K}_1} P_{\vec{K}_2}}{\sqrt{K \cos \phi_0}} e^{jk_0 \Delta \rho} \\
&\cdot \frac{F(\rho_{02}, \omega_0) F(\rho_{020}, \omega_0) e^{-j\frac{\pi}{4}}}{\sqrt{\rho_{0s}(\rho_{0s}^2 - (\frac{\rho}{2})^2)}} (k_0 \chi) e^{jK \rho_{0s} \cos \phi_0} \\
&\cdot e^{jK \delta \rho_0 [\cos \phi_0 \cos(\theta_K - \theta_0) + \sin \phi_0 \sin(\theta_K - \theta_0)] / (2 \cos \phi_0)} \\
&\cdot e^{j\frac{\rho K}{2} \cos(\theta_K - \theta)} \Delta \rho \text{Sa} \left[ \frac{\Delta \rho}{2} \left( \frac{K}{\cos \phi_0} - 2k_0 \right) \right].
\end{aligned} \tag{2.43}$$

Defining  ${}_{BE}\Gamma_P = \frac{k_0 \chi}{K \cos \phi_0}$  as the electromagnetic coupling coefficient reduces (2.43) to

$$\begin{aligned}
(E_n)_{2bf}(t) &= \frac{-j\eta_0\Delta I I_0 k_0^2}{(2\pi)^{3/2}} \sum_{\vec{K}_1} \sum_{\vec{K}_2} {}_{BE}\Gamma_P P_{\vec{K}_1} P_{\vec{K}_2} e^{j\frac{\rho K}{2} \cos(\theta_K - \theta)} e^{jk_0 \Delta \rho} \\
&\cdot \sqrt{K \cos \phi_0} \frac{F(\rho_{02}, \omega_0) F(\rho_{020}, \omega_0) e^{-j\frac{\pi}{4}}}{\sqrt{\rho_{0s}(\rho_{0s}^2 - (\frac{\rho}{2})^2)}} e^{jK \rho_{0s} \cos \phi_0} \\
&\cdot e^{jK \delta \rho_0 [\cos \phi_0 \cos(\theta_K - \theta_0) + \sin \phi_0 \sin(\theta_K - \theta_0)] / (2 \cos \phi_0)} \\
&\cdot \Delta \rho \text{Sa} \left[ \frac{\Delta \rho}{2} \left( \frac{K}{\cos \phi_0} - 2k_0 \right) \right].
\end{aligned} \tag{2.44}$$

Replacing the time-invariant rough surface by the time-varying ocean surface, (2.44) can be written as

$$\begin{aligned}
(E_n)_{2bf}(t) &= \frac{-j\eta_0\Delta I I_0 k_0^2}{(2\pi)^{3/2}} \sum_{\vec{K}_1, \omega_1} \sum_{\vec{K}_2, \omega_2} {}_{BE}\Gamma_P P_{\vec{K}_1, \omega_1} P_{\vec{K}_2, \omega_2} e^{j\frac{\rho K}{2} \cos(\theta_K - \theta)} e^{j(\omega_1 + \omega_2)t} \\
&\cdot \sqrt{K \cos \phi_0} e^{jk_0 \Delta \rho} \frac{F(\rho_{02}, \omega_0) F(\rho_{020}, \omega_0)}{\sqrt{\rho_{0s}[\rho_{0s}^2 - (\rho/2)^2]}} e^{-j\frac{\pi}{4}} e^{jK \rho_{0s} \cos \phi_0} \\
&\cdot e^{jK \delta \rho_0 [\cos \phi_0 \cos(\theta_K - \theta_0) + \sin \phi_0 \sin(\theta_K - \theta_0)] / (2 \cos \phi_0)} \\
&\cdot \Delta \rho \text{Sa} \left[ \frac{\Delta \rho}{2} \left( \frac{K}{\cos \phi_0} - 2k_0 \right) \right].
\end{aligned} \tag{2.45}$$

Replacing the electromagnetic coupling coefficient  ${}_{BE}\Gamma_P$  with its symmetrical counterpart  ${}_{SE}\Gamma_P$ , which is derived in Appendix D, gives the final second-order electromagnetic

electric field

$$\begin{aligned}
(E_n)_{2bf}(t) &= \frac{-j\eta_0\Delta l I_0 k_0^2}{(2\pi)^{3/2}} \sum_{\vec{K}_1, \omega_1} \sum_{\vec{K}_2, \omega_2} {}_{SE}\Gamma_P P_{\vec{K}_1, \omega_1} P_{\vec{K}_2, \omega_2} e^{j(\omega_1 + \omega_2)t} \sqrt{K \cos \phi_0} \\
&\cdot \frac{F(\rho_{02}, \omega_0) F(\rho_{020}, \omega_0)}{\sqrt{\rho_{0s} [\rho_{0s}^2 - (\rho/2)^2]}} e^{j\frac{\rho K}{2} \cos(\theta_K - \theta)} e^{jk_0 \Delta \rho} e^{-j\frac{\pi}{4}} e^{jK\rho_{0s} \cos \phi_0} \\
&\cdot e^{jK\delta\rho_0 [\cos \phi_0 \cos(\theta_K - \theta_0) + \sin \phi_0 \sin(\theta_K - \theta_0)] / (2 \cos \phi_0)} \\
&\cdot \Delta\rho \text{Sa} \left[ \frac{\Delta\rho}{2} \left( \frac{K}{\cos \phi_0} - 2k_0 \right) \right].
\end{aligned} \tag{2.46}$$

### 2.3.3 Second-Order Radar Cross Section For Patch Scatter

From (2.29) and (2.46), the total second-order scattering field, including both the electromagnetic portion and the hydrodynamic portion, can be expressed as [55] and [56]

$$\begin{aligned}
(E_n)_{2bf}(t) &= \frac{-j\eta_0\Delta l I_0 k_0^2}{(2\pi)^{3/2}} \sum_{\vec{K}_1, \omega_1} \sum_{\vec{K}_2, \omega_2} \Gamma_{P_b} P_{\vec{K}_1, \omega_1} P_{\vec{K}_2, \omega_2} e^{j(\omega_1 + \omega_2)t} \sqrt{K \cos \phi_0} \\
&\cdot \frac{F(\rho_{02}, \omega_0) F(\rho_{020}, \omega_0)}{\sqrt{\rho_{0s} [\rho_{0s}^2 - (\rho/2)^2]}} e^{-j\frac{\pi}{4}} e^{jK\rho_{0s} \cos \phi_0} e^{j\frac{\rho K}{2} \cos(\theta_K - \theta)} e^{jk_0 \Delta \rho} \\
&\cdot e^{jK\delta\rho_0 [\cos \phi_0 \cos(\theta_K - \theta_0) + \sin \phi_0 \sin(\theta_K - \theta_0)] / (2 \cos \phi_0)} \\
&\cdot \Delta\rho \text{Sa} \left[ \frac{\Delta\rho}{2} \left( \frac{K}{\cos \phi_0} - 2k_0 \right) \right]
\end{aligned} \tag{2.47}$$

where  $\Gamma_{P_b} = {}_{SE}\Gamma_P + {}_H\Gamma$ . A similar process, as was used in [50] and [51], is used to obtain the radar cross section from the electric field equation. The initial step of the approach is to write the autocorrelation,  $R(\tau)$ , as

$$\begin{aligned}
R(\tau) &= \frac{A_r}{2\eta_0} \langle (E_n)_{2bf}(t_0, t_0 + \tau) (E_n)_{2bf}^*(t_0, t_0) \rangle \\
&= \frac{A_r}{2\eta_0} \left\{ \frac{\eta_0^2 k_0^4 |\Delta l I_0|^2 (\Delta\rho)^2}{2(2\pi)^3 \rho_{0s} [\rho_{0s}^2 - (\rho/2)^2]} \right\} \sum_{m_1 = \pm 1} \sum_{m_2 = \pm 1} \int_{-\pi}^{\pi} \int_0^{\infty} \int_{-\pi}^{\pi} \int_0^{\infty} \\
&\cdot \{S_1(m_1 \vec{K}_1) S_1(m_2 \vec{K}_2) e^{j\omega\tau} |\Gamma_{P_b}|^2 K^2 \cos \phi_0 |F(\rho_{02}, \omega_0) F(\rho_{020}, \omega_0)|^2 \\
&\cdot \langle M(K, \theta_K, \tau, t) \rangle \text{Sa}^2 \left[ \frac{\Delta\rho}{2} \left( \frac{K}{\cos \phi_0} - 2k_0 \right) \right] K_1 \} dK_1 d\theta_{\vec{K}_1} dK d\theta_{\vec{K}}
\end{aligned} \tag{2.48}$$

where  $M(K, \theta_K, \tau, t)$  is defined in (2.20).

A Fourier transform of (2.48) with respect to  $\tau$  gives the received power spectral density spectrum

$$\begin{aligned}
P(\omega_d) &= \frac{A_r \eta_0 k_0^4 |\Delta I I_0|^2 (\Delta \rho)^2}{4(2\pi)^3 \rho_{0s} [\rho_{0s}^2 - (\rho/2)^2]} \sum_{m_1=\pm 1} \sum_{m_2=\pm 1} \int_{-\pi}^{\pi} \int_0^{\infty} \int_{-\pi}^{\pi} \int_0^{\infty} \\
&\cdot \{S_1(m_1 \vec{K}_1) S_1(m_2 \vec{K}_2) |\Gamma_{P_b}|^2 K^2 \cos \phi_0 \\
&\cdot |F(\rho_{02}, \omega_0) F(\rho_{020}, \omega_0)|^2 \text{Sa}^2 \left[ \frac{\Delta \rho}{2} \left( \frac{K}{\cos \phi_0} - 2k_0 \right) \right] K_1 \} \\
&\cdot \int_{\tau} e^{j\tau(\omega - \omega_d)} \langle M(K, \theta_K, \tau, t) \rangle d\tau dK_1 d\theta_{\vec{K}_1} dK d\theta_{\vec{K}}.
\end{aligned} \tag{2.49}$$

The result in (2.49) may be normalized in a per unit area sense as

$$\begin{aligned}
\frac{P(\omega_d)}{dA} &= P(\omega_d) \frac{\rho_{0s} [\rho_{0s}^2 - (\frac{\rho}{2})^2]}{\Delta \rho d\theta_N (\rho_{02} \rho_{020})^2} \\
&= P(\omega_d) \frac{\rho_{0s} [\rho_{0s}^2 - (\frac{\rho}{2})^2]}{\Delta \rho d\theta_K (\rho_{02} \rho_{020})^2} \\
&= \frac{A_r \eta_0 k_0^4 |\Delta I I_0|^2 \Delta \rho}{4(2\pi)^3 (\rho_{02} \rho_{020})^2} \sum_{m_1=\pm 1} \sum_{m_2=\pm 1} \int_0^{\infty} \int_{-\pi}^{\pi} \int_0^{\infty} \{S_1(m_1 \vec{K}_1) S_1(m_2 \vec{K}_2) \\
&\cdot |\Gamma_{P_b}|^2 K^2 \cos \phi_0 |F(\rho_{02}, \omega_0) F(\rho_{020}, \omega_0)|^2 \text{Sa}^2 \left[ \frac{\Delta \rho}{2} \left( \frac{K}{\cos \phi_0} - 2k_0 \right) \right] K_1 \\
&\int_{\tau} e^{j\tau(\omega - \omega_d)} \langle M(K, \theta_K, \tau, t) \rangle d\tau dK_1 d\theta_{\vec{K}_1} dK \},
\end{aligned} \tag{2.50}$$

and this may be compared directly with the radar range equation to obtain the cross section

$$\begin{aligned}
\sigma_{2bf}(\omega_d) &= 2^2 k_0^2 \Delta \rho \sum_{m_1=\pm 1} \sum_{m_2=\pm 1} \int_0^{\infty} \int_{-\pi}^{\pi} \int_0^{\infty} \\
&\cdot \{S_1(m_1 \vec{K}_1) S_1(m_2 \vec{K}_2) |\Gamma_{P_b}|^2 K^2 K_1 \cos \phi_0 \text{Sa}^2 \left[ \frac{\Delta \rho}{2} \left( \frac{K}{\cos \phi_0} - 2k_0 \right) \right] \\
&\cdot \int_{\tau} e^{-j\tau(m_1 \sqrt{gK_1} + m_2 \sqrt{gK_2} + \omega_d)} \langle M(K, \theta_K, \tau, t) \rangle d\tau dK_1 d\theta_{\vec{K}_1} dK \}
\end{aligned} \tag{2.51}$$

where  $\langle M(K, \theta_K, \tau, t) \rangle$  is addressed in Appendix B. Substituting (B.5) into (2.51) and setting  $2 \cos(n\omega_p \tau) = e^{jn\omega_p \tau} + e^{-jn\omega_p \tau}$ , the  $\tau$  integral may be completed to give [55], [56]

$$\begin{aligned}
\sigma_{2bf}(\omega_d) = & 2^3 \pi k_0^2 \Delta \rho \sum_{m_1=\pm 1} \sum_{m_2=\pm 1} \int_0^\infty \int_{-\pi}^\pi \int_0^\infty \\
& \cdot S_1(m_1 \vec{K}_1) S_1(m_2 \vec{K}_2) |\Gamma_{P_b}|^2 K^2 K_1 \cos \phi_0 \text{Sa}^2 \left[ \frac{\Delta \rho}{2} \left( \frac{K}{\cos \phi_0} - 2k_0 \right) \right] \\
& \cdot \left\{ J_0^2 \left\{ \frac{aK}{2} \left| \cos(\theta_K - \theta_{K_p}) + \tan \phi_0 \sin(\theta_K - \theta_{K_p}) \right| \right\} \right. \\
& \cdot \delta(\omega_d + m_1 \sqrt{gK_1} + m_2 \sqrt{gK_2}) \\
& + \sum_{n=1}^\infty J_n^2 \left\{ \frac{aK}{2} \left| \cos(\theta_K - \theta_{K_p}) + \tan \phi_0 \sin(\theta_K - \theta_{K_p}) \right| \right\} \\
& \cdot [\delta(\omega_d + m_1 \sqrt{gK_1} + m_2 \sqrt{gK_2} - n\omega_p) \\
& \left. + \delta(\omega_d + m_1 \sqrt{gK_1} + m_2 \sqrt{gK_2} + n\omega_p)] \right\} dK_1 d\theta_{\vec{K}_1} dK.
\end{aligned} \tag{2.52}$$

Equation (2.52) is the final result for the second-order bistatic ocean surface radar cross section with a floating transmitter and a fixed receiver.

## 2.4 Comparisons of Antenna-Motion Incorporated Bistatic Radar Cross Sections with Earlier Models

### A. Comparison with a Monostatic Model

For monostatic cases,  $\phi_0 = 0$ , i.e.  $\cos \phi_0 = 1$  and  $\tan \phi_0 = 0$ . Then, (2.27) becomes

$$\begin{aligned}
\sigma_1(\omega_d) = & 2^3 \pi k_0^2 \Delta \rho \sum_{m=\pm 1} \int_K K^2 S_1(m \vec{K}) \text{Sa}^2 \left[ \frac{\Delta \rho}{2} (K - 2k_0) \right] \\
& \cdot \left\{ J_0^2 \left\{ \left| \frac{aK}{2} \cos(\theta_K - \theta_{K_p}) \right| \right\} \delta(\omega_d + m \sqrt{gK}) \right. \\
& + \sum_{n=1}^\infty J_n^2 \left\{ \left| \frac{aK}{2} \cos(\theta_K - \theta_{K_p}) \right| \right\} \\
& \left. \cdot [\delta(\omega_d + m \sqrt{gK} - n\omega_p) + \delta(\omega_d + m \sqrt{gK} + n\omega_p)] \right\} dK,
\end{aligned} \tag{2.53}$$

which is the same as the monostatic model with a floating transmitter and a fixed receiver given in [74]. It is worth noting that (2.53) differs from its counterpart (1.8), where both transmitter and receiver are assumed to be floating, by having a  $\frac{aK}{2} \cos(\theta_K - \theta_{K_p})$  factor in the Bessel functions instead of a  $aK \cos(\theta_K - \theta_{K_p})$  factor.

For the second-order radar cross section, (2.52) reduces to

$$\begin{aligned}
\sigma_2(\omega_d) = & 2^3 \pi k_0^2 \Delta \rho \sum_{m_1=\pm 1} \sum_{m_2=\pm 1} \int_0^\infty \int_{-\pi}^\pi \int_0^\infty \\
& \cdot S_1(m_1 \vec{K}_1) S_1(m_2 \vec{K}_2) |\Gamma_{P_b}|^2 K^2 K_1 \text{Sa}^2 \left[ \frac{\Delta \rho}{2} (K - 2k_0) \right] \\
& \cdot \left\{ J_0^2 \left\{ \frac{1}{2} aK |\cos(\theta_K - \theta_{K_p})| \right\} \delta(\omega_d + m_1 \sqrt{gK_1} + m_2 \sqrt{gK_2}) \right. \\
& + \sum_{n=1}^\infty J_n^2 \left\{ \frac{1}{2} aK |\cos(\theta_K - \theta_{K_p})| \right\} [\delta(\omega_d + m_1 \sqrt{gK_1} + m_2 \sqrt{gK_2} - n\omega_p) \\
& \left. + \delta(\omega_d + m_1 \sqrt{gK_1} + m_2 \sqrt{gK_2} + n\omega_p)] \right\} dK_1 d\theta_{\vec{K}_1} dK.
\end{aligned} \tag{2.54}$$

Considering the Bessel function property,  $J_n^2 = J_{-n}^2$ , (2.54) can be written as

$$\begin{aligned}
\sigma_2(\omega_d) = & 2^3 \pi k_0^2 \Delta \rho \sum_{m_1=\pm 1} \sum_{m_2=\pm 1} \int_0^\infty \int_{-\pi}^\pi \int_0^\infty S_1(m_1 \vec{K}_1) S_1(m_2 \vec{K}_2) |\Gamma_{P_b}|^2 K^2 K_1 \\
& \cdot \text{Sa}^2 \left[ \frac{\Delta \rho}{2} (K - 2k_0) \right] \sum_{n=-\infty}^\infty J_n^2 \left\{ \frac{1}{2} aK |\cos(\theta_K - \theta_{K_p})| \right\} \\
& \cdot \delta(\omega_d + m_1 \sqrt{gK_1} + m_2 \sqrt{gK_2} + n\omega_p) dK_1 d\theta_{\vec{K}_1} dK.
\end{aligned} \tag{2.55}$$

For a large patch width  $\Delta \rho$ ,  $\lim_{M \rightarrow \infty} M \text{Sa}^2[Mx] = \pi \delta(x)$ . It is straightforward to show that in this case

$$\Delta \rho \text{Sa}^2 \left[ \frac{\Delta \rho}{2} (K - 2k_0) \right] = 2\pi \delta(K - 2k_0). \tag{2.56}$$

Carrying out the  $K$  integration, (2.55) reduces to

$$\begin{aligned}
\sigma_2(\omega_d) = & 2^6 \pi^2 k_0^4 \sum_{m_1=\pm 1} \sum_{m_2=\pm 1} \int_0^\infty \int_{-\pi}^\pi |\Gamma_{P_b}|^2 S_1(m_1 \vec{K}_1) S_1(m_2 \vec{K}_2) K_1 \\
& \cdot \sum_{n=-\infty}^\infty J_n^2\{ak_0 |\cos(\theta_K - \theta_{K_p})|\} \\
& \cdot \delta(\omega_d + m_1 \sqrt{gK_1} + m_2 \sqrt{gK_2} + n\omega_p) d\theta_{\vec{K}_1} dK_1.
\end{aligned} \tag{2.57}$$

Except for the term in the Bessel functions, equation (2.57) is of the same form as (1.14). It has been explained that (1.14) is the model for the monostatic radar cross section when both the transmitter and receiver are floating. If the term  $2k_0a |\cos(\theta_K - \theta_{K_p})|$  appearing in the argument of the Bessel functions of the first kind is replaced by the term  $k_0a |\cos(\theta_K - \theta_{K_p})|$ , then the model is reduced to the monostatic radar cross section involving a floating transmitter and a fixed receiver. Next, it will be illustrated that the coefficient  $\Gamma_{P_b}$  in (2.57) has the same value as the coefficient  $\Gamma_{P_m}$  in (1.14), when the bistatic geometry is reduced to the monostatic case. The hydrodynamic coefficients  $H\Gamma$  in both coefficients remain unchanged, so only the electromagnetic coefficients need to be addressed. For the monostatic case,  $\phi_0 = 0$  and  $\hat{\rho}_2 = \hat{N} = \hat{K}$ . Also, it can be shown that

$$\begin{aligned}
\vec{K} &= \vec{K}_1 + \vec{K}_2 = 2k_0\hat{K} \\
\vec{K}_s(\hat{\rho}_2, \vec{K}_1) &= k_0\hat{\rho}_2 - \vec{K}_1 = \frac{\vec{K}_2 - \vec{K}_1}{2} = -\vec{K}_s(\hat{\rho}_2, \vec{K}_2), \\
K_s^2(\hat{\rho}_2, \vec{K}_1) &= k_0^2 - \vec{K}_1 \cdot \vec{K}_2 = K_s^2(\hat{\rho}_2, \vec{K}_2),
\end{aligned}$$

and

$$G[K_s(\hat{\rho}_2, \vec{K}_1)] = G[K_s(\hat{\rho}_2, \vec{K}_2)].$$

Thus,  ${}_{SE}\Gamma_P$  in (D.9) reduces to

$$\begin{aligned}
{}_{SE}\Gamma_P(\vec{K}_1, \vec{K}_2) &= \frac{jk_0}{2K^2K_s} G[K_s(\hat{\rho}_2, \vec{K}_2)] \\
&\cdot \{ [\vec{K}_1 \cdot (\vec{K}_1 + \vec{K}_2)] \left[ \frac{\vec{K}_2 - \vec{K}_1}{2} \cdot \vec{K}_2 \right] - [\vec{K}_2 \cdot (\vec{K}_1 + \vec{K}_2)] \left[ \frac{\vec{K}_2 - \vec{K}_1}{2} \cdot \vec{K}_1 \right] \} \\
&= \frac{jk_0}{2K^2K_s} G[K_s(\hat{\rho}_2, \vec{K}_2)] [(K_1K_2)^2 - (\vec{K}_1 \cdot \vec{K}_2)^2] \\
&= \frac{jk_0}{2K^2K_s} G[K_s(\hat{\rho}_2, \vec{K}_2)] |\vec{K}_1 \times \vec{K}_2|^2 \\
&= \frac{jk_0}{2K^2} \frac{|\vec{K}_1 \times \vec{K}_2|^2}{k_0^2 - \vec{K}_1 \cdot \vec{K}_2} \left\{ 1 - j \frac{k_0(1+\Delta)}{\sqrt{-\vec{K}_1 \cdot \vec{K}_2 + jk_0\Delta}} \right\}
\end{aligned} \tag{2.58}$$

which is exactly the same as the monostatic electromagnetic coupling coefficient (1.13).

## B. Comparison with a Stationary Model

For a model involving a stationary antenna platform,  $\delta\vec{\rho}_0 = 0$  and  $a = 0$ ,  $\omega_p = 0$ . In addition, it is known that  $J_0(0) = 1$ ,  $J_n(0) = 0$ . Under these conditions, (2.27) becomes

$$\begin{aligned}
\sigma_1(\omega_d) &= 2^3 \pi k_0^2 \Delta \rho \sum_{m=\pm 1} \int_K K^2 \cos \phi_0 S_1(m\vec{K}) \\
&\cdot \text{Sa}^2 \left[ \frac{\Delta \rho}{2} \left( \frac{K}{\cos \phi_0} - 2k_0 \right) \right] \delta(\omega_d + m\sqrt{gK}) dK.
\end{aligned} \tag{2.59}$$

Due to the Dirac delta function,  $K = \frac{\omega_d^2}{g}$ , so that  $dK = \frac{2\omega_d d\omega_d}{g} = \frac{2\sqrt{K}}{\sqrt{g}} d\omega_d$ . Thus, (2.59) may be written as

$$\sigma_1(\omega_d) = \frac{2^4 \pi k_0^2 \Delta \rho}{\sqrt{g}} \sum_{m=\pm 1} K^{\frac{5}{2}} \cos \phi_0 S_1(m\vec{K}) \text{Sa}^2 \left[ \frac{\Delta \rho}{2} \left( \frac{K}{\cos \phi_0} - 2k_0 \right) \right] \tag{2.60}$$

which is identical to the stationary bistatic model in [51].

Similarly, for the second-order radar cross section, (2.52) reduces to

$$\begin{aligned}
\sigma_2(\omega_d) = & 2^3 \pi k_0^2 \Delta \rho \sum_{m_1=\pm 1} \sum_{m_2=\pm 1} \int_0^\infty \int_{-\pi}^\pi \int_0^\infty \{S_1(m_1 \vec{K}_1) S_1(m_2 \vec{K}_2) \\
& \cdot |\Gamma_P|^2 K^2 K_1 \cos \phi_0 S a^2 \left[ \frac{\Delta \rho}{2} \left( \frac{K}{\cos \phi_0} - 2k_0 \right) \right] \\
& \cdot \delta(\omega_d + m_1 \sqrt{gK_1} + m_2 \sqrt{gK_2}) dK_1 d\theta_{\vec{K}_1} dK \}
\end{aligned} \tag{2.61}$$

which is the same as the bistatic model for the stationary antenna case shown in [51]. It is worth noting that the coefficient  $\Gamma_{P_b}$  has been modified compared to Gill's [51]. Here, it is not assumed that  $F(\rho_{12}) \approx 1$ , when  $\rho_{12}$  is a very small value compared to  $\rho_1$  and  $\rho_2$ . Instead, the properties of the Sommerfeld function are used, producing the surface impedance  $\Delta$  in the final result. The modified coefficient avoids a non-physical singularity in the radar cross section.  $\Delta$  is a very small value. For example, at an operating frequency of 15 MHz, it is approximately  $0.0103 + j0.01$ . Setting  $\Delta = 0$ , the modified coefficient will reduce to the coefficient shown in [51].

## 2.5 Simulation and Analysis

The RCS models here are computed using a Pierson-Moskowitz model [57] with a cardioid directional distribution for the directional ocean wave height spectrum of a fully developed wind driven sea. For the simulations considered here, the operating frequency is chosen to be 25 MHz, the bistatic angle is  $30^\circ$ , the patch width is 3000 m, and the ellipse normal  $\theta_N$  (illustrated Fig. A.1 in Appendix A of this thesis) is  $90^\circ$ . The direction of the barge motion is taken to be the same as the wind direction, which is at  $90^\circ$  with respect to the ellipse normal. In keeping with [17], the platform sway is assumed to be due to the dominant ocean wave. The sway amplitude and frequency depend on the wind velocity and are given in Table 2.1 (also in [17]). In addition, a Hamming window is used to smooth the curve and reduce oscillatory features caused by the  $Sa^2$  function.

Table 2.1 Barge motion parameters [17]

Wind Speed (knots*)	Sea State	Sway Amplitude (m)	Sway frequency (Hz)
10	2	0.177	0.261
15	3 to 4	0.581	0.174
20	5	1.228	0.127
*1 knot = 0.5148 m/s			

Fig. 2.2 presents a comparison of the first-order bistatic radar cross section for a fixed transmitter and receiver with that of a floating transmitter and a fixed receiver. From this figure, additional peaks due to platform motion are observed. The Bragg peaks for both cases are located at their usual positions of  $\pm f_B = \pm \sqrt{2gk_0 \cos \phi_0} / 2\pi$ . The motion-induced peaks are symmetrically distributed at  $\pm f_B \pm f_p$  and  $\pm f_B \pm 2f_p$ , where  $f_p = \omega_p / 2\pi$ .

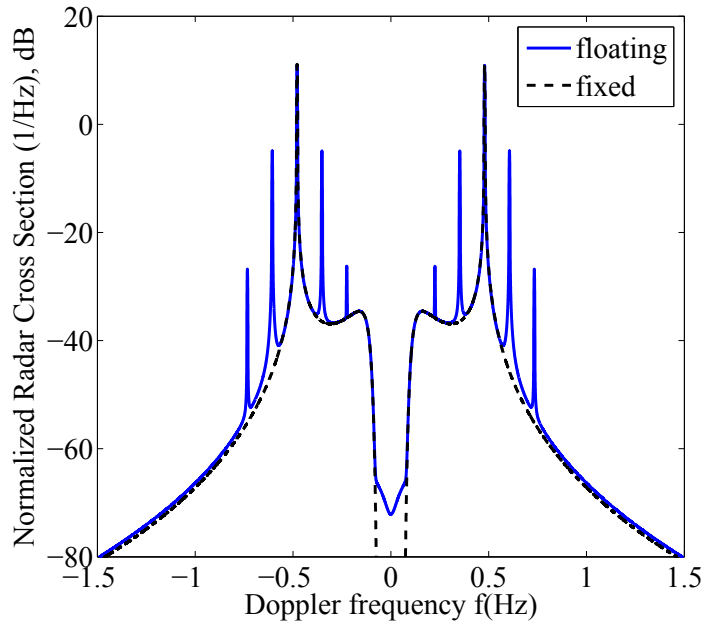


Fig. 2.2 Comparison of the first-order bistatic radar cross section for both transmitter and receiver fixed with that for a floating transmitter and a fixed receiver.

Fig. 2.3 illustrates the effect of radial patch width on the RCS. From the RCS models derived in Section 2.2, the magnitude of both Bragg peaks and antenna-motion-induced peaks are expected to increase with the increasing patch width. The radar cross sections

in Fig. 2.3 are normalized in order to clearly observe the magnitude difference. The energies of the motion-induced peaks are seen to increase with the increasing patch width. However, the relative differences between each peak are essentially unchanged with patch width.

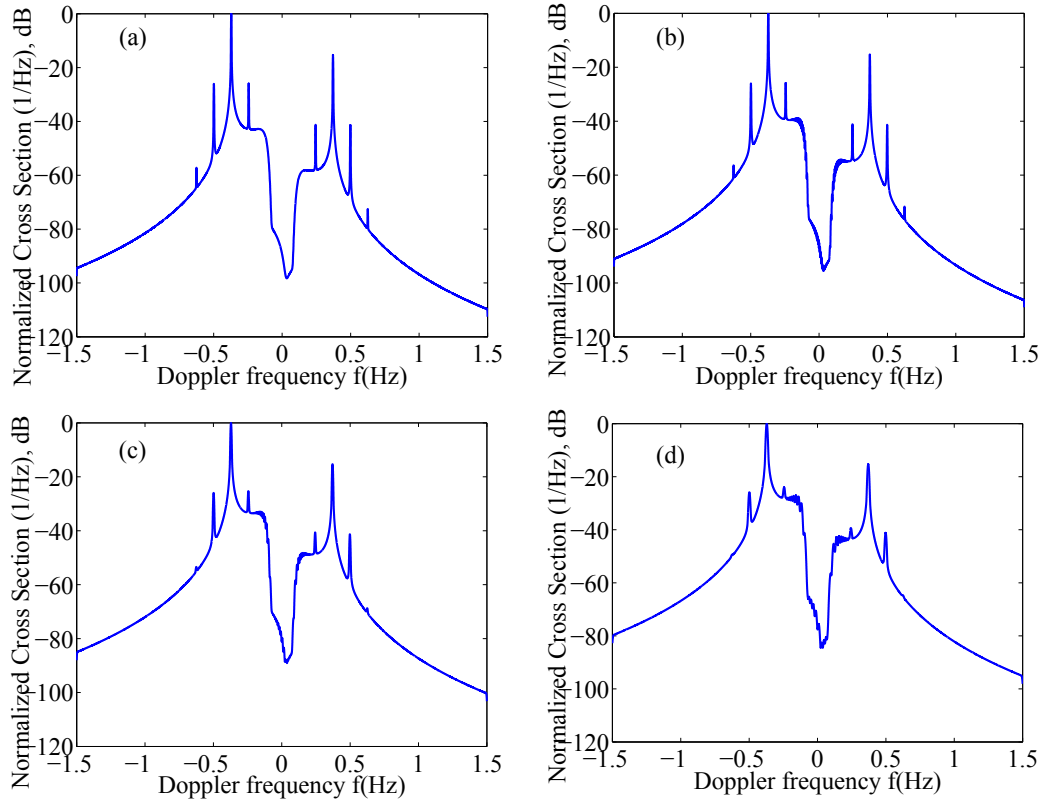


Fig. 2.3 The effect of radial patch width on the first-order cross section. The patch width is (a) 2000 m, (b) 1000 m, (c) 500 m, (d) 250 m.

Fig. 2.4(a) and Fig. 2.4(b) show the second-order hydrodynamic results without and with antenna motion, respectively.  $h1$  represents the hydrodynamic peak at  $\pm\sqrt{2}f_B$ , where  $f_B$  represents the Doppler frequency of the Bragg peak. The physical meaning of this peak is a single scatter from a second-order ocean surface component of wave length  $\lambda_B$ , where  $\lambda_B = c/f_B$ . From Fig. 2.4(b), extra hydrodynamic peaks  $h2$  at  $\pm\sqrt{2}f_B \pm f_p$  due to the platform motion are observed. Fig. 2.4(c) and Fig. 2.4(d) depict the second-order electromagnetic results without and with antenna motion, respectively. Electromagnetic

peaks  $e1$  and  $e2$  occur for [49]

$$K_1 = K_2$$

and

$$f_d = \pm 2^{\frac{3}{4}} \sqrt{\frac{[1 \pm \sin \phi_0]^{\frac{1}{2}}}{\cos \phi_0}} f_B.$$

For monostatic operation, (i.e.  $\phi_0 = 0$ ), the four peaks are reduced to two peaks at  $f_d = \pm 2^{\frac{3}{4}} f_B$ , which is the well known ‘corner reflector’ condition. By comparing Fig. 2.4(c) and Fig. 2.4(d), it may be observed that  $e1$  and  $e2$  are shifted in the spectrum at  $f_d \pm f_p$ , labelled as  $e3$  and  $e4$ . In Figs. 2.4(b) and (d), the gaps around  $\pm 0.4$  Hz in the second-order Doppler spectra are seen to be raised by these  $e3$  and  $e4$  peaks. In these figures, motion effects need be considered only up to second-order for the first-order radar cross section and up to first-order for the second-order radar cross section. This is because the energies of the motion-induced peaks in the second-order radar cross section are significantly lower than that of the first-order result. In total, the second-order hydrodynamic contribution is greater than that of the electromagnetic contribution.

Discussion regarding the first-order bistatic result for the case with a floating transmitter and a fixed receiver can be found in [50]. The total bistatic radar patch scatter cross sections to second-order for stationary antennas and floating antennas are shown in Figs. 2.4(e) and (f), respectively. It should be noted that, unlike the field observation results in [11], no motion-induced spreading is seen in the first-order peaks in the sea echo Doppler spectra presented here because a simple sinusoidal motion model with a single frequency is used and an extreme narrow antenna beam is assumed. In reality, it is anticipated that the region of the first-order peaks will be broadened due to various wave component contributions.

Fig. 2.5 illustrates the total bistatic radar cross section (including the first- and second-order) for a floating transmitter and a fixed receiver. Motion effects need be considered only up to second-order for the first-order radar cross section and up to first-order for the second-order radar cross section. The latter is true because the energies of the motion-

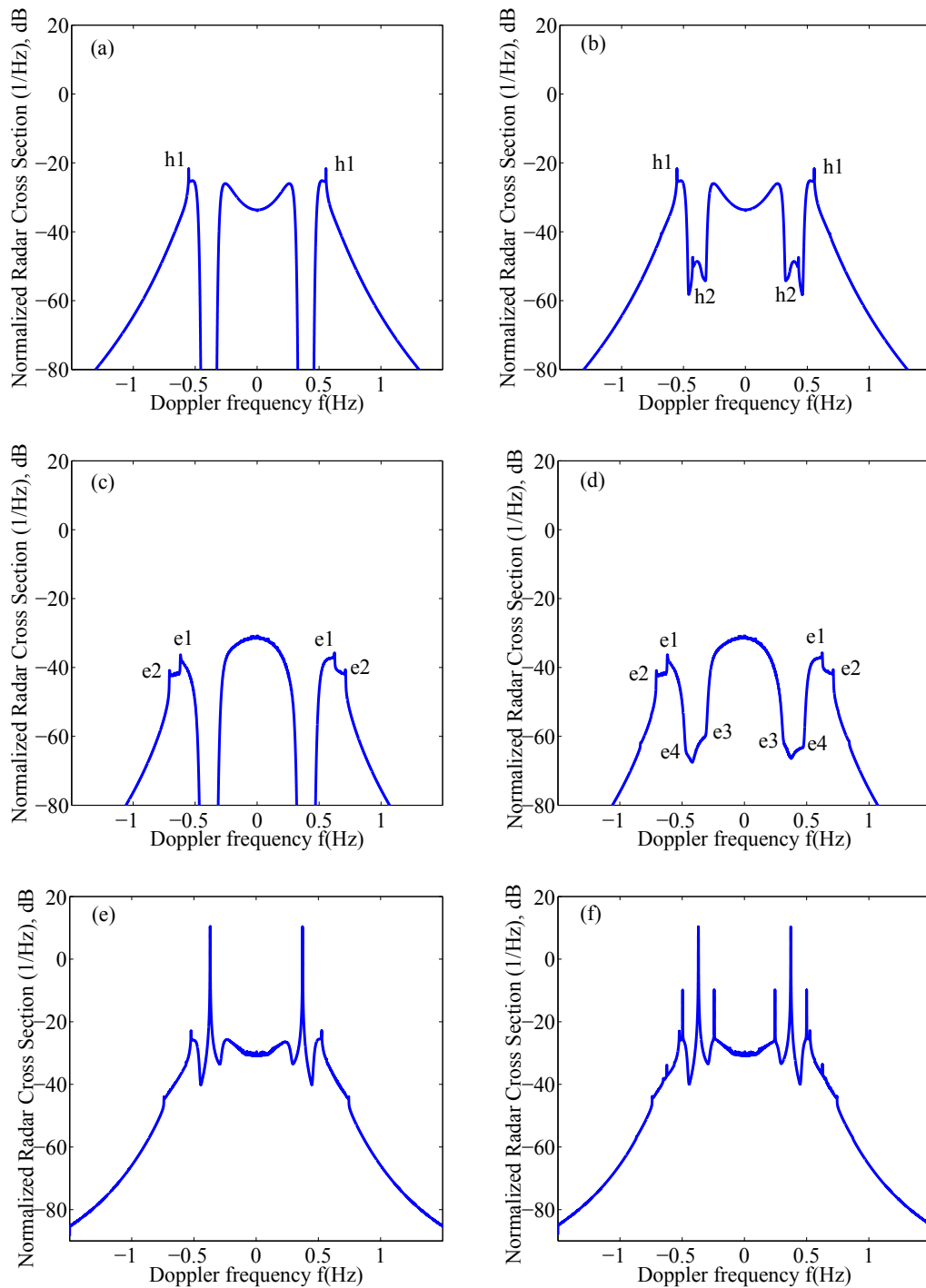


Fig. 2.4 (a) The second-order bistatic hydrodynamic contribution without antenna motion. (b) The second-order hydrodynamic contribution with antenna motion. (c) The second-order electromagnetic contribution without antenna motion. (d) The second-order electromagnetic contribution with antenna motion. (e) The total bistatic radar cross section without antenna motion. (f) The total bistatic radar cross section with antenna motion.

induced peaks in the second-order radar cross section are significantly lower than that of the first-order result. The case presented demonstrates that in general, the second-order hydrodynamic contribution is greater than that of the electromagnetic contribution.

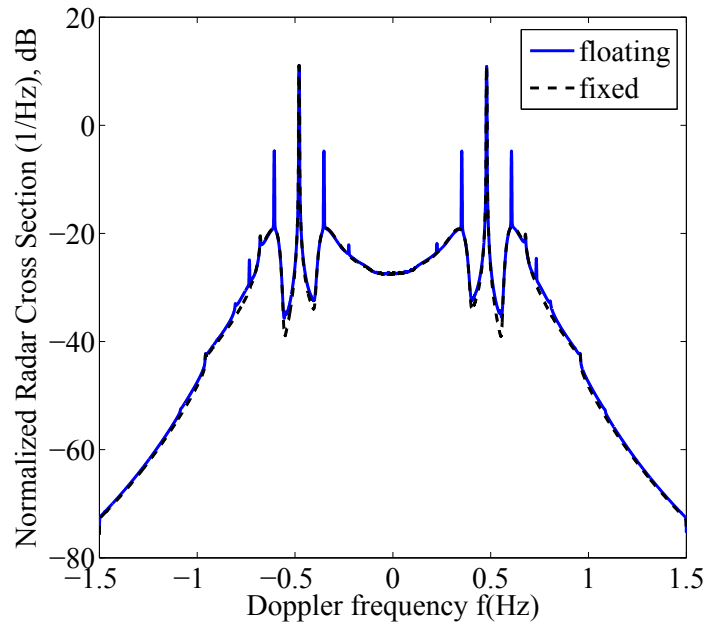


Fig. 2.5 Comparison of the total bistatic radar cross section for both transmitter and receiver fixed with that for a floating transmitter and a fixed receiver.

The difference between the bistatic and monostatic radar cross sections with antenna motion is depicted in Fig. 2.6. Maintaining the location of the transmitter and the wind direction fixed, a comparison is made by varying the antenna operating geometry (bistatic or monostatic). It may be observed that, for the bistatic case, the frequencies of the first-order and the second-order peaks are closer to zero Doppler frequency. This is also true for peaks induced by the platform motion. It may be observed that in the monostatic case, the peaks (including the Bragg peaks and the motion-induced peaks) in the negative Doppler frequency region have less energy, while the peaks in the positive Doppler frequency region have more energy than those of the bistatic case. This is because, for the example presented here, the angle between the wind direction with the look direction  $\theta_L$  in the monostatic case is larger than the angle between the wind direction with the ellipse normal  $\theta_N$  in the bistatic case.

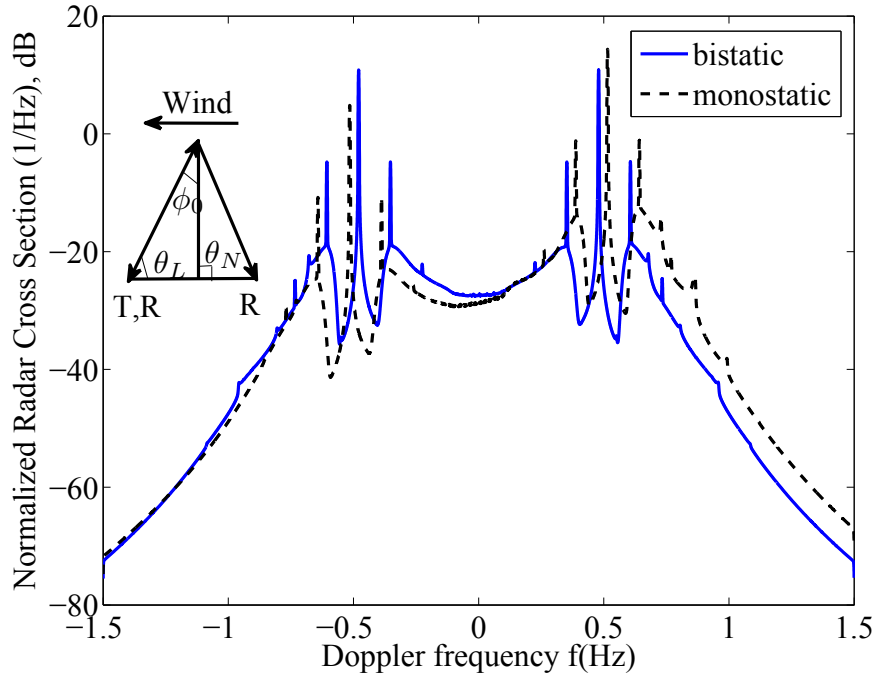


Fig. 2.6 Comparison of the radar cross sections with floating platform for the monostatic case and for the bistatic case with bistatic angle of  $30^\circ$ . Wind direction is  $180^\circ$ , ellipse normal  $\theta_N = 90^\circ$  for bistatic geometry and look direction  $\theta_L = 60^\circ$  for monostatic geometry.

Fig. 2.7 illustrates the effect of wind speed on the bistatic radar cross section with antenna motion. From Fig. 2.7, it can be seen that the motion-induced peaks are highly sensitive to the wind speed. The peaks caused by antenna motion increase in amplitude and decrease in Doppler frequency as the wind speed increases. This is because, as mentioned before, the sway amplitude and frequency are determined by the wind speed. When the wind speed increases, the sway amplitude will increase and the sway frequency will decrease. At low wind speeds, the effect of the antenna-motion-induced peaks on the Doppler spectrum is not significant. It should be noted that magnitude differences between the Bragg peaks and the motion-induced peaks for the bistatic case presented here are larger than in the monostatic results appearing in [17], even when the wind speeds are identical. This is due to the fact that the bistatic geometry affects the values of  $K$  and  $\phi_0$ , and the fixed receiver introduces a factor of “1/2” in the argument of the

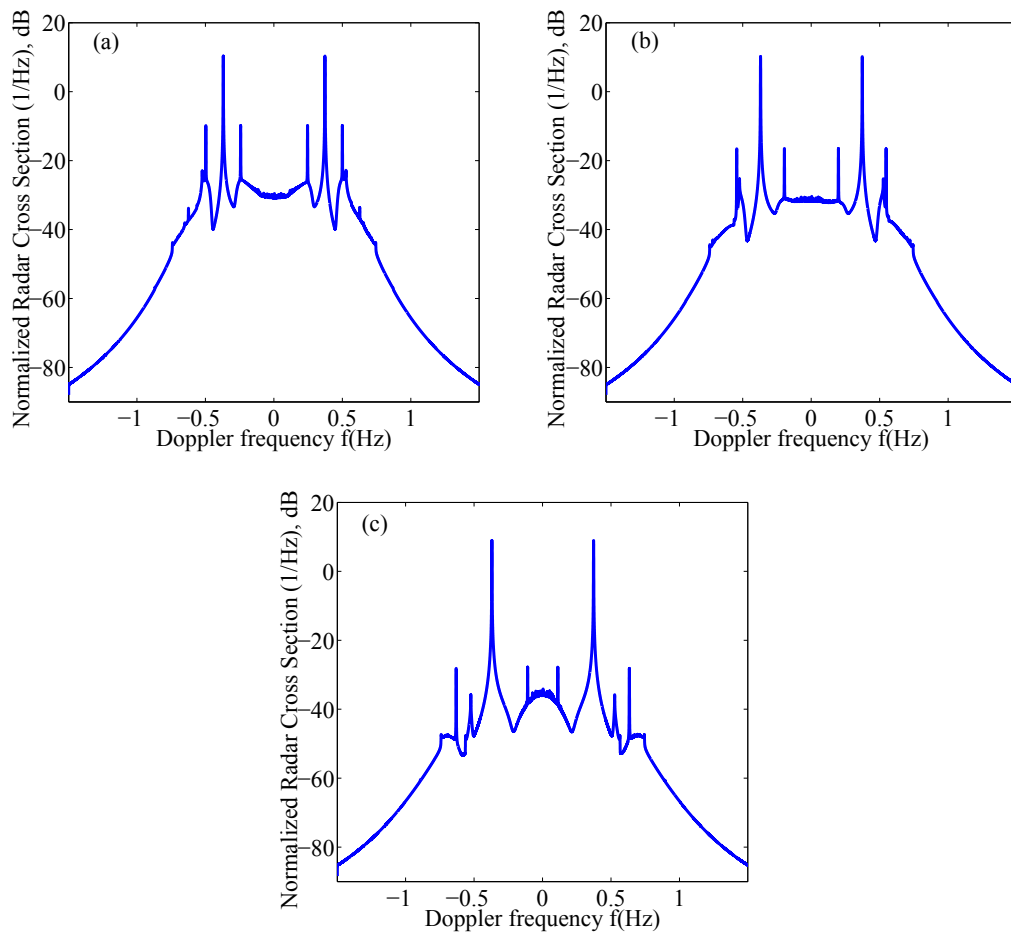


Fig. 2.7 The effect of wind speed on bistatic radar cross section with floating transmitter and fixed receiver. The wind speed is (a) 20 knots, (b) 15 knots, (c) 10 knots.

Bessel functions of the models. By comparison, the Bragg peaks, the second-order hydrodynamic peaks and electromagnetic peaks are not significantly affected by wind speed provide that the sea is fully developed at the radar operating frequency.

The effect of wind direction on bistatic radar cross section with antenna motion is shown in Fig. 2.8. From this figure, it is clearly seen that all the peaks including the Bragg peaks, the second-order hydrodynamic peaks, electromagnetic peaks and the motion-induced peaks show the same reaction to the change in the wind direction. As is to be expected, the ratio of the intensities of the positive and negative peaks is highly sensitive to wind direction. If the wind is perpendicular to the ellipse normal, the positive and negative peaks will carry the same amount of energy, and the spectrum will be

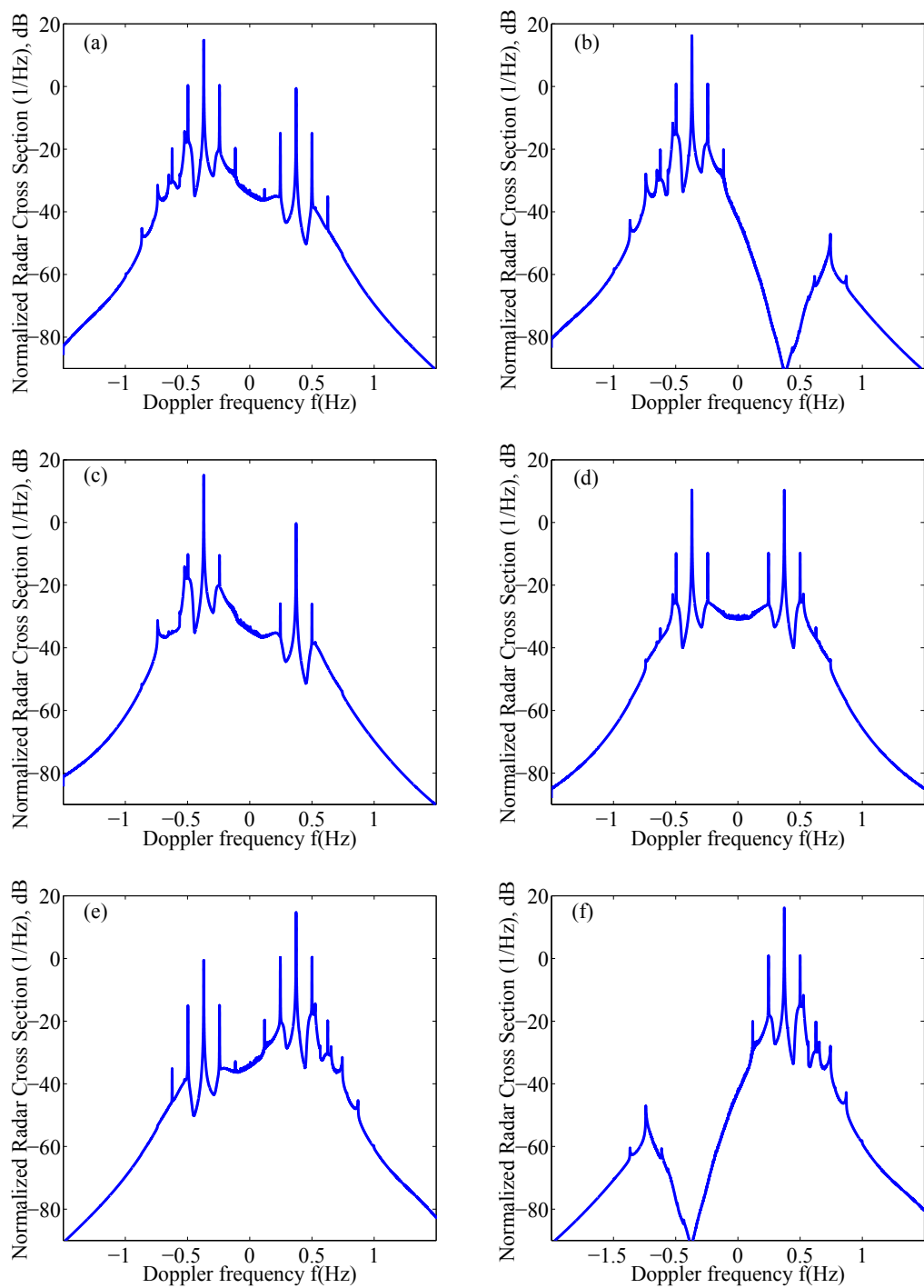


Fig. 2.8 The effect of wind direction on bistatic radar cross section with floating transmitter and fixed receiver. The wind direction is (a)  $45^\circ$ , (b)  $90^\circ$ , (c)  $135^\circ$ , (d)  $180^\circ$ , (e)  $225^\circ$ , (f)  $270^\circ$  with respect to the positive  $x$  axis. The ellipse normal is  $90^\circ$  with respect to the positive  $x$  axis.

symmetrical. When the wind direction is parallel/anti-parallel to the ellipse normal (i.e. the angle between these two directions is  $0^\circ/180^\circ$ ), the negative/positive Bragg peaks will reach their maximum. It is worth noting that, for monostatic operation from a floating platform, when the wind direction is perpendicular to the radar look direction, the sway motion does not produce additional peaks, while for the bistatic operation, this is not the case.

Fig. 2.9 illustrates how radar frequency affects the bistatic radar cross sections associated with antenna motion. From Fig. 2.9, it may be observed that the energy of the antenna-motion-induced peaks decreases as the radar operating frequency drops. When the radar frequency is lower than 7 MHz, the effect of these peaks caused by antenna motion under moderate sea state may be ignored due to its insignificant influence [17].

## 2.6 Chapter Summary

The development of the first- and second-order bistatic radar patch scatter cross sections of the ocean surface have been presented for the case of a fixed receiver and a transmitter mounted on a floating platform. Beginning with the bistatic electric fields for scattering from a time-invariant rough ocean surface derived in [17] and [18], a small displacement has been added into the source term. Then, the electric field equations are transformed to the time domain and adjusted to incorporate a time-varying ocean surface. Finally, the radar cross sections are deduced following procedures similar to those found in [17], [18]. The developed models are verified by imposing the appropriate conditions on the new models, to reduce them to the stationary bistatic models in [51] or the monostatic models with antenna motion in [17], [18]. Based on the new models, the effect of antenna motion on the radar cross section is simulated and discussed under different wind speeds, wind directions and radar frequencies. The simulation shows that the platform motion introduces additional peaks that contaminate the Doppler spectrum. This is consistent with the experimental results in [9]. The phenomenon will potentially result in the

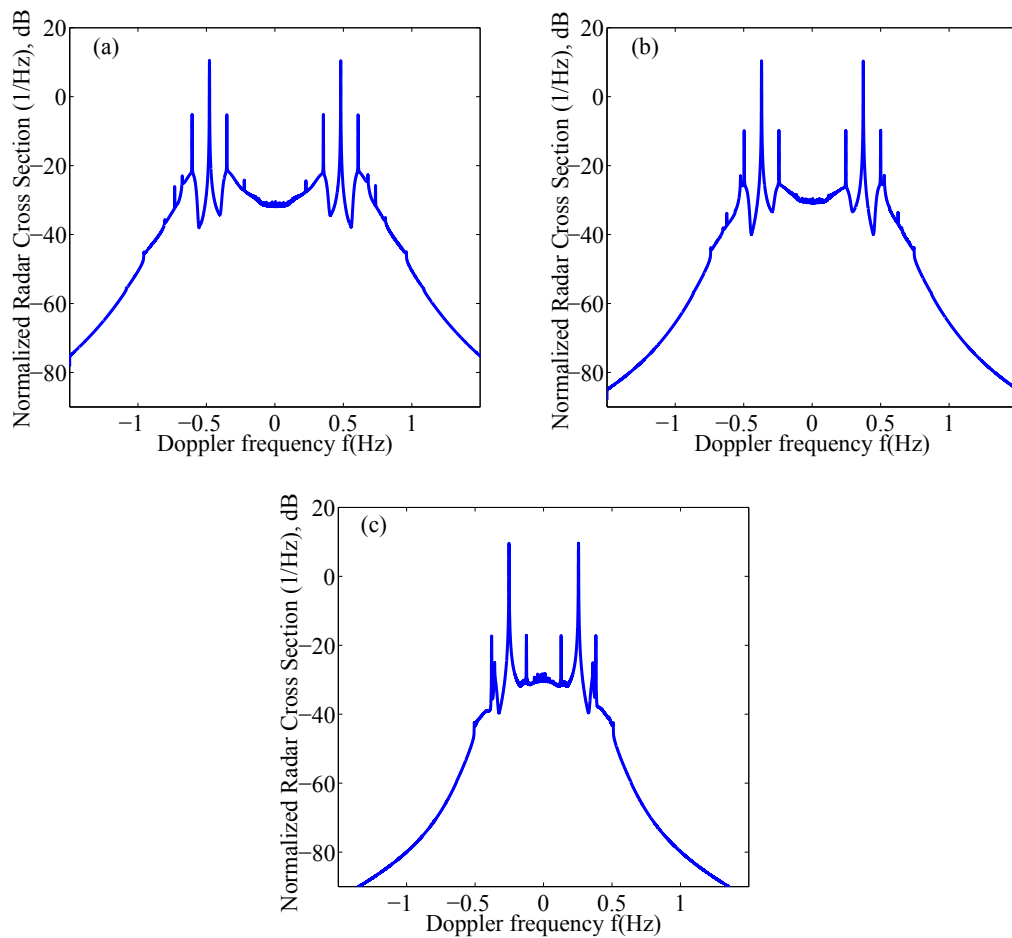


Fig. 2.9 The effect of radar frequency on bistatic radar cross section with floating transmitter and fixed receiver. The radar frequency is (a) 25 MHz, (b) 15 MHz, (c) 7 MHz.

overestimation of wave height determined by the inversion of such contaminated second-order echo. It is found that sway-motion-induced peaks appear symmetrically with respect to the zero Doppler frequency in the Doppler spectra and are more significant in the first-order radar cross section than in the second-order case. Simulations are also made to compare the bistatic model with the monostatic case. It is clear that these motion-induced peaks are closer to zero Doppler frequency in the bistatic case than in the monostatic case.

In this chapter, a simple sinusoidal model is used to describe the antenna motion as presented in [17], [18]. This simple model serves to establish the proof of concept. Of course, incorporating a model that better fits a particular experiment is worthy of con-

sideration. However, the conclusion of this chapter is that this would not fundamentally alter the analysis. Such models are discussed in Chapter 4 of this thesis.

## **Chapter 3**

# **Bistatic Radar Cross Section for an FMCW Source with an Antenna on a Floating Platform**

### **3.1 Introduction**

All of the models mentioned previously were developed specifically for a simple pulsed radar that are generally used in monostatic configurations where the receiver must be protected from the transmitter. However, there are inherent disadvantages to using pulsed radar systems. For example, the detectable range capability is determined by the average transmitted power. In a pulsed radar system, both the range resolution and the average transmitted power are dependent on the pulse width. Narrower pulses, bringing better range resolution, require large peak powers to be useful at long range. Compared to this, FMCW radar systems are able to achieve satisfactory range resolution and long range with moderate power due to a 100% duty cycle provide that the receiver and transmitter system are sufficiently separated. FMCW system are generally preferred if the transmitter and receiver systems can be separated such that there is sufficient attenuation of the direct

waveform. Thus, in recent years, FMCW radars have been widely used in ocean remote sensing applications.

A good summary of the digital processing of an FMCW signal for radar systems has been reported by Barrick [58]. Then, techniques for range and unambiguous velocity measurement for an FMCW radar were outlined in [59]. More recently, Walsh *et al.* [60] developed the first- and second-order monostatic radar ocean surface cross sections for an FMCW waveform.

In this chapter, the first- and second-order bistatic radar ocean surface cross sections for an antenna on a floating platform, and incorporating an FMCW source, are presented. Through these newly-developed RCS models, the differences in RCS for different sources are compared and the platform motion effect on the Doppler spectra for an FMCW source is illustrated. Based on previous work, the derivation begins with the general bistatic electric field in the frequency domain for the case of a floating antenna. Demodulation and range transformation are used to obtain the range information, distinguishing the process from that used for a pulsed radar. After Fourier transforming the auto-correlation and comparing the result with the radar range equation, the radar cross sections are derived. In Section 3.2, the derivation process for the first- and second-order received electric field is reviewed. Then, a method similar to that in [51] is used to obtain the first- and second-order radar cross sections in Section 3.3. Section 3.4 contains model simulations and comparisons with the pulsed waveform. Section 3.5 provides conclusions.

## **3.2 Radar Received Field Equations – FMCW source**

### **3.2.1 General First- and Second-Order Electric Field Equation**

In Chapter 2, it was noted that, without specifying the dipole source, (2.1) and (2.42) are, respectively, the first- and second-order bistatic scattered fields for an antenna on a

floating platform. Based on these two scattered field expressions, the derivation of the radar cross section models for an FMCW source is carried out below.

### 3.2.2 Applications to an FMCW Radar

Following a similar analysis as in [50] and [51], (2.1) may be inversely Fourier transformed to give the received electric field in the time domain as

$$\begin{aligned} \mathcal{F}^{-1}[(E_n)_1](t) &= \frac{1}{(2\pi)^{3/2}} \mathcal{F}^{-1}\left[-j \frac{\eta_0 \Delta l}{c^2} \omega^2 I(\omega)\right] \\ & \quad * \mathcal{F}^{-1}\left\{ \sum_{\vec{K}} P_{\vec{K}} \sqrt{K} e^{j \frac{\rho K}{2} \cos(\theta_K - \theta)} \int_{\rho/2}^{\infty} \frac{F(\rho_1) F(\rho_2)}{\sqrt{\rho_s [\rho_s^2 - (\rho/2)^2]}} e^{-j \frac{\pi}{4}} \right. \\ & \quad \left. \cdot \sqrt{\cos \phi} e^{jk \delta \rho_0 [\cos \phi \cos(\theta_K - \theta_0) + \sin \phi \sin(\theta_K - \theta_0)]} e^{j \rho_s [K \cos \phi - 2k]} d\rho_s \right\}. \end{aligned} \quad (3.1)$$

The current waveform of an FMCW radar may be written as [58], [60]

$$i(t) = I_0 e^{j(\omega_0 t + \alpha \pi t^2)} \left\{ h\left[t + \frac{T_r}{2}\right] - h\left[t - \frac{T_r}{2}\right] \right\} \quad (3.2)$$

where  $I_0$  is the peak current and  $\omega_0 = 2\pi f_0$  is the center radian frequency of the sweep waveform.  $T_r$  represents the sweep interval and the sweep rate may be expressed as  $\alpha = B/T_r$  where  $B$  is the sweep bandwidth.

It is known from [60] that for an FMCW waveform,

$$\mathcal{F}^{-1}\left[-j \frac{\eta_0 \Delta l}{c^2} \omega^2 I(\omega)\right] = -j I_0 \frac{\eta_0 \Delta l \omega_0^2}{c^2} e^{j(\omega_0 t + \alpha \pi t^2)} \left\{ h\left[t + \frac{T_r}{2}\right] - h\left[t - \frac{T_r}{2}\right] \right\}. \quad (3.3)$$

From this, by direct comparison with the corresponding first-order case for a pulsed dipole found in equation (2.2), the first-order time domain electric field for an FMCW

source may be written as

$$\begin{aligned}
(E_n)_{1bfff}(t_r) &= \frac{-jI_0\eta_0\Delta lk_0^2}{(2\pi)^{3/2}} \sum_{\vec{K}} P_{\vec{K}} \sqrt{K} e^{j\frac{\rho K}{2} \cos(\theta_K - \theta)} e^{-j\frac{\pi}{4}} \\
&\cdot \int_{\rho/2}^{\infty} \frac{F(\rho_1, \omega_0) F(\rho_2, \omega_0)}{\sqrt{\rho_s [\rho_s^2 - (\rho/2)^2]}} \sqrt{\cos \phi} e^{j\rho_s K \cos \phi} e^{j(\omega_0 t_r + \alpha \pi t_r^2)} \\
&\cdot e^{-jk_0(2\rho_s - \delta\rho_{s0})} e^{-j\frac{2\pi\alpha(2\rho_s - \delta\rho_{s0})}{c} t_r} e^{j\frac{\pi\alpha(2\rho_s - \delta\rho_{s0})^2}{c^2}} \\
&\cdot \left\{ h\left[t_r + \frac{T_r}{2} - \frac{2\rho_s - \delta\rho_{s0}}{c}\right] - h\left[t_r - \frac{T_r}{2} - \frac{2\rho_s - \delta\rho_{s0}}{c}\right] \right\} d\rho_s
\end{aligned} \tag{3.4}$$

where  $t$  is renamed as  $t_r$  to indicate that the time is within a sweep repetition interval  $(\frac{2\rho_s - \delta\rho_{s0}}{c} - \frac{T_r}{2}, \frac{2\rho_s - \delta\rho_{s0}}{c} + \frac{T_r}{2})$ . As stated in [58] and [60], the frequency difference between the transmitted waveform and the received waveform may be Fourier transformed within this interval to obtain the range information. This is the so-called ‘‘range transform’’. Because the received signals in the given time interval reflect the information for an extremely large region of the ocean surface, here range transformation is taken to specify a patch of ocean surface to analyse. The frequency difference of waveforms may be obtained by the demodulation process, in which the transmitted signals and the received signals are mixed and then lowpass filtered.

After the demodulation preprocess, the exponential factor  $e^{j(\omega_0 t_r + \alpha \pi t_r^2)}$  in (3.4) will be eliminated. Then, Fourier transforming with respect to  $t_r$  gives

$$\begin{aligned}
(E_n)_{1bfff}(\omega_r) &= \frac{-jI_0\eta_0\Delta lk_0^2 T_r}{(2\pi)^{3/2}} \sum_{\vec{K}} P_{\vec{K}} \sqrt{K} e^{j\frac{\rho K}{2} \cos(\theta_K - \theta)} e^{-j\frac{\pi}{4}} \\
&\cdot \int_{\rho/2}^{\infty} \frac{F(\rho_1, \omega_0) F(\rho_2, \omega_0)}{\sqrt{\rho_s [\rho_s^2 - (\rho/2)^2]}} \sqrt{\cos \phi} e^{j\rho_s K \cos \phi} e^{-jk_0(2\rho_s - \delta\rho_{s0})} \\
&\cdot e^{j\omega_r(2\rho_s - \delta\rho_{s0})/c} e^{-j\frac{\pi\alpha(2\rho_s - \delta\rho_{s0})^2}{c^2}} \text{Sa}\left[\frac{T_r}{2}\left(\omega_r - \frac{2\pi\alpha(2\rho_s - \delta\rho_{s0})}{c}\right)\right] d\rho_s
\end{aligned} \tag{3.5}$$

where  $\omega_r$  is the transform variable in the frequency domain. Similarly, using the definition  $\rho'_s = \rho_s - \delta\rho_{s0}/2$  and changing the integration variable from  $\rho_s$  to  $\rho'_s$  and ignoring the

$\delta\rho_{s0}/2$  factor in the magnitude terms give

$$\begin{aligned}
(E_n)_{1bfff}(\omega_r) &= \frac{-jI_0\eta_0\Delta lk_0^2 T_r}{(2\pi)^{3/2}} \sum_{\bar{K}} P_{\bar{K}} \sqrt{K} e^{j\frac{\rho K}{2} \cos(\theta_K - \theta)} e^{-j\frac{\pi}{4}} \\
&\cdot \int_{\rho/2}^{\infty} \frac{F(\rho_1, \omega_0) F(\rho_2, \omega_0)}{\sqrt{\rho_s [\rho_s^2 - (\rho/2)^2]}} \sqrt{\cos \phi} e^{j(K \cos \phi - 2k_0 + 2\omega_r/c)\rho'_s} e^{-j\frac{4\pi\alpha(\rho'_s)^2}{c^2}} \quad (3.6) \\
&\cdot e^{j\delta\rho_{s0}K \cos \phi/2} \text{Sa}\left[\frac{T_r}{2}\left(\omega_r - \frac{4\pi\alpha}{c}\rho'_s\right)\right] d\rho'_s.
\end{aligned}$$

Since the maximum of the sampling function  $Sa(x)$  occurs at  $x = 0$ , a representative range  $\rho_r$  may be defined as

$$\rho_r = \frac{c\omega_r}{4\pi\alpha}. \quad (3.7)$$

Based on the representative range, defining the corresponding range variable

$$\rho''_s = \rho'_s - \rho_r \quad (3.8)$$

and changing the integration variable from  $\rho'_s$  to  $\rho''_s$ , (3.6) becomes

$$\begin{aligned}
(E_n)_{1bfff}(\omega_r) &= \frac{-jI_0\eta_0\Delta lk_0^2 T_r}{(2\pi)^{3/2}} \sum_{\bar{K}} P_{\bar{K}} \sqrt{K} e^{j\frac{\rho K}{2} \cos(\theta_K - \theta)} e^{-j\frac{\pi}{4}} \\
&\cdot \int_{\rho''_{s\min}}^{\rho''_{s\max}} \frac{F(\rho_1, \omega_0) F(\rho_2, \omega_0)}{\sqrt{\rho_s [\rho_s^2 - (\rho/2)^2]}} \sqrt{\cos \phi} e^{j(-2k_0 + k_r)\rho_r} e^{j(-2k_0)\rho''_s} \quad (3.9) \\
&\cdot e^{j\rho_s K \cos \phi} e^{-j(k_r/\rho_r)(\rho''_s)^2} \text{Sa}[k_B \rho''_s] d\rho''_s
\end{aligned}$$

where  $k_B = \frac{2\pi B}{c}$  and  $k_r = \frac{\omega_r}{c}$ . A process similar to that in [50] is used to simplify the terms in the integral. Then, (3.9) reduces to

$$\begin{aligned}
(E_n)_{1bfff}(\omega_r) &= \frac{-jI_0\eta_0\Delta lk_0^2 T_r}{(2\pi)^{3/2}} \sum_{\bar{K}} P_{\bar{K}} \sqrt{K} e^{j\frac{\rho K}{2} \cos(\theta_K - \theta)} e^{-j\frac{\pi}{4}} \sqrt{\cos \phi_0} \\
&\cdot \frac{F(\rho_{01}, \omega_0) F(\rho_{02}, \omega_0)}{\sqrt{\rho_r [\rho_r^2 - (\rho/2)^2]}} e^{j\frac{\delta\rho_{s0}}{2} \frac{K}{\cos \phi_0}} e^{j(K \cos \phi_0 - 2k_0 + k_r)\rho_r} \quad (3.10) \\
&\cdot \int_{\rho''_{s\min}}^{\rho''_{s\max}} e^{j(\frac{K}{\cos \phi_0} - 2k_0)\rho''_s} e^{-j(k_r/\rho_r)(\rho''_s)^2} \text{Sa}[k_B \rho''_s] d\rho''_s.
\end{aligned}$$

By directly comparing (3.10) with (24) in [60], the first-order bistatic received electric field for an FMCW waveform with an antenna on a floating platform may be expressed as [61]

$$\begin{aligned}
(E_n)_{1bff}(\omega_r) &= \frac{-jI_0\eta_0\Delta lk_0^2}{(2\pi)^{3/2}} \sum_{\vec{K}} P_{\vec{K}} \sqrt{K} e^{j\frac{\rho K}{2} \cos(\theta_K - \theta)} e^{-j\frac{\pi}{4}} \\
&\cdot \sqrt{\cos\phi_0} e^{j(K\cos\phi_0 - 2k_0 + k_r)\rho_r} \frac{F(\rho_{01}, \omega_0) F(\rho_{02}, \omega_0)}{\sqrt{\rho_r[\rho_r^2 - (\rho/2)^2]}} \\
&\cdot e^{j\frac{\delta\rho_{s0}}{2} \frac{K}{\cos\phi_0}} (T_r\Delta\rho) \text{Sm}(K, \cos\phi_0, k_B, \Delta r).
\end{aligned} \tag{3.11}$$

$\pm\Delta r$  are the symmetrical limits of the integral in (3.10), where a sampling function dominates this integral. If only the values of  $\rho_s''$  within the main lobe of the sampling function are considered in the integral, i.e.,  $-\frac{\pi}{2} < k_B\rho_s'' < \frac{\pi}{2}$ , it can be deduced as in [60] that  $\Delta r = \frac{\Delta\rho}{2} = \frac{c}{4B}$ . Also, as in [60],

$$\text{Sm}(K, \cos\phi_0, k_B, \Delta r) = \frac{1}{\pi} \left\{ \text{Si} \left[ \left( \frac{K}{\cos\phi_0} - 2k_0 + k_B \right) \Delta r \right] - \text{Si} \left[ \left( \frac{K}{\cos\phi_0} - 2k_0 - k_B \right) \Delta r \right] \right\} \tag{3.12}$$

where  $\text{Si}(x) = \int_0^x \frac{\sin(t)}{t} dt$ .

Following a similar procedure to the first-order case, the second-order bistatic received electric field with a transmitter on a floating platform for an FMCW waveform may be written as

$$\begin{aligned}
(E_n)_{2bff}(\omega_r) &= \frac{-jI_0\eta_0\Delta lk_0^2}{(2\pi)^{3/2}} \sum_{\vec{K}_1} \sum_{\vec{K}_2} P_{\vec{K}_1} P_{\vec{K}_2} \sqrt{K} e^{-j\frac{\pi}{4}} e^{j\frac{\rho K}{2} \cos(\theta_K - \theta)} \sqrt{\cos\phi_0} \\
&\cdot e^{j(K\cos\phi_0 - 2k_0 + k_r)\rho_r} \frac{SE\Gamma_P F(\rho_{02}, \omega_0) F(\rho_{020}, \omega_0)}{\sqrt{\rho_r[\rho_r^2 - (\rho/2)^2]}} e^{j\frac{\delta\rho_{s0}}{2} \frac{K}{\cos\phi_0}} \\
&\cdot (T_r\Delta\rho) \text{Sm}(K, \cos\phi_0, k_B, \Delta r).
\end{aligned} \tag{3.13}$$

### 3.3 Radar Cross Sections for an FMCW Source

#### 3.3.1 First-Order Radar Cross Section

In developing the ocean radar cross section, a time-varying ocean surface (1.5) is used to replace the time-invariant case (1.3). This gives the time-varying received electric field corresponding to (3.11) as

$$\begin{aligned}
 (E_n)_{1bff}(\omega_r, t) &= \frac{-jI_0\eta_0\Delta l k_0^2}{(2\pi)^{3/2}} \sum_{\vec{K}, \omega} P_{\vec{K}, \omega} \sqrt{K} e^{j\frac{\rho K}{2} \cos(\theta_K - \theta)} e^{j(K \cos \phi_0 - 2k_0 + k_r)\rho_r} \\
 &\cdot e^{-j\frac{\pi}{4}} \sqrt{\cos \phi_0} e^{j\omega t} \frac{F(\rho_{01}, \omega_0) F(\rho_{02}, \omega_0)}{\sqrt{\rho_r[\rho_r^2 - (\rho/2)^2]}} \\
 &\cdot e^{j\frac{\delta\rho_{s0}}{2} \frac{K}{\cos \phi_0}} (T_r \Delta \rho) \text{Sm}(K, \cos \phi_0, k_B, \Delta r).
 \end{aligned} \tag{3.14}$$

A technique similar to that in [50] and [60] is used to obtain the radar cross section from the received electric field equation. After Fourier transforming the auto-correlation and comparing directly with the radar range equation, the radar cross section,  $\sigma_{1bff}(\omega_d)$ , may be written as [61]

$$\begin{aligned}
 \sigma_{1bff}(\omega_d) &= 2^3 \pi k_0^2 \Delta \rho \sum_{m=\pm 1} \int_K S_1(m\vec{K}) K^2 \cos \phi_0 \text{Sm}^2(K, \cos \phi_0, k_B, \Delta r) \\
 &\cdot \{J_0^2[\frac{aK}{2} |\cos(\theta_K - \theta_{K_p}) + \tan \phi_0 \sin(\theta_K - \theta_{K_p})|] \cdot \delta(\omega_d + m\sqrt{gK}) \\
 &+ \sum_{n=1}^{\infty} J_n^2[\frac{aK}{2} |\cos(\theta_K - \theta_{K_p}) + \tan \phi_0 \sin(\theta_K - \theta_{K_p})|] \\
 &\cdot [\delta(\omega_d + m\sqrt{gK} - n\omega_p) + \delta(\omega_d + m\sqrt{gK} + n\omega_p)]\} dK
 \end{aligned} \tag{3.15}$$

For simulation purposes (see Section 3.4) and in keeping with [17] and [50], it will be assumed that the antenna motion is caused by the dominant ocean waves.

### 3.3.2 Second-Order Radar Cross Section

From Chapter 1, it is known that the second-order radar cross section contains two portions: an hydrodynamic contribution and an electromagnetic contribution. Using the Fourier coefficient for the second-order ocean waves  $\sum_{\vec{K}_1} \sum_{\vec{K}_2} H\Gamma P_{\vec{K}_1} P_{\vec{K}_2}$  to replace the first-order case  $\sum_{\vec{K}} P_{\vec{K}}$  in (3.11), the hydrodynamic second-order electric field may be written as

$$\begin{aligned}
 (E_n)_{2bfff}(\omega_r) &= \frac{-jI_0\eta_0\Delta lk_0^2}{(2\pi)^{3/2}} \sum_{\vec{K}_1} \sum_{\vec{K}_2} P_{\vec{K}_1} P_{\vec{K}_2} \sqrt{K} e^{-j\frac{\pi}{4}} e^{j\frac{\rho K}{2} \cos(\theta_K - \theta)} \sqrt{\cos\phi_0} \\
 &\cdot e^{j(K\cos\phi_0 - 2k_0 + k_r)\rho_r} \frac{H\Gamma F(\rho_{01}, \omega_0) F(\rho_{02}, \omega_0)}{\sqrt{\rho_r[\rho_r^2 - (\rho/2)^2]}} e^{j\frac{\delta\rho_{s0}}{2} \frac{K}{\cos\phi_0}} \\
 &\cdot (T_r\Delta\rho) \text{Sm}(K, \cos\phi_0, k_B, \Delta r).
 \end{aligned} \tag{3.16}$$

Adding the electromagnetic contribution (3.13) and the hydrodynamic contribution (3.16) together and using the time-varying ocean wave surface (1.5) to replace the time-invariant case (1.3), the total second-order bistatic electric field for an FMCW source with an antenna on a floating platform may be expressed as

$$\begin{aligned}
 (E_n)_{2bfff}(\omega_r, t) &= \frac{-jI_0\eta_0\Delta lk_0^2}{(2\pi)^{3/2}} \sum_{\vec{K}_1, \omega_1} \sum_{\vec{K}_2, \omega_2} P_{\vec{K}_1, \omega_1} P_{\vec{K}_2, \omega_2} \Gamma_{P_b} \sqrt{K} e^{j\frac{\rho K}{2} \cos(\theta_K - \theta)} e^{-j\frac{\pi}{4}} \\
 &\cdot \sqrt{\cos\phi_0} e^{j(K\cos\phi_0 - 2k_0 + k_r)\rho_r} e^{j\omega t} \frac{F(\rho_{01}, \omega_0) F(\rho_{02}, \omega_0)}{\sqrt{\rho_r[\rho_r^2 - (\rho/2)^2]}} e^{j\frac{\delta\rho_{s0}}{2} \frac{K}{\cos\phi_0}} \\
 &\cdot (T_r\Delta\rho) \text{Sm}(K, \cos\phi_0, k_B, \Delta r).
 \end{aligned} \tag{3.17}$$

Following the same procedure as for the first-order case, based on the total second-order time-varying received electric field (3.17), the corresponding second-order radar

cross section,  $\sigma_{2bff}(\omega_d)$ , may be obtained as [61]

$$\begin{aligned}
\sigma_{2bff}(\omega_d) = & 2^3 \pi k_0^2 \Delta \rho \sum_{m_1=\pm 1} \sum_{m_2=\pm 1} \int_0^\infty \int_{-\pi}^\pi \int_0^\infty \\
& \cdot S_1(m_1 \vec{K}_1) S_1(m_2 \vec{K}_2) |\Gamma_{P_b}|^2 K^2 \cos \phi_0 K_1 S m^2(K, \cos \phi_0, k_B, \Delta r) \\
& \cdot \left\{ J_0^2 \left\{ \frac{aK}{2} \left| \cos(\theta_K - \theta_{K_p}) + \tan \phi_0 \sin(\theta_K - \theta_{K_p}) \right| \right\} \right. \\
& \cdot \delta(\omega_d + m_1 \sqrt{gK_1} + m_2 \sqrt{gK_2}) \\
& + \sum_{n=1}^\infty J_n^2 \left\{ \frac{aK}{2} \left| \cos(\theta_K - \theta_{K_p}) + \tan \phi_0 \sin(\theta_K - \theta_{K_p}) \right| \right\} \\
& \cdot [\delta(\omega_d + m_1 \sqrt{gK_1} + m_2 \sqrt{gK_2} - n\omega_p) \\
& \left. + \delta(\omega_d + m_1 \sqrt{gK_1} + m_2 \sqrt{gK_2} + n\omega_p) \right\} dK_1 d\theta_{\vec{K}_1} dK.
\end{aligned} \tag{3.18}$$

## 3.4 Simulation and Analysis

Based on a Pierson-Moskowitz (PM) ocean spectral model for a fully developed sea [57], the newly derived radar cross sections, accounting for antenna sway, can be simulated to illustrate the differences in the FMCW and pulsed waveform cases. The sweep bandwidth of the FMCW waveform is chosen as 50 kHz. The operating frequency, defined as the central frequency of the FMCW waveform, is taken to be 25 MHz. The bistatic angle is  $30^\circ$  and the wind speed is 20 knots. The scattering ellipse normal and the wind direction are  $90^\circ$  and  $180^\circ$ , respectively, as measured from the positive  $x$  axis (the line connecting the transmitter with the receiver). The sway amplitude and frequency depend on the wind velocity and are taken from Table 2.1. The sway direction is chosen to be the same as the wind direction.

### 3.4.1 First-Order Radar Cross Section

Fig. 3.1 shows a comparison of the first-order radar cross section for a pulsed source and that for an FMCW source. In order to keep the same bandwidth for both waveforms, for the FMCW waveform,  $\Delta r$  is chosen to be 1500 m, which equals half the width of

the scattering patch ( $\Delta\rho = 3000$  m) for the pulsed waveform. A Hamming window is used to smooth the curve and reduce the oscillations. From this figure, it can be observed that additional peaks caused by the antenna motion appear symmetrically in the Doppler spectrum with respect to the Bragg peaks. A detailed description of these motion-induced peaks has been provided in Chapter 2. It can also be seen that the magnitudes of the radar cross sections for the FMCW waveform are a little lower than those for the corresponding pulsed waveform. This may be caused by the value of  $\Delta r$ .  $\Delta r$  is the limit value of the integral, in which a sampling function is a dominant factor.  $\Delta r$  is usually taken to be  $\Delta r = \Delta\rho/2$ , which means only the contributions in the main lobe of the sampling function are considered and no interaction between the range bins is assumed in the ideal case.

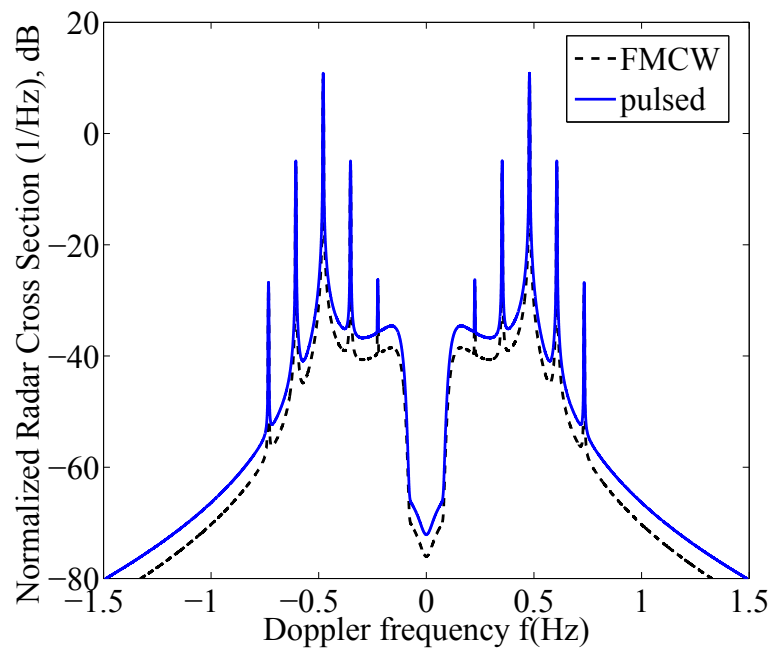


Fig. 3.1 Comparison of the first-order radar cross sections for the FMCW waveform with that for the pulsed waveform.

It is clear that the first-order radar cross section has a certain relationship with the integral limit  $\Delta r$ . In Section 3.2, it may be observed that there is no mathematical limit for the parameter  $\Delta r$ . By varying  $\Delta r$ , the effect on the radar cross section can be examined.

Keeping the value of  $\Delta\rho = 3000$  m,  $\Delta r = 0.5\Delta\rho$  and  $\Delta r = 10\Delta\rho$  are simulated in Figs. 3.2 (a) and (b), respectively. It should be mentioned that the Hamming window smoothing process is not used in Fig. 3.2 in order to clearly show the sidelobe levels of the first-order radar cross sections. The sidelobe structure appears in the radar Doppler spectra due to the sidelobes of the  $Sm$  function for the FMCW waveform. By comparing Figs. 3.2 (a) and (b), the magnitude of the sidelobes for FMCW source is found to decrease with increasing  $\Delta r$  and the main lobe level is a little raised with increasing  $\Delta r$  due to the properties of the  $Sm$  function. This seems to indicate an advantage of an FMCW system. When the value of  $\Delta r$  is taken to be larger than  $\Delta\rho/2$ , the interactions between the range bins (the contributions in the sidelobe of the sampling function) are considered and appear in the received electric field at a fixed distance. Increasing  $\Delta r$  means the received signal is scattered from a larger ocean surface region. When  $\Delta r$  approaches infinity, the radar cross section for the FMCW waveform becomes a rectangular function, whose width is determined by  $B/(2f_0\omega_B)$ . However, when the patch width  $\Delta\rho$  approaches infinity, the sampling functions in the first-order pulse radar ocean cross section reduce to delta functions.

By varying the radar bandwidth, and keeping the relationships  $\Delta\rho = c/2B$  and  $\Delta r = \Delta\rho/2$ , the effect of the bandwidth on the radar cross sections is illustrated in Fig. 3.3. From this figure, it can be seen that with increased bandwidth, the magnitudes of the Bragg peaks and the motion-induced peaks are found to be reduced, while the rest of the radar cross section increases. In addition, the width of the Bragg peaks and the motion-induced peaks is also broadened. Therefore, if a large radar bandwidth is used for ocean remote sensing, the Bragg peaks may be significantly contaminated by the motion-induced peaks.

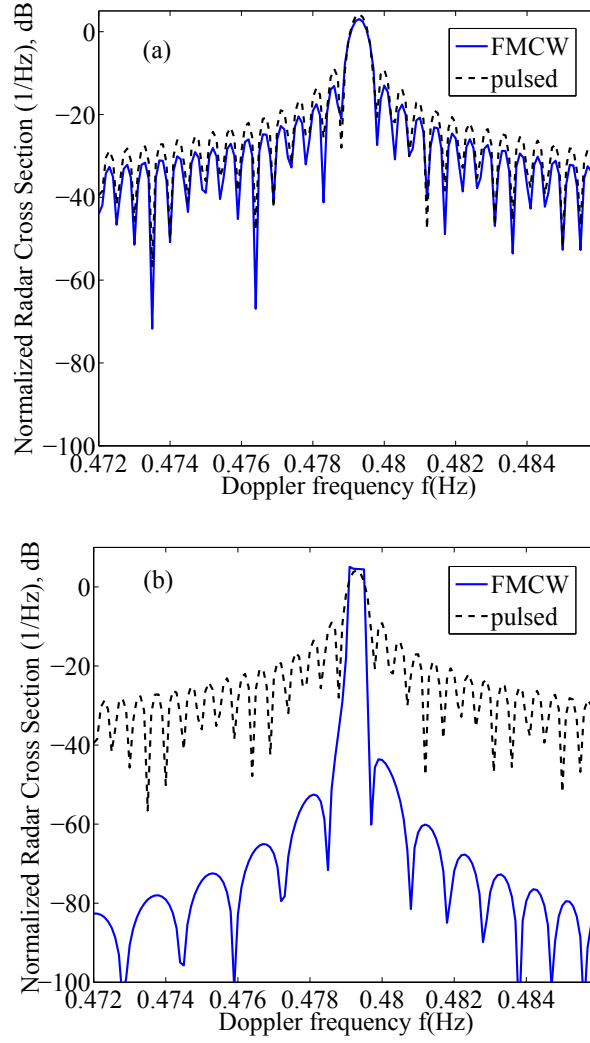


Fig. 3.2 Comparison of the sidelobe levels of the first-order radar cross sections for the pulsed and FMCW waveform. (a)  $\Delta r = 0.5\Delta\rho$  and (b)  $\Delta r = 10\Delta\rho$ .

### 3.4.2 Second-Order Radar Cross Section

A similar technique is used to simplify and simulate the second-order radar ocean cross section for the FMCW waveform as that for the pulsed waveform in [55] and [62]. For the case of large  $\Delta r$ , it can be shown that

$$\begin{aligned} \lim_{\Delta r \rightarrow \infty} [\Delta\rho S m^2(K, \cos\phi_0, k_B, \Delta r)] \\ \approx \Delta\rho \cos\phi_0 \{h[K - \cos\phi_0(2k_0 - k_B)] - h[K - \cos\phi_0(2k_0 + k_B)]\}. \end{aligned} \quad (3.19)$$

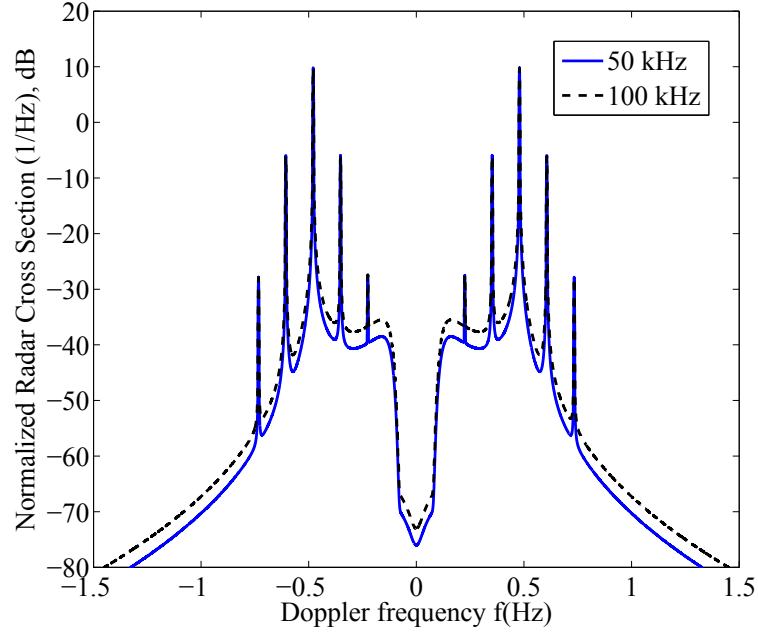


Fig. 3.3 The effect of the bandwidth on the first-order radar cross sections.

Assuming that the other terms in (3.18) are slowly varying within the interval

$$\cos \phi_0(2k_0 - k_B) < K < \cos \phi_0(2k_0 + k_B) \quad (3.20)$$

and carrying out the  $K$  integration, (3.18) reduces to

$$\begin{aligned} \sigma_{2bfff}(\omega_d) = & 2^6 \pi^2 k_0^4 \cos^4 \phi_0 \sum_{m_1=\pm 1} \sum_{m_2=\pm 1} \int_0^\infty \int_{-\pi}^\pi \\ & \cdot S_1(m_1 \vec{K}_1) S_1(m_2 \vec{K}_2) |\Gamma_{P_b}|^2 K_1 \\ & \cdot \left\{ J_0^2 \left\{ \frac{aK}{2} \left| \cos(\theta_K - \theta_{K_p}) + \tan \phi_0 \sin(\theta_K - \theta_{K_p}) \right| \right\} \right. \\ & \cdot \delta(\omega_d + m_1 \sqrt{gK_1} + m_2 \sqrt{gK_2}) \\ & + \sum_{n=1}^\infty J_n^2 \left\{ \frac{aK}{2} \left| \cos(\theta_K - \theta_{K_p}) + \tan \phi_0 \sin(\theta_K - \theta_{K_p}) \right| \right\} \\ & \cdot [\delta(\omega_d + m_1 \sqrt{gK_1} + m_2 \sqrt{gK_2} - n\omega_p) \\ & \left. + \delta(\omega_d + m_1 \sqrt{gK_1} + m_2 \sqrt{gK_2} + n\omega_p)] \right\} d\theta_{\vec{K}_1} dK_1. \end{aligned} \quad (3.21)$$

Equation (3.21) is the same as the corresponding model for the pulsed waveform when the scattering patch  $\Delta\rho$  approaches infinity. Therefore, the second-order cross section model for the FMCW waveform shows the same features in the Doppler spectra as the model for the pulsed waveform in [55], for a given sea state, radar operating parameters and platform motion. An example of the second-order bistatic radar cross section with a transmitter on a floating platform and a fixed receiver is shown in Fig. 3.4, for a scattering patch assumed to be infinite in extent. Details of the second-order radar cross section are illustrated in Fig. 2.4 previously presented in Section 2.5.

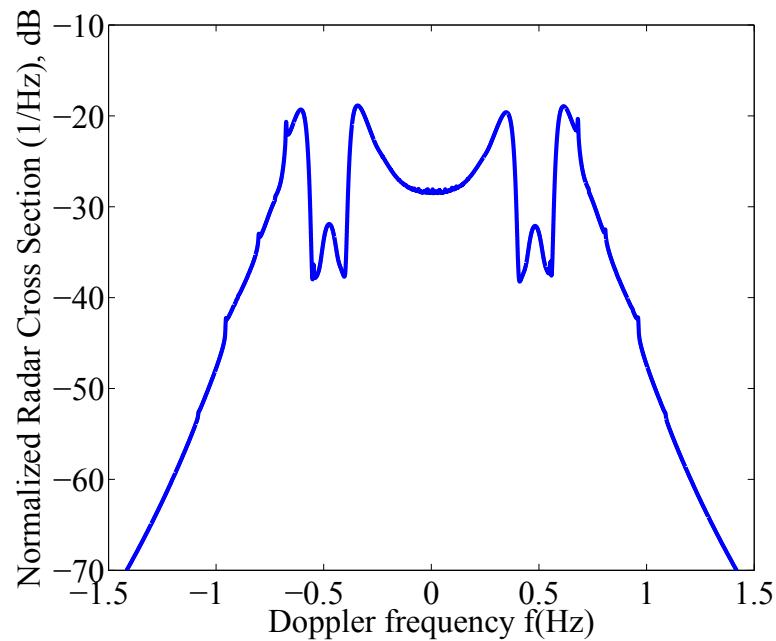


Fig. 3.4 Second-order bistatic radar cross section with a transmitter on a floating platform.

### 3.5 Chapter Summary

The first- and second-order bistatic radar ocean cross sections for an antenna on a floating platform have been presented for the case of an FMCW waveform. The derivations of the first- and second-order models begin with the bistatically-received electric field equations derived in [50] and [55]. Subsequently, the derivation is carried out for an FMCW radar,

which is different from [50] and [55] where a pulsed radar is considered. In particular, the distinguishing feature in the RCS derivation process is that demodulation and range transformation must be used to obtain the range information. Based on the new models, simulations are made to compare the radar cross sections for the FMCW waveform with those for the pulsed waveform. The effect of the platform motion on the Doppler spectra for an FMCW waveform is observed to be similar to that for a pulsed waveform. It is found that the first-order radar cross section for the FMCW waveform is a little lower than that for a pulsed source with the same simulation parameters. With increased radar operating bandwidth, the magnitude and width of Bragg peaks and motion-induced peaks are found to be reduced and broadened, respectively. For an FMCW waveform, there is no definite mathematical limit for a patch width, which is different from that for a pulsed waveform. Therefore, the magnitude of the range bin is varied to examine the effect on the radar cross section. The sidelobe level is found to be reduced with increasing magnitude of the range bin. When the range bin approaches infinity, the first-order radar cross section for an FMCW waveform approaches a rectangular function and the second-order radar cross section model for the FMCW waveform is reduced to that of the pulsed waveform.

# **Chapter 4**

## **Generalized Radar Cross Section**

### **Models with a More Realistic Platform**

#### **Motion Model**

##### **4.1 Introduction**

The studies conducted in Chapters 2 and 3 simplified the platform motion to a sinusoidal model with a single frequency. This is potentially problematic as the actual platform motion is unlikely to be perfectly sinusoidal. Thus, based on the work for the monostatic case with an antenna on a floating platform in [17] and [18], newly derived first- and second-order HFSWR ocean surface cross sections incorporating a more realistic platform motion model are presented in this chapter. In Section 4.2, a floating platform motion model is proposed. Then, a method similar to that described in [17] and [18] is used to obtain the new first- and second-order monostatic radar cross sections (Section 4.3) and bistatic radar cross sections (Section 4.4). The platform motion model is then extended to the case of multiple frequencies and a single motion direction as well as for surge and sway directions, and the corresponding radar cross section models are developed in Section 4.5. Section 4.6 contains model simulations and discussions on how

the new platform motion affects the radar cross sections. Finally, Section 4.7 presents conclusions and suggestions for future research.

## **4.2 A More Realistic Platform Motion Model**

If an HFSWR system is installed on a floating platform with a mooring system, such as an oil exploration platform, motion effects cannot be ignored in interpreting the radar cross sections and extracting wave information [9]. A large and heavy platform has the advantage of weak pitch and roll movements [32]. For example, for the large moored platform considered in [9], the angles of the pitch and roll were less than  $5^\circ$ . Unlike [39] and [42], the receiving antenna array is installed onshore in this study. Thus, the radiation pattern distortion caused by the platform motion in the vertical plane is not addressed. Because the platform motions in the vertical plane do not cause the Doppler shift. Therefore, the effects of horizontal motions (surge and sway) are especially important to consider. Fortunately, significant effort has been expended in describing the horizontal motions of moored floating platforms. For example, the dynamic coupling effects between a spar buoy and its mooring lines were analyzed and surge energy spectra were simulated for different water depths [63]. Low and Robin [64] compared the response prediction methods of a spread moored floating production storage and offloading (FPSO) platform and gave the spectral density figures for surge and sway. From [63] and [64], it was concluded that a slackly moored, large floating platform usually has a very low natural frequency due to its large mass and relatively small restoring stiffness. The responses of the floating platform are small in the wave frequency range [63]. However, the wave drift forces vary slowly, and these may excite the moored floating platform at its natural frequency, resulting in large low frequency motions. Thus, in these cases, the horizontal response is dominated by low frequency motion [65]. From [63–65], it is also seen that the shape and properties of the sway spectral density are similar to those for surge. The motion spectral density figures contained in these works show that there are

two dominant regions, representing contributions of the low frequency motion and wave frequency motion, respectively. By discretizing the spectra into  $N$  points, the surge and sway motions can be decomposed into  $N$  cosine functions, whose amplitudes and radian frequencies can be obtained from the spectral densities. Therefore, the platform motion model  $\delta\vec{\rho}_0$  can be expressed as

$$\delta\vec{\rho}_0(t) = \hat{\rho}_{p_x} \sum_{i=1}^N a_{xi} \cos(\omega_{xi}t + \phi_{xi}) + \hat{\rho}_{p_y} \sum_{l=1}^M a_{yl} \cos(\omega_{yl}t + \phi_{yl}) \quad (4.1)$$

where  $\hat{\rho}_{p_x}$  and  $\hat{\rho}_{p_y}$  represent the surge and sway directions, respectively, while  $a_{xi}$ ,  $\omega_{xi}$  and  $\phi_{xi}$  are, respectively, the amplitudes, radian frequencies and initial phases for the surge motion. Similarly,  $a_{yl}$ ,  $\omega_{yl}$  and  $\phi_{yl}$  are corresponding parameters of the sway motion.

### 4.3 Monostatic Radar Cross Sections for a Platform Motion Model Incorporating Dual-Frequency and Single Direction

To simplify the model used in this study, just one motion direction is initially considered, and the floating platform motion model is reduced to the combination of two cosine functions that represent the main components in the low frequency motion and the wave frequency motion region, respectively. Thus, the displacement of the floating platform (4.1) can be reduced to [66]

$$\delta\vec{\rho}_0(t) = [a_{x1} \cos(\omega_{x1}t + \phi_{x1}) + a_{x2} \cos(\omega_{x2}t + \phi_{x2})] \hat{\rho}_{p_x}. \quad (4.2)$$

Based on this simplified floating platform motion model, the first- and second-order RCSs with an antenna on a floating platform are derived below.

### 4.3.1 The First-Order Radar Cross Section Model

In [17], the first-order HFSWR cross section of the ocean surface with a single-frequency platform motion model was derived. Although different platform motion models are established and used to develop the radar cross sections, the general forms of the electric field equations and RCS models in [17] remain similar. Here, to avoid repetition, only the differences introduced by the new platform motion model are considered. The derivation of the first-order RCS in this chapter begins directly with (31) in [17] since at that point in the analysis the particular platform motion model is not yet specified. Thus,

$$\begin{aligned} \sigma_1(\omega_d) = & 2^2 k_0^2 \Delta \rho \sum_{m=\pm 1} \int_K \int_{\omega} K^2 S_1(m\vec{K}) \delta(\omega + m\sqrt{gK}) \text{Sa}^2\left[\frac{\Delta \rho}{2}(K - 2k_0)\right] \\ & \cdot \left\{ \int_{\tau} e^{j\tau(\omega - \omega_d)} \langle M(K, \theta_K, \tau, t) \rangle d\tau \right\} d\omega dK. \end{aligned} \quad (4.3)$$

By substituting the newly proposed floating platform motion model given in (4.2), the corresponding displacement term  $\langle M(K, \theta_K, \tau, t) \rangle$  may be expressed as

$$M(K, \theta_K, \tau, t) = e^{j\chi K \cos(\theta_K - \theta_{p_x})} \quad (4.4)$$

where  $\theta_{p_x}$  represents the surge direction of the platform motion and

$$\begin{aligned} \chi = & -a_{x1} \cos(\omega_{x1}t + \phi_{x1}) + a_{x1} \cos(\omega_{x1}t + \omega_{x1}\tau + \phi_{x1}) \\ & - a_{x2} \cos(\omega_{x2}t + \phi_{x2}) + a_{x2} \cos(\omega_{x2}t + \omega_{x2}\tau + \phi_{x2}). \end{aligned} \quad (4.5)$$

Now,  $\chi$  can be rearranged and expressed as

$$\begin{aligned} \chi = & -2a_{x1} \sin\left(\omega_{x1}t + \phi_{x1} + \frac{\omega_{x1}\tau}{2}\right) \sin\left(\frac{\omega_{x1}\tau}{2}\right) \\ & - 2a_{x2} \sin\left(\omega_{x2}t + \phi_{x2} + \frac{\omega_{x2}\tau}{2}\right) \sin\left(\frac{\omega_{x2}\tau}{2}\right). \end{aligned} \quad (4.6)$$

Thus, the ensemble average of  $M(K, \theta_K, \tau, t)$  may be written as

$$\langle M \rangle = \langle e^{j[v_1 \sin(\omega_{x1}t + \varphi_1) + v_2 \sin(\omega_{x2}t + \varphi_2)]} \rangle \quad (4.7)$$

where

$$v_1 = -2a_{x1}K \sin\left(\frac{\omega_{x1}\tau}{2}\right) \cos(\theta_K - \theta_{px})$$

$$v_2 = -2a_{x2}K \sin\left(\frac{\omega_{x2}\tau}{2}\right) \cos(\theta_K - \theta_{px})$$

$$\varphi_1 = \phi_{x1} + \frac{\omega_{x1}\tau}{2}$$

and

$$\varphi_2 = \phi_{x2} + \frac{\omega_{x2}\tau}{2}.$$

Also, from Euler's identity,

$$\begin{aligned} & e^{j[v_1 \sin(\omega_{x1}t + \varphi_1) + v_2 \sin(\omega_{x2}t + \varphi_2)]} \\ &= \{\cos[v_1 \sin(\omega_{x1}t + \varphi_1)] + j \sin[v_1 \sin(\omega_{x1}t + \varphi_1)]\} \\ & \cdot \{\cos[v_2 \sin(\omega_{x2}t + \varphi_2)] + j \sin[v_2 \sin(\omega_{x2}t + \varphi_2)]\}. \end{aligned} \quad (4.8)$$

Using the Bessel function relationships (as given, for example, in [67]),

$$\cos(x \sin(\phi)) = J_0(x) + 2 \sum_{n=1}^{\infty} J_{2n}(x) \cos(2n\phi) \quad (4.9)$$

and

$$\sin(x \sin(\phi)) = 2 \sum_{n=0}^{\infty} J_{2n+1}(x) \sin[(2n+1)\phi]. \quad (4.10)$$

Then, the expression in (4.8) can be expanded as

$$\begin{aligned}
& e^{j[v_1 \sin(\omega_{x1}t + \varphi_1) + v_2 \sin(\omega_{x2}t + \varphi_2)]} \\
&= \{J_0(v_1) + 2 \sum_{n_1=1}^{\infty} J_{2n_1}(v_1) \cos(2n_1 \varphi_{11}) + 2j \sum_{n_1=0}^{\infty} J_{2n_1+1}(v_1) \sin[(2n_1 + 1)\varphi_{11}]\} \\
&\cdot \{J_0(v_2) + 2 \sum_{n_2=1}^{\infty} J_{2n_2}(v_2) \cos(2n_2 \varphi_{22}) + 2j \sum_{n_2=0}^{\infty} J_{2n_2+1}(v_2) \sin[(2n_2 + 1)\varphi_{22}]\}
\end{aligned} \tag{4.11}$$

where  $\varphi_{11} = \omega_{x1}t + \varphi_1$  and  $\varphi_{22} = \omega_{x2}t + \varphi_2$ . From (4.11), the ensemble average of  $M(K, \theta_K, \tau, t)$  can be obtained by the summation of 9 separate ensemble average terms including

$$\langle J_0(v_1)J_0(v_2) \rangle = J_0(v_1)J_0(v_2), \tag{4.12}$$

$$\begin{aligned}
& \langle J_0(v_1) \cdot 2 \sum_{n_2=1}^{\infty} J_{2n_2}(v_2) \cos(2n_2 \varphi_{22}) \rangle \\
&= \frac{1}{T} \int_0^T J_0(v_1) \cdot 2 \sum_{n_2=1}^{\infty} J_{2n_2}(v_2) \cos(2n_2 \varphi_{22}) dt \\
&= \frac{2}{T} J_0(v_1) \cdot \sum_{n_2=1}^{\infty} J_{2n_2}(v_2) \int_0^T \cos(2n_2 \varphi_{22}) dt \\
&= 0,
\end{aligned} \tag{4.13}$$

and

$$\begin{aligned}
& \langle 2 \sum_{n_1=1}^{\infty} J_{2n_1}(v_1) \cos(2n_1 \varphi_{11}) \cdot 2 \sum_{n_2=1}^{\infty} J_{2n_2}(v_2) \cos(2n_2 \varphi_{22}) \rangle \\
&= \frac{1}{T} \int_0^T 2 \sum_{n_1=1}^{\infty} J_{2n_1}(v_1) \cos(2n_1 \varphi_{11}) \cdot 2 \sum_{n_2=1}^{\infty} J_{2n_2}(v_2) \cos(2n_2 \varphi_{22}) dt \\
&= \frac{4}{T} \sum_{n_1=1}^{\infty} J_{2n_1}(v_1) \cdot \sum_{n_2=1}^{\infty} J_{2n_2}(v_2) \cdot \int_0^T \cos(2n_1 \varphi_{11}) \cos(2n_2 \varphi_{22}) dt \\
&= 0.
\end{aligned} \tag{4.14}$$

The ensemble averages of the other 6 terms in (4.11) evaluate to zero. Thus, (4.7) reduces to

$$\begin{aligned}
\langle M \rangle &= J_0(v_1)J_0(v_2) \\
&= J_0[-2a_{x1}K \cos(\theta_K - \theta_{px}) \sin(\frac{\omega_{x1}\tau}{2})] \\
&\quad \cdot J_0[-2a_{x2}K \cos(\theta_K - \theta_{px}) \sin(\frac{\omega_{x2}\tau}{2})].
\end{aligned} \tag{4.15}$$

By using the relationship

$$J_0\left(2x \sin\left(\frac{\phi}{2}\right)\right) = \sum_{n=-\infty}^{\infty} J_n^2(x) \cos(n\phi) \tag{4.16}$$

and

$$J_n(-x) = (-1)^n J_n(x), \tag{4.17}$$

(4.15) reduces

$$\langle M \rangle = \sum_{n_1=-\infty}^{\infty} J_{n_1}^2(x_1) \cos(n_1 \omega_{x1} \tau) \sum_{n_2=-\infty}^{\infty} J_{n_2}^2(x_2) \cos(n_2 \omega_{x2} \tau) \tag{4.18}$$

where  $x_1 = a_{x1}K \cos(\theta_K - \theta_{px})$  and  $x_2 = a_{x2}K \cos(\theta_K - \theta_{px})$ .

Substituting the expression for  $\langle M(K, \theta_K, \tau, t) \rangle$  into the first-order RCS found in (4.3) gives

$$\begin{aligned}
\sigma_{1bfd}(\omega_d) &= 2^2 k_0^2 \Delta \rho \sum_{m=\pm 1} \int_K K^2 S_1(m\vec{K}) \text{Sa}^2\left[\frac{\Delta \rho}{2}(K - 2k_0)\right] \left\{ \int_{\tau} e^{-j\tau(m\sqrt{gK} + \omega_d)} \right. \\
&\quad \cdot \sum_{n_1=-\infty}^{\infty} J_{n_1}^2(x_1) \sum_{n_2=-\infty}^{\infty} J_{n_2}^2(x_2) \cos(n_1 \omega_{x1} \tau) \cos(n_2 \omega_{x2} \tau) d\tau \Big\} dK
\end{aligned} \tag{4.19}$$

By using the relationship  $2 \cos(n\omega\tau) = e^{jn\omega\tau} + e^{-jn\omega\tau}$ , and completing the  $\tau$  integral, the first-order RCS for the case of an antenna on a floating platform, whose displacement

is given in (4.2), may then be expressed as [68]

$$\begin{aligned} \sigma_{1bfd}(\omega_d) = & 2^3 \pi k_0^2 \Delta \rho \sum_{m=\pm 1} \int_K K^2 S_1(m\vec{K}) \text{Sa}^2\left[\frac{\Delta \rho}{2}(K - 2k_0)\right] \\ & \cdot \sum_{n_1=-\infty}^{\infty} J_{n_1}^2(x_1) \sum_{n_2=-\infty}^{\infty} J_{n_2}^2(x_2) \delta(\omega_d + m\sqrt{gK} + n_1\omega_{x1} + n_2\omega_{x2}) dK. \end{aligned} \quad (4.20)$$

### 4.3.2 The Second-Order Radar Cross Section Model

A general form of the received electric field for an antenna on a floating platform has been previously developed and appears as Equation (21) of [18]. Substituting the new platform motion model (4.2) into this electric field equation and following a similar analysis as used in [55], the second-order RCS may be written as [68]

$$\begin{aligned} \sigma_{2mfd}(\omega_d) = & 2^6 \pi^2 k_0^4 \sum_{m_1=\pm 1} \sum_{m_2=\pm 1} \int_0^{\infty} \int_{-\pi}^{\pi} S_1(m_1\vec{K}_1) S_1(m_2\vec{K}_2) |\Gamma_{P_m}|^2 K_1 \\ & \cdot \sum_{n_1=-\infty}^{\infty} J_{n_1}^2(x_1) \sum_{n_2=-\infty}^{\infty} J_{n_2}^2(x_2) \\ & \cdot \delta(\omega_d + m_1\sqrt{gK_1} + m_2\sqrt{gK_2} + n_1\omega_{x1} + n_2\omega_{x2}) d\theta_{\vec{K}_1} dK_1. \end{aligned} \quad (4.21)$$

## 4.4 Bistatic Radar Cross Sections for a Platform Motion Model Incorporating Dual-Frequency and Single Direction

Based on the floating platform proposed in (4.2), the first- and second-order bistatic radar cross sections for a platform motion model incorporating dual-frequency and single direction are developed.

#### 4.4.1 The First-Order Radar Cross Section Model

In [50], the first-order HFSWR bistatic cross section of the ocean surface incorporating a simple single-frequency platform motion model was derived. Here, the case for a platform motion model having a more realistic dual-frequency is investigated. By substituting the floating platform motion model (4.2) into  $M(K, \theta_K, \tau, t)$  in (2.20), the latter may be reduced to

$$M(K, \theta_K, \tau, t) = e^{j\frac{\chi K \cos(\theta_K - \theta_{px})}{2}} e^{j\frac{\chi K \tan \phi_0 \sin(\theta_K - \theta_{px})}{2}} \quad (4.22)$$

where

$$\begin{aligned} \chi = & -a_{x1} \cos(\omega_{p1}t + \phi_{p1}) + a_{x1} \cos(\omega_{p1}t + \omega_{p1}\tau + \phi_{p1}) \\ & - a_{x2} \cos(\omega_{p2}t + \phi_{p2}) + a_{x2} \cos(\omega_{p2}t + \omega_{p2}\tau + \phi_{p2}). \end{aligned} \quad (4.23)$$

Now,  $\chi$  can be rearranged and expressed as

$$\begin{aligned} \chi = & -2a_{x1} \sin(\omega_{p1}t + \phi_{p1} + \frac{\omega_{p1}\tau}{2}) \sin(\frac{\omega_{p1}\tau}{2}) \\ & - 2a_{x2} \sin(\omega_{p2}t + \phi_{p2} + \frac{\omega_{p2}\tau}{2}) \sin(\frac{\omega_{p2}\tau}{2}). \end{aligned} \quad (4.24)$$

Thus, the ensemble average of  $M(K, \theta_K, \tau, t)$  may be written as

$$\langle M \rangle = \langle e^{j[v_1 \sin(\omega_{p1}t + \varphi_1) + v_2 \sin(\omega_{p2}t + \varphi_2)]} \rangle \quad (4.25)$$

where

$$v_1 = -a_{x1} K \sin(\frac{\omega_{p1}\tau}{2}) [\cos(\theta_K - \theta_{px}) + \tan \phi_0 \sin(\theta_K - \theta_{px})]$$

$$v_2 = -a_{x2} K \sin(\frac{\omega_{p2}\tau}{2}) [\cos(\theta_K - \theta_{px}) + \tan \phi_0 \sin(\theta_K - \theta_{px})]$$

$$\varphi_1 = \phi_{p1} + \frac{\omega_{p1}\tau}{2}$$

and

$$\varphi_2 = \phi_{p2} + \frac{\omega_{p2}\tau}{2}.$$

Based on analysis similar to that in [66], it is possible to show that (4.25) may be reduced to

$$\langle M \rangle = \sum_{n_1=-\infty}^{\infty} J_{n_1}^2(x_1) \cos(n_1 \omega_{p1} \tau) \sum_{n_2=-\infty}^{\infty} J_{n_2}^2(x_2) \cos(n_2 \omega_{p2} \tau) \quad (4.26)$$

where

$$x_1 = \frac{1}{2} a_{x1} K [\cos(\theta_K - \theta_{p_x}) + \tan \phi_0 \sin(\theta_K - \theta_{p_x})] \quad (4.27)$$

and

$$x_2 = \frac{1}{2} a_{x2} K [\cos(\theta_K - \theta_{p_x}) + \tan \phi_0 \sin(\theta_K - \theta_{p_x})]. \quad (4.28)$$

Also, it is easy to show that

$$\cos(\theta_K - \theta_{p_x}) + \tan \phi_0 \sin(\theta_K - \theta_{p_x}) = \frac{\cos(\theta_1 - \theta_{p_x})}{\cos \phi_0}. \quad (4.29)$$

Thus, (4.27) and (4.28), respectively, become

$$x_1 = \frac{a_{x1} K}{2} \cos(\theta_1 - \theta_{p_x}) / \cos \phi_0 \quad (4.30)$$

and

$$x_2 = \frac{a_{x2} K}{2} \cos(\theta_1 - \theta_{p_x}) / \cos \phi_0. \quad (4.31)$$

Substituting the expression for  $\langle M(K, \theta_K, \tau, t) \rangle$  in (4.26) into (2.25) and completing the  $\tau$  integral, the first-order bistatic radar cross section  $\sigma_{1bfd}$  for the case of an antenna on a floating platform, whose displacement is given in (4.2), may then be expressed as [69]

$$\begin{aligned} \sigma_{1bfd}(\omega_d) = & 2^3 \pi k_0^2 \Delta \rho \sum_{m=\pm 1} \int_K K^2 \cos \phi_0 S_1(m\vec{K}) \text{Sa}^2 \left[ \frac{\Delta \rho}{2} \left( \frac{K}{\cos \phi_0} - 2k_0 \right) \right] \\ & \cdot \sum_{n_1=-\infty}^{\infty} J_{n_1}^2(x_1) \sum_{n_2=-\infty}^{\infty} J_{n_2}^2(x_2) \\ & \cdot \delta(\omega_d + m\sqrt{gK} + n_1 \omega_{p1} + n_2 \omega_{p2}) dK. \end{aligned} \quad (4.32)$$

From (4.30) and (4.31), it may be demonstrated that the modulation indices,  $x_1$  and  $x_2$ , are maximum when  $\theta_1 = \theta_{p_x}$  and are minimum when  $\theta_{p_x}$  is perpendicular to  $\theta_1$ . It can also be observed from (4.27) and (4.28) that when  $\sin(\theta_K - \theta_{p_x}) > 0$ , the modulation indices  $x_1$  and  $x_2$  increase with bistatic angle  $\phi_0$ , resulting in a greater modulation effect on the Doppler spectra. An opposite conclusion is reached when  $\sin(\theta_K - \theta_{p_x}) < 0$ . In addition, when  $\theta_{p_x} = \theta_K$ , the modulation effect is unrelated to the bistatic angle.

#### 4.4.2 The Second-Order Radar Cross Section Model

Substituting the dual-frequency platform motion model (4.2) into (2.51) and following a similar analysis as that appearing in the first-order case in Section 4.4.1, the second-order bistatic radar cross section  $\sigma_{2bfd}$  for this new floating platform motion model may be expressed as [69]

$$\begin{aligned} \sigma_{2bfd}(\omega_d) = & 2^6 \pi^2 k_0^4 \cos^4 \phi_0 \sum_{m_1=\pm 1} \sum_{m_2=\pm 1} \int_0^\infty \int_{-\pi}^\pi S_1(m_1 \vec{K}_1) S_1(m_2 \vec{K}_2) |\Gamma_{P_b}|^2 K_1 \\ & \cdot \sum_{n_1=-\infty}^\infty J_{n_1}^2(x_1) \sum_{n_2=-\infty}^\infty J_{n_2}^2(x_2) \\ & \cdot \delta(\omega_d + m_1 \sqrt{gK_1} + m_2 \sqrt{gK_2} + n_1 \omega_{p1} + n_2 \omega_{p2}) d\theta_{\vec{K}_1} dK_1. \end{aligned} \quad (4.33)$$

### 4.5 Radar Cross Sections for a More Complicated Platform Motion Model

#### 4.5.1 Platform Motion Model Having Multiple Frequencies

If all the frequency components in one direction in the spectrum of the floating platform are considered, the platform displacement (4.1) can be reduced to

$$\delta \vec{\rho}_0(t) = \hat{\rho}_{p_x} \sum_{i=1}^N a_{xi} \cos(\omega_{xi} t + \phi_{xi}), \quad (4.34)$$

in which case the first-order RCS incorporating a multi-frequency platform motion model may be written as

$$\begin{aligned}
\sigma_{1fm}(\omega_d) &= 2^3 \pi k_0^2 \Delta \rho \sum_{m=\pm 1} \int_K K^2 S_1(m\vec{K}) \text{Sa}^2 \left[ \frac{\Delta \rho}{2} (K - 2k_0) \right] \\
&\cdot \sum_{n_1=-\infty}^{\infty} J_{n_1}^2(x_1) \sum_{n_2=-\infty}^{\infty} J_{n_2}^2(x_2) \cdots \sum_{n_N=-\infty}^{\infty} J_{n_N}^2(x_N) \\
&\cdot \delta(\omega_d + m\sqrt{gK} + n_1\omega_{x1} + n_2\omega_{x2} + \cdots + n_N\omega_{xN}) dK.
\end{aligned} \tag{4.35}$$

The corresponding second-order RCS may be expressed as

$$\begin{aligned}
\sigma_{2fm}(\omega_d) &= 2^6 \pi^2 k_0^4 \sum_{m_1=\pm 1} \sum_{m_2=\pm 1} \int_0^{\infty} \int_{-\pi}^{\pi} S_1(m_1\vec{K}_1) S_1(m_2\vec{K}_2) |\Gamma_P|^2 K_1 \\
&\cdot \sum_{n_1=-\infty}^{\infty} J_{n_1}^2(x_1) \sum_{n_2=-\infty}^{\infty} J_{n_2}^2(x_2) \cdots \sum_{n_N=-\infty}^{\infty} J_{n_N}^2(x_N) \\
&\cdot \delta(\omega_d + m_1\sqrt{gK_1} + m_2\sqrt{gK_2} + n_1\omega_{x1} + n_2\omega_{x2} + \cdots + n_N\omega_{xN}) d\theta_{\vec{K}_1} dK_1.
\end{aligned} \tag{4.36}$$

It is worth noting that (4.35) and (4.36) are suitable for both monostatic and bistatic geometries. For a monostatic geometry,  $x_i = a_{xi}K \cos(\theta_K - \theta_{p_x})$  and  $\Gamma_P = \Gamma_{P_m}$ . For bistatic geometry,  $x_i = \frac{a_{xi}K}{2} \cos(\theta_1 - \theta_{p_x}) / \cos \phi_0$  and  $\Gamma_P = \Gamma_{P_b}$ . From (4.35) and (4.36), it may be observed that the radar cross sections contain a product of infinite sums of a various orders of Bessel functions with each sum being the contribution of a platform motion frequency component.

## 4.5.2 Platform Motion Model Incorporating Surge and Sway Directions

In this section, the general platform motion model given in (4.1) is considered. Derivations similar to those used in Section 4.3 can be conducted to obtain the corresponding RCS models. These models also consist of products of infinite sums of Bessel functions, whose parameters depend on the platform motion amplitudes, ocean wavenumbers and

the angles between the radar look direction and the motion directions. The first-order RCS for the floating platform model shown in (4.1) can be expressed as

$$\begin{aligned}
\sigma_{1fa}(\omega_d) &= 2^3 \pi k_0^2 \Delta \rho \sum_{m=\pm 1} \int_K K^2 S_1(m\vec{K}) \text{Sa}^2 \left[ \frac{\Delta \rho}{2} (K - 2k_0) \right] \\
&\cdot \sum_{n_1=-\infty}^{\infty} J_{n_1}^2(x_1) \sum_{n_2=-\infty}^{\infty} J_{n_2}^2(x_2) \cdots \sum_{n_N=-\infty}^{\infty} J_{n_N}^2(x_N) \\
&\cdot \sum_{q_1=-\infty}^{\infty} J_{q_1}^2(y_1) \sum_{q_2=-\infty}^{\infty} J_{q_2}^2(y_2) \cdots \sum_{q_M=-\infty}^{\infty} J_{q_M}^2(y_M) \\
&\cdot \delta(\omega_d + m\sqrt{gK} + n_1\omega_{x1} + n_2\omega_{x2} + \cdots + n_N\omega_{xN} \\
&\quad + q_1\omega_{y1} + q_2\omega_{y2} + \cdots + q_M\omega_{yM}) dK
\end{aligned} \tag{4.37}$$

where  $\theta_{py}$  is the direction of the sway motion. The corresponding second-order RCS may be written as

$$\begin{aligned}
\sigma_{2fa}(\omega_d) &= 2^6 \pi^2 k_0^4 \sum_{m_1=\pm 1} \sum_{m_2=\pm 1} \int_0^{\infty} \int_{-\pi}^{\pi} S_1(m_1\vec{K}_1) S_1(m_2\vec{K}_2) |\Gamma_P|^2 K_1 \\
&\cdot \sum_{n_1=-\infty}^{\infty} J_{n_1}^2(x_1) \sum_{n_2=-\infty}^{\infty} J_{n_2}^2(x_2) \cdots \sum_{n_N=-\infty}^{\infty} J_{n_N}^2(x_N) \\
&\cdot \sum_{q_1=-\infty}^{\infty} J_{q_1}^2(y_1) \sum_{q_2=-\infty}^{\infty} J_{q_2}^2(y_2) \cdots \sum_{q_M=-\infty}^{\infty} J_{q_M}^2(y_M) \\
&\cdot \delta(\omega_d + m_1\sqrt{gK_1} + m_2\sqrt{gK_2} + n_1\omega_{x1} + n_2\omega_{x2} + \cdots + n_N\omega_{xN} \\
&\quad + q_1\omega_{y1} + q_2\omega_{y2} + \cdots + q_M\omega_{yM}) d\theta_{\vec{K}_1} dK_1.
\end{aligned} \tag{4.38}$$

It is worth noting that (4.37) and (4.38) are also suitable for both monostatic and bistatic geometries. As before, for a monostatic geometry,  $x_i = a_{xi}K \cos(\theta_K - \theta_{px})$  and  $\Gamma_P = \Gamma_{P_m}$ , while, for a bistatic geometry,  $x_i = \frac{a_{xi}K}{2} \cos(\theta_1 - \theta_{px}) / \cos \phi_0$  and  $\Gamma_P = \Gamma_{P_b}$ .

## 4.6 Simulation and Analysis

Using a Pierson-Moskowitz ocean spectral model for a fully developed wind sea, simulations to illustrate the effects of antenna motion for the newly derived RCSs are conducted.

The radar operating frequency, wind speed, and patch width are taken to be 15 MHz, 15 m/s and 3000 m, respectively. The wind direction is  $90^\circ$  with respect to the radar look direction. It should be noted that the minimum distance between the floating platform and the patch of the ocean the HFSWR observes will be, in general, tens of kilometers [9]. Thus, sea states at the platform and the patch do not have to be the same. The parameters for the platform motion are obtained from [70], where the horizontal motions of a moored FPSO platform in bi-directional swell and wind-sea with a significant wave height  $H_s=2.06$  m, offshore of West Africa, were analysed. From this work,  $a_{x1} = 5$  m,  $a_{x2} = 0.35$  m,  $\omega_{x1} = 0.02$  rad/s and  $\omega_{x2} = 0.35$  rad/s are used. A Hamming window is used to smooth the curve and reduce oscillatory features caused by the  $Sa^2$  function in the presented models (see Section 4.3 and 4.4).

Using these values results in the Doppler spectra shown in Fig. 4.1 and Fig. 4.2. As depicted in Fig. 4.1, the motion-induced peaks appear symmetrically in the Doppler spectrum at frequencies given by  $\omega_d = \omega_B + n_1 \omega_{x1} + n_2 \omega_{x2}$ , where  $\omega_B$  represents the Doppler frequency of the Bragg peaks. When there is no platform motion, the typical Bragg peaks are seen. Comparing with the case of the fixed antenna, both the low frequency platform motion and the wave frequency platform motion cause motion-induced peaks in the Doppler spectra and broaden the region of the Bragg peaks. Compared to previous studies that considered only single-frequency platform motion [17–19], the Bragg peaks and the peaks caused by the wave frequency motion, shown in Fig. 4.2, are broadened by the low frequency motion.

From the RCS model derived in Section 4.3, it may be seen that the initial phases of the platform motions have no effect on the radar cross sections. Rather, the radian frequencies of the platform motions determine the frequency locations of the motion-induced peaks. In addition, the amplitudes of these motion-induced peaks are determined by the amplitudes of the platform motions. The radian frequencies and relative amplitudes of the Bragg peaks and motion-induced peaks are shown in Table 4.1. The relative amplitude in Table 4.1 refers to the ratio of the actual peak amplitude to the amplitude

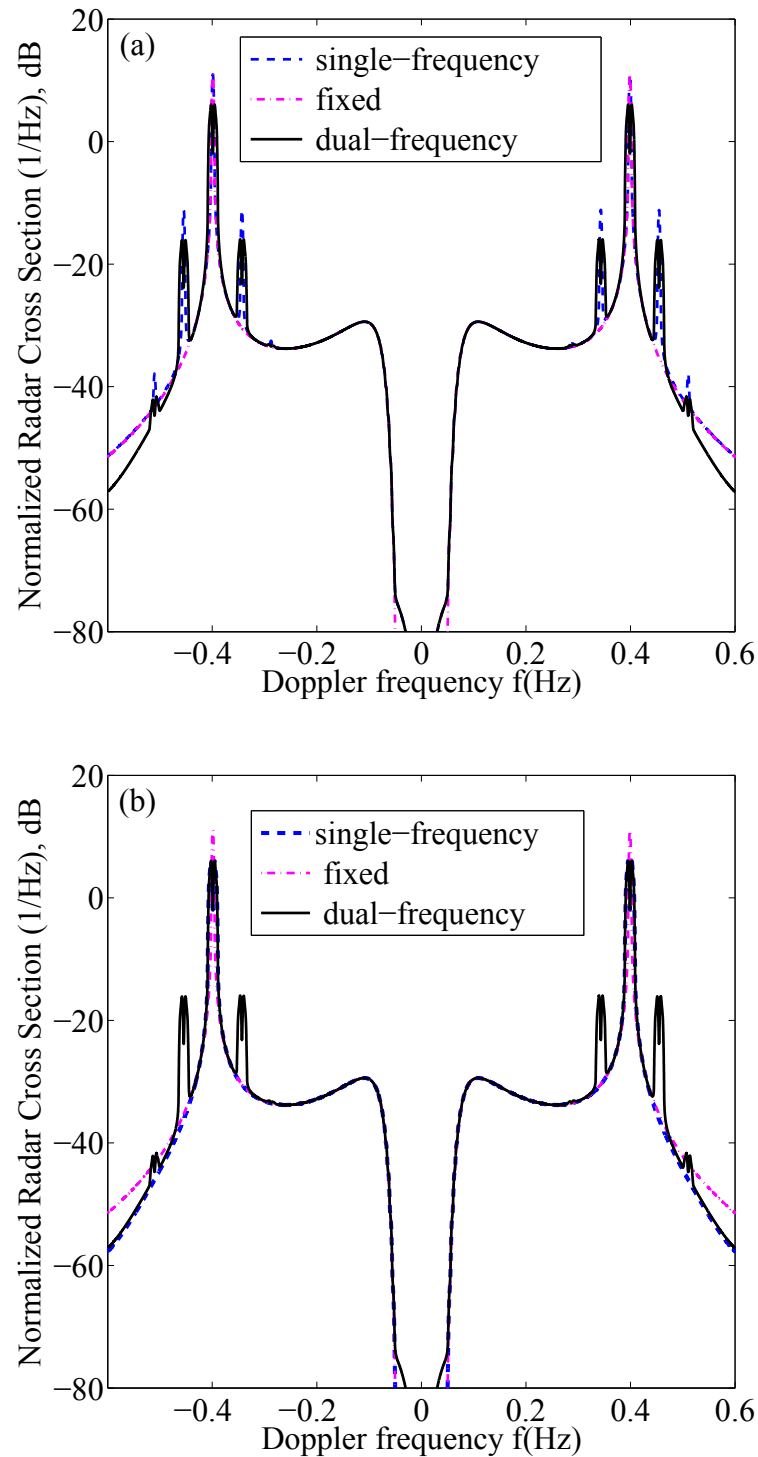


Fig. 4.1 Comparison of the first-order radar cross sections under a moderate sea state of  $H_s = 2.06$  m (see text for other model parameters) for a fixed antenna with those for a floating antenna, respectively, incorporating a dual-frequency platform motion and (a) a single wave frequency platform motion; (b) a single low frequency platform motion.

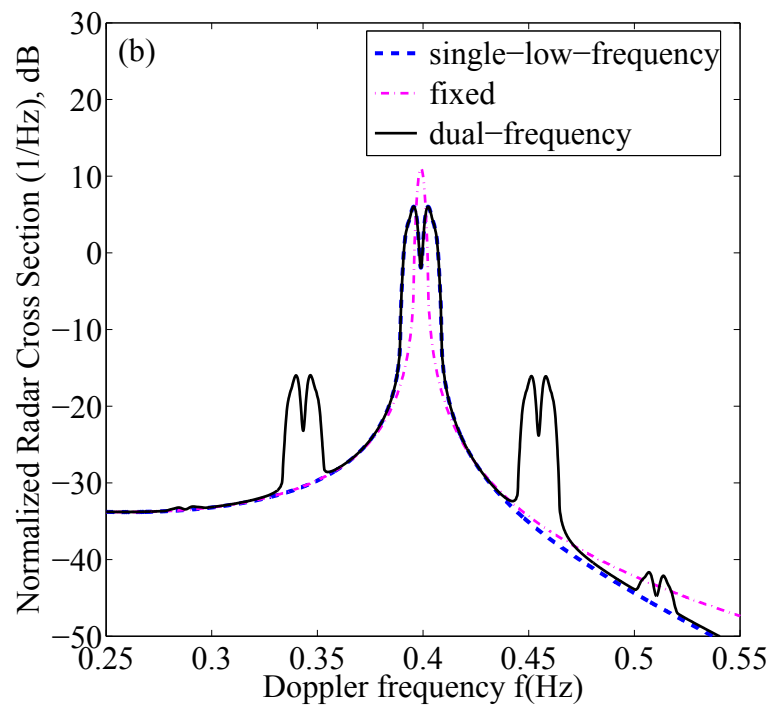
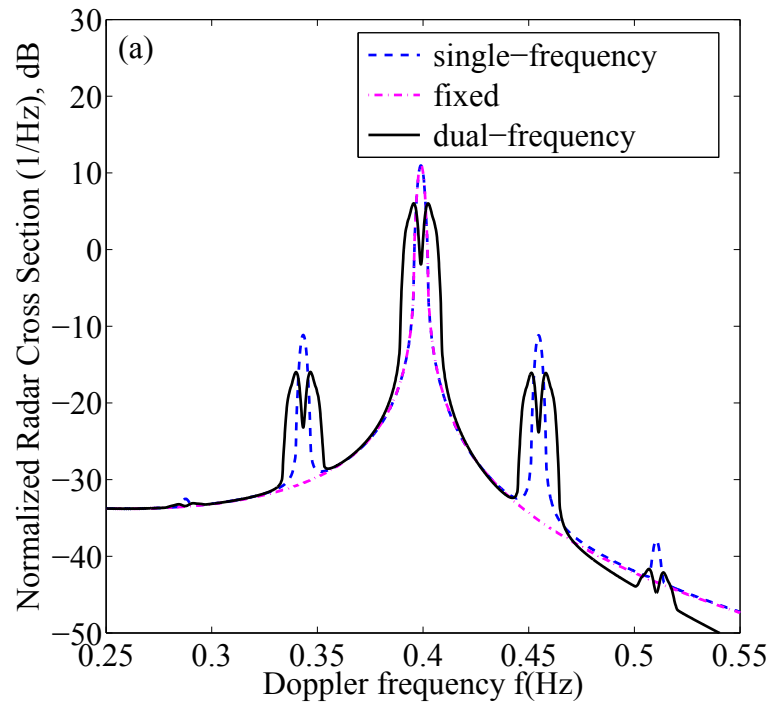


Fig. 4.2 Zoomed-in view of the positive Doppler spectrum (a) in Fig. 4.1(a); (b) in Fig. 4.1(b).

of the Bragg peak for the case of a fixed antenna. From both Table 4.1 and Fig. 4.1, it can be seen that the magnitudes of the Bragg peaks for the case of a floating antenna are lower than those for the case of a fixed antenna due to  $|J_n(x)| \leq 1$  for any  $n$  and  $x$ , but the total spectral powers are the same in both cases.

Table 4.1 The radian frequencies and relative amplitudes of Bragg peaks and motion-induced peaks

Type of peaks	Doppler frequency	Relative amplitude
Bragg peaks	$\pm \omega_B$	$J_0^2(x_1)J_0^2(x_2)$
Low frequency motion-induced peaks	$\pm \omega_B \pm n_1 \omega_{x1}$	$J_{n_1}^2(x_1)J_0^2(x_2)$
Wave frequency motion-induced peaks	$\pm \omega_B \pm n_2 \omega_{x2}$	$J_0^2(x_1)J_{n_2}^2(x_2)$
Combined motion-induced peaks	$\pm \omega_B \pm n_1 \omega_{x1} \pm n_2 \omega_{x2}$	$J_{n_1}^2(x_1)J_{n_2}^2(x_2)$

In [71], for example, it is noted that if a sinusoidal signal is frequency modulated by a signal involving two sinusoidal waves, the frequency modulated wave can be expressed as  $e = E_0 \sin(\omega t + l_1 \sin p_1 t + l_2 \sin p_2 t)$ , where  $E_0$  represents the amplitude of the wave,  $\omega$  is the radian frequency of the carrier, and  $l_1$  and  $l_2$  are the modulation indices with corresponding modulating radian frequencies  $p_1$  and  $p_2$ . As also noted in [71], the frequencies of the sideband components appear at  $\omega + n_1 p_1 + n_2 p_2$ , where  $n_1$  and  $n_2$  can be any integer. In addition, the amplitudes of the carrier and sideband components equal the products of Bessel's functions with the arguments being the modulation indices. This conclusion agrees well with the derived RCS models (see Section 4.3). Therefore, the floating platform motion may be viewed as modulating the radar signals. The modulation indices are related to the amplitudes of the platform motions and the angles between the motion directions with the radar look direction. The value of the modulation index determines how much energy is transferred from the carrier to the sideband components. In this context, the Bragg peaks can be treated as the carrier and the motion-induced peaks may be viewed as sideband components. It is worth noting that the relative amplitudes shown in Table 4.1 equal the products of the square of Bessel's functions instead of the products of Bessel's functions. This is because the radar cross sections represent the power spectral density, resulting in a square operation in the amplitude.

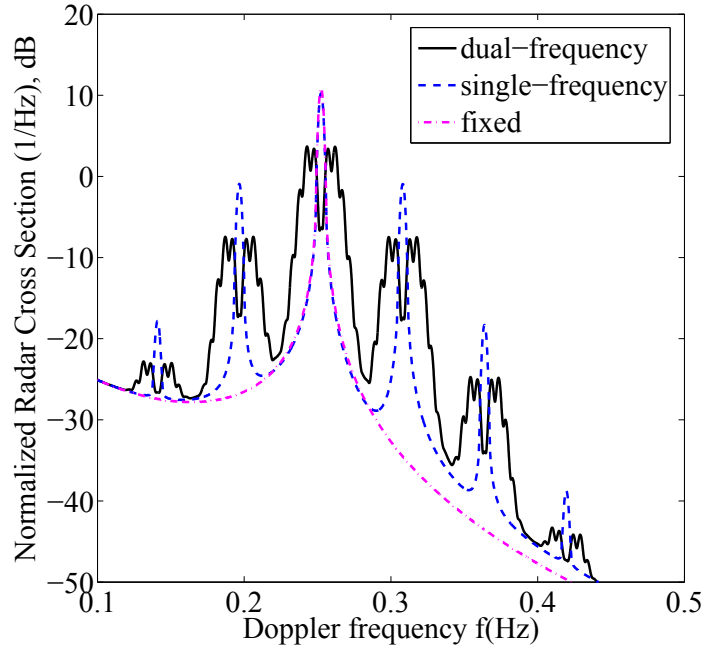


Fig. 4.3 Comparison of the first-order positive Doppler spectra under an extremely high sea state of  $H_s = 15.7$  m for a fixed antenna with that for a floating antenna.

Fig. 4.3 describes the first-order radar cross section incorporating a dual-frequency platform motion model under storm conditions associated with sea state 11 with a significant wave height  $H_s = 15.7$  m. It is shown in [72] that the saturation limit on the significant wave height is defined approximately by  $H_{sat} = 2/k_0$ . Thus, the highest applicable radar operating frequency is around 6 MHz and this is used in the simulation shown in Fig. 4.3. For a high sea state, the amplitudes of both the low frequency platform motion and the wave frequency platform motion increase with increasing wind speed. With increasing amplitude of the platform motion, the energy of the Bragg peaks decreases, the bandwidth of the Bragg peaks widens, more energy is transferred from Bragg peaks to sideband components, and more sideband components need to be considered. In Fig. 4.2, only the Bessel functions up to the second-order are used, while Bessel functions up to the sixth-order are considered in Fig. 4.3. For an extremely high sea state, the Bragg peak tends to be flatter and smoother instead of being a single sharp peak.

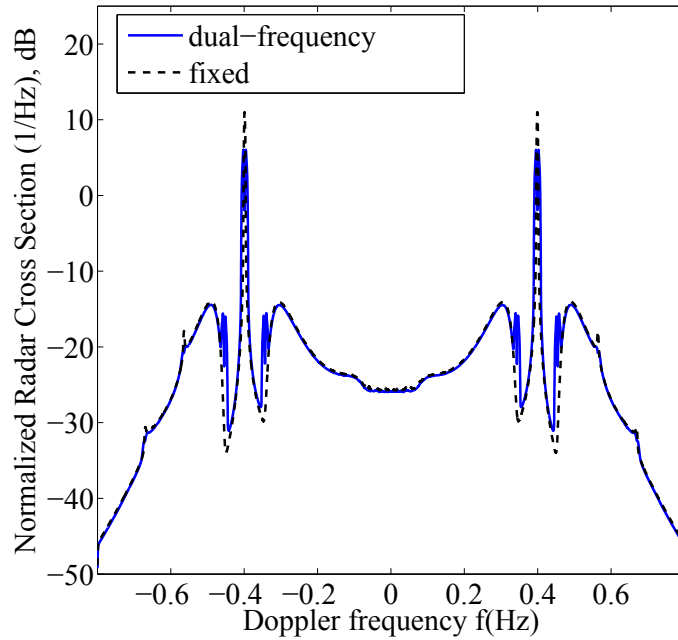


Fig. 4.4 Comparison of the total (including the first- and second-order) radar cross sections under a moderate sea state of  $H_s = 2.06$  m for a fixed antenna with that for a floating antenna.

Fig. 4.4 shows the comparison of the total radar cross section (including the first- and second-order radar cross sections) with an antenna on a floating platform with that for a fixed antenna. The third- and higher-order radar cross sections are ignored in this study due to their little contribution to the total radar cross section. The simulation parameters used to generate Fig. 4.4 are the same as those used in Figs. 4.1 and 4.2. Four obvious motion-induced peaks, around  $\pm 0.35$  Hz and  $\pm 0.45$  Hz, can be observed in Fig. 4.4. These four motion-induced peaks are the first-order motion-induced peaks, which can also be found in Figs. 4.1 and 4.2. Due to their small magnitudes, the second-order motion-induced peaks cannot be seen in Fig. 4.4. As explained in [18] and [55], this is because the motion-induced peaks have less energy in the second-order than in the first-order radar cross section.

A total radar cross section under an extremely high sea state with an antenna on a floating platform is depicted in Fig. 4.5. The simulation parameters are the same as those used in generating Fig. 4.3. From Fig. 4.4 and Fig. 4.5, it can be seen that, as expected,

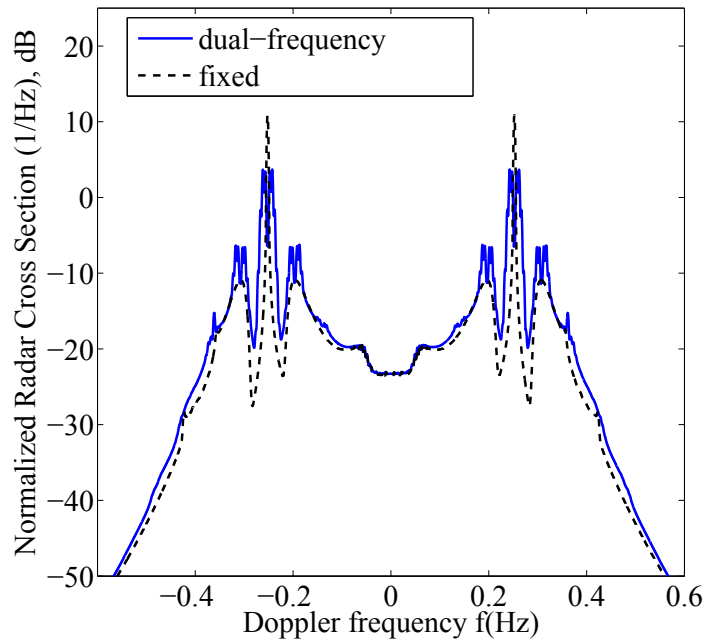


Fig. 4.5 Comparison of the total radar cross sections under an extremely high sea state of  $H_s = 15.7$  m for a fixed antenna with that for a floating antenna.

the modulation effect on the radar cross section is significant when the amplitudes of the platform motions are large. From these figures, it can be seen that a fraction of the energy is transferred from the Bragg peaks to the motion-induced peaks. In the process of the energy transfer, wave frequency platform motions rather than low frequency motions play a dominant role. In Fig. 4.5, some of the first-order motion-induced peaks are located in the region of the second-order radar cross section. If the effect of the platform motion is ignored in interpreting the Doppler spectra, this will cause an overestimation of the significant wave height. This effect has also been observed in experimental data [9] in which it was reported that during North Sea winter storm conditions, using an HFSSWR system operated aboard a semisubmersible oil platform, the wave height was overestimated by 40%. By comparison, for the conditions associated with Fig. 4.4, little energy is transferred from the first-order radar cross section to the second-order, and, in this case, the effect of the platform motion may be ignored in the second-order inversion process. Thus, it can be concluded that the estimation of significant wave

height will be affected by many factors, such as the amplitudes and radian frequencies of the platform motion. Meanwhile, this estimated value is also affected by wind speed and radar operating frequency. As shown in [50] and [55], the amplitudes and radian frequencies of the platform motion are seen to increase and decrease, respectively, with increasing wind speed. Additionally, in [50] and [55], the energies of the motion-induced peaks, for a given sea state, are found to decrease as the radar operating frequency is reduced.

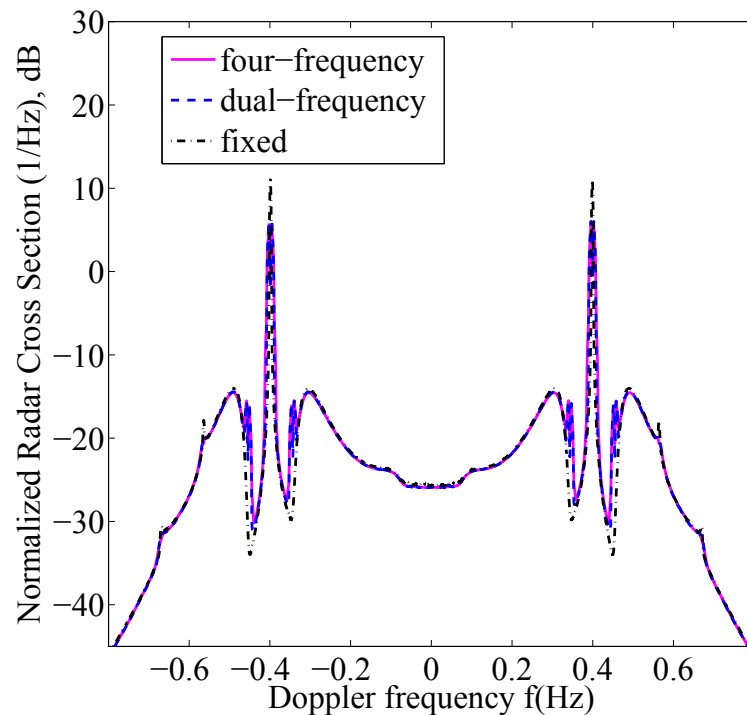


Fig. 4.6 Comparison of the total radar cross sections incorporating a multi-frequency platform motion model under a moderate sea state 3 of  $H_s = 2.06$  m for a fixed antenna with that for a floating antenna.

Spectra obtained using the multi-frequency platform motion model that incorporates both surge and sway directions are generated using the same parameters as used for Fig. 4.1. Results are presented in Fig. 4.6 and Fig. 4.7. Keeping the two frequency components used in Fig. 4.4 unchanged, the results using a platform motion model incorporating four frequency components are shown in Fig. 4.6. Little difference is

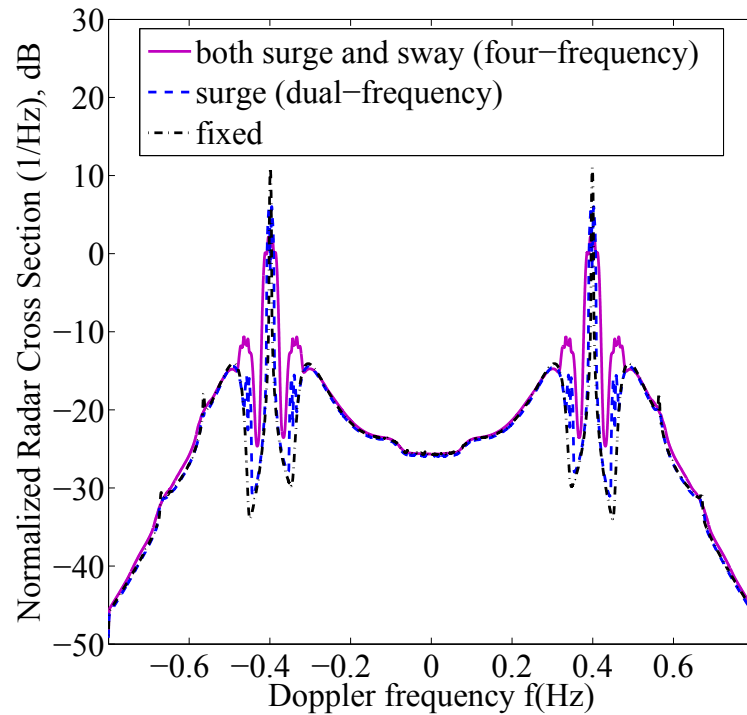


Fig. 4.7 Comparison of the total radar cross sections considering both surge and sway directions under a moderate sea state 3 of  $H_s = 2.06$  m for a fixed antenna with that for a floating antenna.

observed in Fig. 4.6 between the radar cross section incorporating a four-frequency platform motion model and that having dual-frequency. This is because the amplitudes for the third and fourth frequency components are much smaller compared to those for the first two frequency components. Similarly, keeping the two frequency components in the surge direction used in Fig. 4.4 unchanged, the results using a platform motion model considering both surge and sway directions are shown in Fig. 4.7. It can be seen from Fig 4.7 that the modulation effect on the radar cross section, considering both surge and sway directions, is greater than that when considering only the surge direction. This is because for this floating, moored platform, the amplitudes of the two frequency components in the sway direction are much greater than those in the surge direction.

Simulations are also undertaken to investigate the effects of bistatic angle on the new radar cross sections. The radar operating frequency, wind speed and patch width are

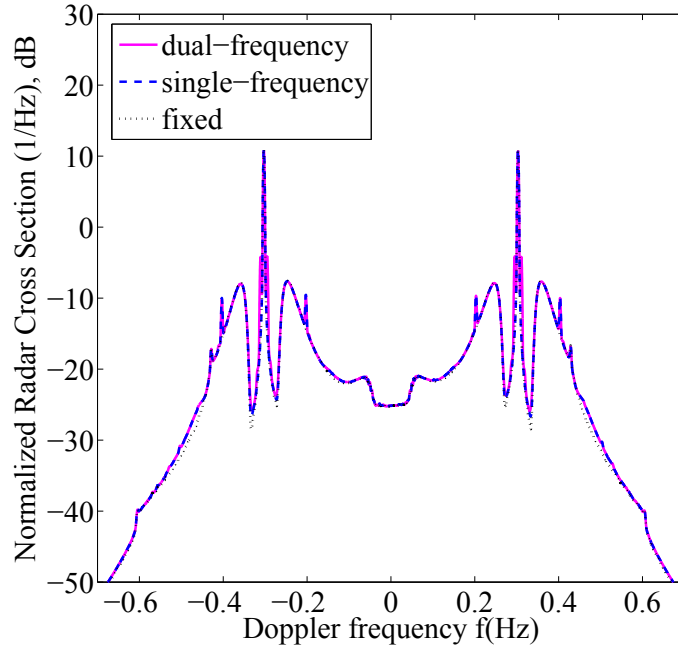


Fig. 4.8 Comparison of bistatic radar cross sections under a high sea state of  $H_s = 8$  m for a fixed antenna with that for a floating antenna.

taken to be 10 MHz, 25 m/s and 3000 m, respectively. The wind direction and ellipse normal are  $175^\circ$  and  $85^\circ$ , respectively, as measured from the positive  $x$  axis (the line connecting the transmitter to the receiver). The parameters for the platform motion are obtained from [88], where the time series of the surge motion were given under a significant wave height of  $H_s = 8$  m (strong gale, sea state 9). From that work, the dual-frequency platform motion model of (4.2) is used in the simulation, with  $a_{x1}$ ,  $\omega_{x1}$ ,  $a_{x2}$ , and  $\omega_{x2}$  being 2 m, 0.05 rad/s, 0.9 m and 0.63 rad/s, respectively.

Comparisons of the radar cross sections for an antenna on a floating platform with that for a fixed antenna are shown in Figs. 4.8 and 4.9. The bistatic angle  $\phi_0$  in Figs. 4.8 and 4.9 is taken to be  $30^\circ$ . From these two figures, it is observed that the analysis of how antenna motion affects the bistatic Doppler spectrum, and the difference between bistatic radar cross sections for a dual-frequency platform motion model with those for a single frequency motion model, are similar to the monostatic case. The effects of different sea states and radar parameters have been previously shown in this section for the monostatic

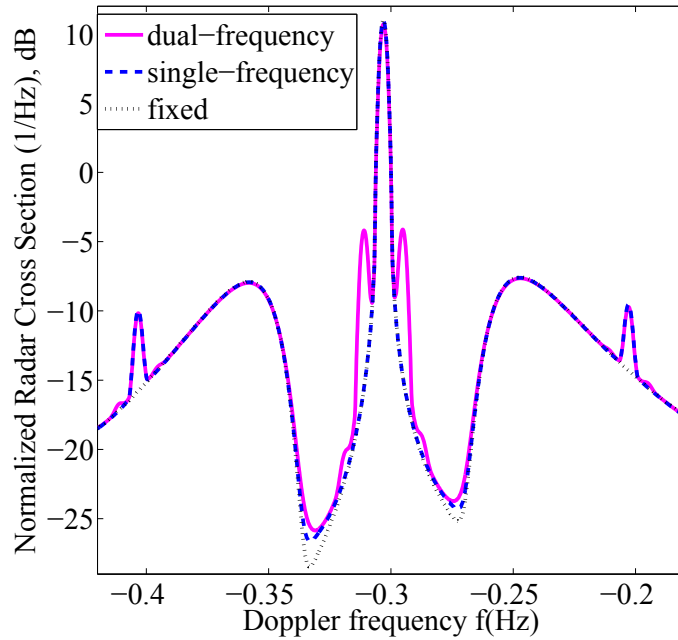


Fig. 4.9 Zoomed-in view of the negative Doppler spectrum in Fig. 4.8.

radar cross section model. Similar effects are observed for the bistatic case and are not further addressed here.

In order to clearly show how the bistatic angle affects the modulation extent of the radar cross sections, the parameters for the platform motion are obtained under an extreme sea state. In [89], the time series of the surge motion was recorded under environmental conditions associated with a 100 year storm with which was associated a significant wave height of 14 m and wave period of 15.8 s. Based on this work, the platform motion data involving two main frequency components is taken:  $a_{x1} = 10$  m,  $\omega_{x1} = 0.08$  rad/s,  $a_{x2} = 5$  m, and  $\omega_{x2} = 0.63$  rad/s. Through the saturation limit on the significant wave height, the radar operating frequency is taken to be 5 MHz.

Fig. 4.10 and Fig. 4.11 show radar cross sections with an antenna on a floating platform for different bistatic angles. The directions of the platform motion in Fig. 4.10 and Fig. 4.11 are  $0^\circ$  and  $90^\circ$ , for which  $\sin(\theta_K - \theta_{p_x})$  corresponds to a positive number and a negative number, respectively. It may be observed from Fig. 4.10 and Fig. 4.11 that the frequencies of the Bragg peaks and the second-order hydrodynamic and electromagnetic

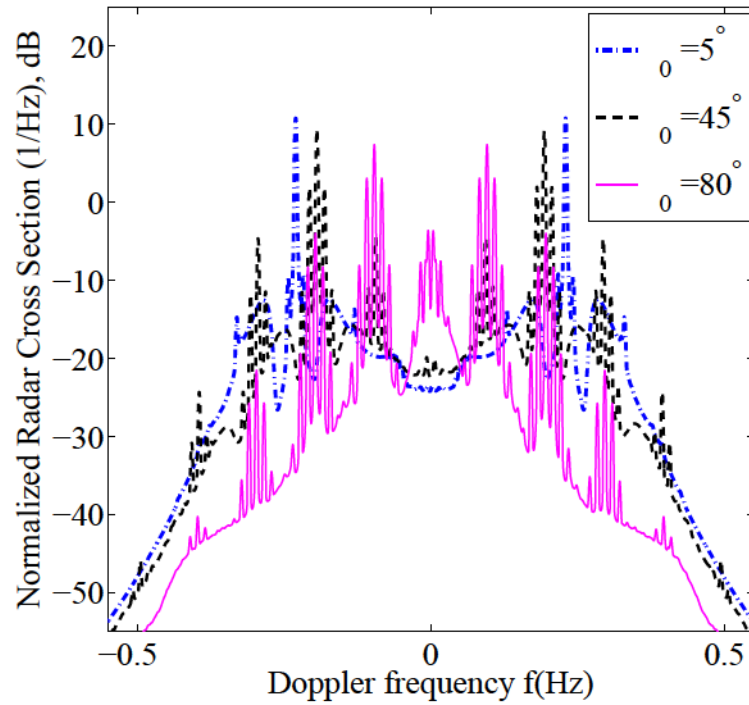


Fig. 4.10 Comparison of bistatic radar cross sections for different bistatic angles with the platform motion direction of  $0^\circ$  under environmental conditions associated with sea state 11.

peaks are closer to zero Doppler frequency for a larger bistatic angle. In addition, the energies of both the second-order hydrodynamic and electromagnetic peaks are found to decrease with increasing bistatic angle. This has been examined in detail in [73]. In Fig. 4.10, the modulation effect is seen to increase with increasing bistatic angle, while in Fig. 4.11 a decrease is observed. This conclusion agrees well with the cross section models derived in Section 4.4. In addition, the amplitudes of the Bragg peaks in Fig. 4.10 and Fig. 4.11 are mainly determined by the amplitude of the modulation index. When the modulation index is large, the modulation effect is obvious, resulting in more energy being transferred from the Bragg peaks to the motion-induced peaks [66].

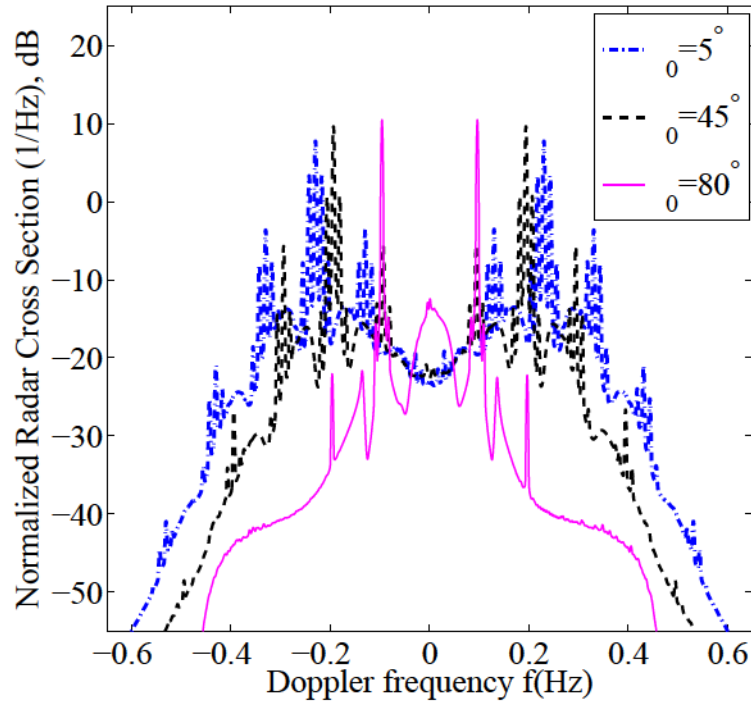


Fig. 4.11 Comparison of bistatic radar cross sections for different bistatic angles with the platform motion direction of  $90^\circ$  under environmental conditions associated with sea state 11.

## 4.7 Chapter Summary

The development of HFSWR first- and second-order ocean surface cross section models with a more realistic platform motion model than appears in [50] and [55] has been presented. First, a platform motion model containing two cosine waves in one direction, representing the low frequency motion and the wave frequency motion has been considered. Then, the platform motion model is extended to include multiple frequencies and both surge and sway directions.

It has been shown that the platform motion can be viewed as modulating the radar frequencies and the modulation indices are related to the amplitudes of the motion. It has also been shown that this frequency modulation has a much greater effect on the first-order RCS than it does on the second-order. Simulation results show that a fraction

of the energy is transferred from the Bragg peaks to the motion-induced peaks, which may be located in the region of the second-order radar cross section.

If the effect of the platform motion is ignored in interpreting the Doppler spectra, these motion-induced peaks may raise the second-order radar cross section. This would result in an overestimation of the significant wave height, an effect which has been observed in experimental data [9]. In addition, the regions of the Bragg peaks have been shown to be broadened by the sideband components, a fact which agrees with the field data presented in [74]. It is worth noting that in [35–37] the platform motion is linear since a shipborne HFSWR was used. For such a case, the Bragg frequencies drift due to the platform motion. Here, the platform motion is represented using a sinusoidal function. In this situation, the frequencies of the Bragg peaks are not shifted, but a fraction of the energy is transferred from the Bragg peaks to the motion-induced peaks due to the frequency modulation effect as explained, for example, in [71].

Simulations have been conducted to demonstrate the effect of the bistatic angle on the radar cross sections. The bistatic angle affects both the power of the second-order received Doppler spectra and the modulation level of the platform motion on the radar cross sections. In addition, it has been shown that the size of the modulation level has a dramatic effect on the energy of the Bragg peaks in the radar cross sections. The results are expected to provide a good theoretical basis for determining suitable geometries for the deployment of platform-mounted bistatic HFSWR.

The RCS models developed have been analysed using simulated data. The analysis will assist in the design of future field experimentation needed to further validate these models. From (4.37) and (4.38), it is seen that although pitch and roll movements have not been considered here, a similar method to that used in [9] can be adopted by transferring pitch and roll movements to the horizontal and vertical planes, extracting the horizontal components, and adding these extracted components to the surge and sway movements into the platform motion model.

# **Chapter 5**

## **Motion Compensation for High Frequency Surface Wave Radar on a Floating Platform**

### **5.1 Introduction**

Based on radar cross section models for an antenna on a floating platform found in Chapter 4, a new compensation method for mitigating the platform motion effect is proposed in this chapter. In Section 5.2, the first- and second-order radar cross section models for a fixed antenna are reviewed. The relationship between the radar cross sections for a fixed antenna and for an antenna on a floating platform is established in Section 5.3. Through this relationship, a motion compensation method, which involves deconvolving the radar cross section data with the derived transfer function, is proposed. Four different deconvolution techniques are illustrated in Section 5.4. Then, in Section 5.5, the radar cross section model for an antenna on a floating platform with external white Gaussian noise is developed. Application of the proposed compensation method, along with results obtained under different sea states and SNRs, appears in Section 5.6. Section 5.7 contains conclusions and suggestions for future investigations.

## 5.2 Radar Cross Sections

The first-order monostatic HFSWR cross section of the ocean surface  $\sigma_{1_{fixed}}$  for the case of a fixed antenna may be written as [75]

$$\sigma_{1_{fixed}}(\omega_d) = 2^3 \pi k_0^2 \Delta \rho \sum_{m=\pm 1} \int_K K^2 S_1(m\vec{K}) \text{Sa}^2 \left[ \frac{\Delta \rho}{2} (K - 2k_0) \right] \delta(\omega_d + m\sqrt{gK}) dK. \quad (5.1)$$

The corresponding second-order radar cross section  $\sigma_{2_{fixed}}$  for this case was also derived in [75] as

$$\begin{aligned} \sigma_{2_{fixed}}(\omega_d) = & 2^6 \pi^2 k_0^4 \sum_{m_1=\pm 1} \sum_{m_2=\pm 1} \int_0^\infty \int_{-\pi}^\pi S_1(m_1 \vec{K}_1) S_1(m_2 \vec{K}_2) |\Gamma_{P_m}|^2 K_1 \\ & \cdot \delta(\omega_d + m_1 \sqrt{gK_1} + m_2 \sqrt{gK_2}) d\theta_{\vec{K}_1} dK_1. \end{aligned} \quad (5.2)$$

## 5.3 Platform Motion Compensation Method

For the first-order radar cross section model (4.20), where the sampling function dominates the integral in (4.20), the range of  $K$  in the main lobe of the squared sampling function is extremely small. For such a narrow range of  $K$ , the squared values of the Bessel functions vary only slightly (see Fig. 5.1). Thus, it is assumed here that  $K$  in the arguments of the Bessel functions is constant and is set to a representative value of  $2k_0$ , the wavenumber of the first-order Bragg wave. Then, the Bessel function summation can be removed from the integral and (4.20) may be written as

$$\begin{aligned} \sigma_{1_{floating}}(\omega_d) = & \sum_{n_1=-\infty}^\infty J_{n_1}^2(z_1) \sum_{n_2=-\infty}^\infty J_{n_2}^2(z_2) \\ & \cdot 2^3 \pi k_0^2 \Delta \rho \sum_{m=\pm 1} \int_K K^2 S_1(m\vec{K}) \text{Sa}^2 \left[ \frac{\Delta \rho}{2} (K - 2k_0) \right] \\ & \cdot \delta(\omega_d + m\sqrt{gK} + n_1 \omega_{p1} + n_2 \omega_{p2}) dK \end{aligned} \quad (5.3)$$

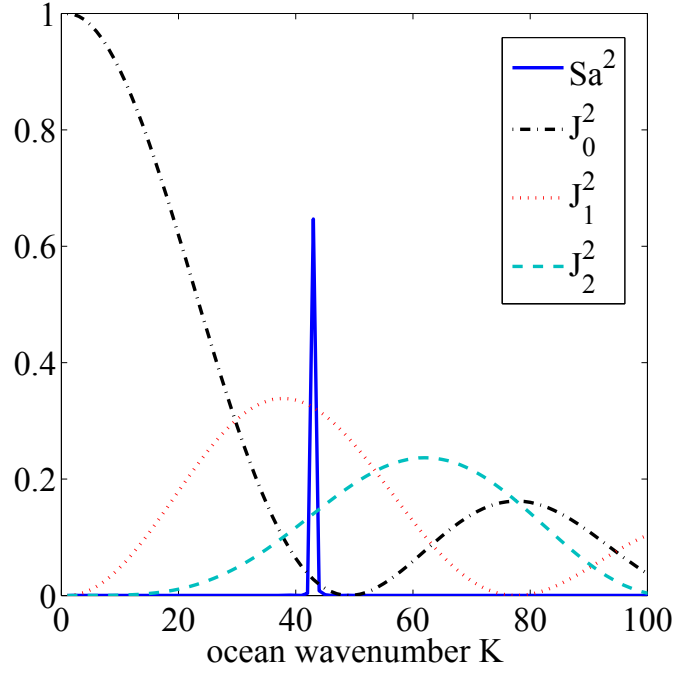


Fig. 5.1 The squared values of sampling function and the Bessel functions with respect to  $K$ . The radar operating frequency is 10 MHz, the platform motion amplitude is 5 m, and the motion direction is the same with the radar look direction.

where  $z_1 = 2a_{x1}k_0 \cos(\theta_K - \theta_{p_x})$  and  $z_2 = 2a_{x2}k_0 \cos(\theta_K - \theta_{p_x})$ . At this stage, it is helpful to define the total radar cross section including the first- and second-order radar cross sections as

$$\sigma_{fixed}(t) = \sigma_{1_{fixed}}(t) + \sigma_{2_{fixed}}(t) \quad (5.4)$$

and

$$\sigma_{floating}(t) = \sigma_{1_{floating}}(t) + \sigma_{2_{floating}}(t). \quad (5.5)$$

By comparing (5.3) and (4.21) with (5.1) and (5.2), respectively, it may be readily determined that the relationship between the radar ocean surface cross section involving a fixed antenna and that for an antenna on a floating platform may be expressed as

$$\sigma_{floating}(\omega_d) = \sum_{n_1=-\infty}^{\infty} J_{n_1}^2(z_1) \sum_{n_2=-\infty}^{\infty} J_{n_2}^2(z_2) \sigma_{fixed}(\omega_d + n_1\omega_{p1} + n_2\omega_{p2}). \quad (5.6)$$

Taking an inverse Fourier transform of (5.6), the relationship may be written in the time domain as

$$\sigma_{floating}(t) = \sigma_{fixed}(t) \cdot \sum_{n_1=-\infty}^{\infty} J_{n_1}^2(z_1) \sum_{n_2=-\infty}^{\infty} J_{n_2}^2(z_2) e^{-j(n_1\omega_{p1} + n_2\omega_{p2})t}. \quad (5.7)$$

Since  $J_n^2(z) = J_{-n}^2(z)$ , (5.7) reduces to

$$\sigma_{floating}(t) = \sigma_{fixed}(t) \cdot \sum_{n_1=-\infty}^{\infty} J_{n_1}^2(z_1) \sum_{n_2=-\infty}^{\infty} J_{n_2}^2(z_2) \cos(n_1\omega_{p1} + n_2\omega_{p2})t. \quad (5.8)$$

Also, the relationship can be extended to the case of a multi-frequency platform motion model. At this point, the transfer function in the time domain  $h(t)$  is defined as

$$h(t) = \sum_{n_1=-\infty}^{\infty} J_{n_1}^2(z_1) \sum_{n_2=-\infty}^{\infty} J_{n_2}^2(z_2) \cdot \cos(n_1\omega_{p1} + n_2\omega_{p2})t. \quad (5.9)$$

Based on the convolution theorem, (5.8) may then be written in the frequency domain as [76], [77]

$$\sigma_{floating}(\omega_d) = \sigma_{fixed}(\omega_d) \otimes H(\omega_d) \quad (5.10)$$

where  $\otimes$  is the linear convolution operation, and  $H(\omega_d)$  represents the Fourier transform of  $h(t)$ .  $H(\omega_d)$  is an array of  $n$  elements, expressed as  $H(\omega_d) = [h_0, h_1, \dots, h_{n-1}]$ , which depends on the floating platform parameters. Thus, if the parameters of the floating platform motion are known, the radar cross section  $\sigma_{fixed}(\omega_d)$  can be recovered through deconvolving the radar cross section  $\sigma_{floating}(\omega_d)$  with  $H(\omega_d)$ .

It should be noted that the models shown above are developed for the monostatic geometry (both the transmitter and the receiver are on the same platform). The relationship (5.10) can also be applied to bistatic radar by modifying the modulation indices in (5.9). For the bistatic case of a fixed receiver and an transmitter on a floating platform, the modulation indices  $z_1 = a_{x1}k_0[\cos(\theta_K - \theta_{px}) + \tan\phi_0 \sin(\theta_K - \theta_{px})]$  and  $z_2 = a_{x2}k_0[\cos(\theta_K - \theta_{px}) + \tan\phi_0 \sin(\theta_K - \theta_{px})]$ . In addition, (5.10) can also be easily

extended for a multi-frequency platform motion model by extending the two frequency components in (5.9) to multiple frequency components.

## 5.4 Deconvolution Techniques

A variety of deconvolution techniques have been developed for different applications. For the problem at hand, four deconvolution techniques are described.

### 5.4.1 Division in the Time Domain

Based on the convolution theorem, deconvolution in the frequency domain can be converted to division in the time domain. Therefore, the radar cross section with platform motion compensation may be calculated through the relation

$$\sigma_{fixed}(\omega_d) = \mathcal{F}\{\mathcal{F}^{-1}\{\sigma_{floating}(\omega_d)\}/h(t)\}. \quad (5.11)$$

For the ideal case of no noise or error in both  $\sigma_{fixed}$  and  $\sigma_{floating}$ , (5.11) is stable, and the method can work successfully. However, for practical systems where there are both noise and error in the data, it is possible that for a certain  $t$ ,  $h(t)$  could approach zero, but  $\sigma_{floating}$  is not relatively small due to the presence of the noise and error. This may cause  $\sigma_{fixed}$  to be an irregularly large number and thereby cause instability in the computation of  $\sigma_{fixed}$ . This represents an ill-posed problem in deconvolution [78].

### 5.4.2 Transformation Matrix

A method of performing a deconvolution by matrix multiplication is introduced. Through the relationship in (5.10),  $\sigma_{floating}(\omega_d)$  and  $\sigma_{fixed}(\omega_d)$  can also be cast in terms of a transformation matrix  $H_{matrix}$  [79] as

$$\sigma_{floating}(\omega_d) = \mathbf{H}_{matrix}\sigma_{fixed}(\omega_d) \quad (5.12)$$

with

$$\mathbf{H}_{matrix} = \begin{bmatrix} h_0 & 0 & 0 & \cdots & 0 & 0 \\ h_1 & h_0 & 0 & 0 & \cdots & 0 \\ \cdots & h_1 & h_0 & 0 & \cdots & 0 \\ h_{n-1} & \cdots & h_1 & h_0 & 0 & \vdots \\ 0 & h_{n-1} & \cdots & h_1 & h_0 & \ddots \\ \vdots & \ddots & \ddots & \ddots & \ddots & \ddots \end{bmatrix}. \quad (5.13)$$

Thus, the deconvolution procedure can be achieved by calculating the inverse matrix  $\mathbf{H}_{matrix}^{-1}$  and multiplying it with the convolved data. The procedure may be written as

$$\sigma_{fixed}(\omega_d) = \mathbf{H}_{matrix}^{-1} \sigma_{floating}(\omega_d), \quad (5.14)$$

and the deconvolution problem is simplified to a matrix inversion problem. However, the ill-posedness still exists in the inversion process, and, therefore, small changes in the  $\sigma_{floating}(\omega_d)$  may cause severe distortion in the  $\sigma_{fixed}(\omega_d)$  because the matrix  $\mathbf{H}_{matrix}$  has a number of small eigenvalues. Here, Von Neumann and Goldstine's P condition number (see, for example, [80]) is introduced as

$$P(\mathbf{H}_{matrix}) = \left| \frac{\lambda_{max}}{\lambda_{min}} \right| \quad (5.15)$$

where  $\lambda_{max}$  and  $\lambda_{min}$ , respectively represent the eigenvalues of  $\mathbf{H}_{matrix}$  of maximum and minimum magnitude. The condition number is an indicator of the "health condition" of a matrix. When  $P(\mathbf{H}_{matrix}) \sim 1$ ,  $\mathbf{H}_{matrix}$  is well-conditioned. When  $P(\mathbf{H}_{matrix}) \gg 1$ ,  $\mathbf{H}_{matrix}$  has at least one small eigenvalue  $\lambda_{min}$  causing the P condition number to be large, and  $\mathbf{H}_{matrix}$  to be ill-conditioned. The worse the condition number of the matrix, the greater the value of P. In our study, an ill-conditioned  $\mathbf{H}_{matrix}$  usually appears when the amplitude of the platform motion is large or the radar operating frequency is high, which results in an increase in the modulation indices.

### 5.4.3 Tikhonov Regularization

Tikhonov regularization (see, for example, [81]), which is widely used to solve ill-posed inverse problems, is introduced by using a transformation matrix as discussed below.

In this study, an assumption of  $K = 2k_0$  in the argument of Bessel functions is made at the beginning of Section 5.3. This assumption may cause errors in the inversion process. If the errors and noise are represented as a matrix  $\mathbf{E}$ , (5.12) may be written as

$$\sigma_{floating}(\omega_d) = \mathbf{H}_{matrix} \sigma_{fixed}(\omega_d) + \mathbf{E}. \quad (5.16)$$

In order to obtain the vector  $\sigma_{fixed}(\omega_d)$ , an error minimization criterion is formulated as

$$\min_{\sigma_{fixed}} \{ \|\mathbf{H}_{matrix} \sigma_{fixed} - \sigma_{floating}\|^2 + \gamma^2 \|\sigma_{fixed}\|^2 \} \quad (5.17)$$

where  $\|\cdot\|$  indicates the 2-norm of a vector.  $\gamma$  is a regularization parameter determined by the noise and errors, which may be estimated by [82]

$$\gamma = \frac{\|\mathbf{H}_{matrix} \sigma_{fixed} - \sigma_{floating}\|^2}{\|\mathbf{I} \sigma_{fixed}\|^2}. \quad (5.18)$$

Then, the estimate for  $\sigma_{fixed}$  is given by

$$\sigma_{fixed} = (\mathbf{H}_{matrix}^T \mathbf{H}_{matrix} + \gamma \mathbf{I})^{-1} \mathbf{H}_{matrix}^T \sigma_{floating}. \quad (5.19)$$

A higher level of noise or errors will require a larger value of  $\gamma$ . The matrix  $\mathbf{I}$  is an identity matrix. If a second-order differential matrix is used to replace the matrix  $\mathbf{I}$ , (5.19) reduces to the least-squares solution. The main idea of Tikhonov regularization is to add a small positive number to the diagonal elements of the transformation matrix to stabilize the system in the inversion process. It is shown in [83] that compared to the matrix  $\mathbf{H}_{matrix}^T \mathbf{H}_{matrix}$ , the magnitude of the smallest eigenvalues of the new transformation matrix  $\mathbf{H}_{matrix}^T \mathbf{H}_{matrix} + \gamma \mathbf{I}$  in (5.19) is increased by finite values of  $\gamma$ . This results in a

decrease in  $P$ , an improvement in the “health condition” of the transformation matrix and the stabilization of the solution.

#### 5.4.4 Iterative Tikhonov Regularization

It is also shown in [83] that the Tikhonov regularization or least-squares method is based on the smoothness of the solution. If the Doppler spectrum  $\sigma_{floating}$  has a sharp low frequency cutoff, this method has limitations. Finally, as in [81], an iterative method is proposed for slow solution convergence by

$$\sigma_{fixed}^{(i+1)} = (\mathbf{H}_{matrix}^T \mathbf{H}_{matrix} + \gamma \mathbf{I})^{-1} \cdot (\mathbf{H}_{matrix}^T \sigma_{floating} + \gamma \sigma_{fixed}^{(i)}) \quad (5.20)$$

where  $\sigma_{fixed}^{(1)}$  is calculated from (5.19). Usually, the larger the number of iterations, the better the solution will be. Typically, 4 or 5 iterations are used in our study. The performance improvement is negligible after 10 iterations.

### 5.5 Radar Cross Sections with External Noise

To date, there is little appropriate existing field data dedicated to the case of an antenna on a floating platform. In order to better mimic experimental data collected from the ocean surface, a combined sea clutter and external noise radar cross section model developed by Gill and Walsh [84] was used to undertake a simulation for a fully developed wind sea and to examine these motion compensation methods.

In the HF band, the external noise may be characterized as a white Gaussian zero-mean process [85]. For HFSWR, it is shown in [86] that the first-order sea echo is a Gaussian process, consisting of linear operations on the presumed stationary Gaussian ocean surface. Additionally, by the central limit theorem, the second-order ocean wave scattered signal may also be treated as a Gaussian process [86]. For such a stationary

Gaussian process, the time-domain form of the signal may be written as [87], [84]

$$f(t) = \int_B e^{j\omega t} e^{j\varepsilon(\omega)} \sqrt{F_s(\omega)} \frac{d\omega}{2\pi} \quad (5.21)$$

where  $B$  represents the limited bandwidth of the system, i.e.  $-\frac{\omega}{2} \leq B \leq \frac{\omega}{2}$ .  $F_s(\omega)$  is the power spectral density of  $f(t)$  and  $\varepsilon(\omega)$  is a random phase variable whose values lie between 0 and  $2\pi$ . However, in our study, the radar received signal is frequency-modulated by the platform motion [68]. Frequency modulation is a nonlinear process. Thus, (5.21) is no longer suitable for addressing the radar cross sections for this case.

Combining (5.8) with frequency modulation results found in Chapter 7 of [71], it may be deduced that

$$f_{floating}(t) = f_{fixed}(t) \cdot e^{j(z_1 \cos \omega_{p1}t + z_2 \cos \omega_{p2}t)} \quad (5.22)$$

where  $f_{floating}(t)$  and  $f_{fixed}(t)$  represent the received radar signals in the case of an antenna on a floating platform and on a fixed platform, respectively. Thus, if the signal  $f(t)$  is frequency-modulated, the signal after modulation in the time domain may be expressed as

$$g(t) = e^{jX} f(t) = e^{jX} \int_B e^{j\omega t} e^{j\varepsilon(\omega)} \sqrt{F_s(\omega)} \frac{d\omega}{2\pi} \quad (5.23)$$

where  $X = z_1 \cos \omega_{p1}t + z_2 \cos \omega_{p2}t$ .

It is worth noting here that the external white noise will also be modulated by the platform motion due to the limited system bandwidth. Substituting the clutter and noise power spectral densities into model (5.23), obtaining the frequency-modulated clutter signal  $c(t)$  and noise signal  $n(t)$ , respectively, and adding them together, the combined signal may be expressed as

$$s(t) = c(t) + n(t). \quad (5.24)$$

Following the analysis in [84], the Doppler spectrum may be estimated by

$$P(\omega) = \frac{1}{\Delta t} \left| \int_{t_1}^{t_2} s(t) e^{-j\omega t} dt \right|^2 \quad (5.25)$$

where the time series length from  $t_1$  to  $t_2$  is specified as  $\Delta t$ .

Fig. 5.2 shows an example of a combined sea clutter and external noise Doppler spectrum for an antenna on a floating platform. The detailed radar system simulation parameters used here are also found in [84] and given in Table 5.1. The SNR in this chapter refers to the ratio of the sea clutter power spectral density for the largest Bragg peak to the noise power spectral density. The platform motion simulation parameters are taken from Table 2.1 for a wind speed of 10.3 m/s. From Fig. 5.2, it is clearly seen that the noise floor is approximately -160 dB, which means the Doppler spectra information below -160 dB is contaminated and covered by the white external noise.

Table 5.1 Radar system parameters [84]

Operating frequency	10 MHz
Bistatic angle	30°
Pulse width	13.3 $\mu s$
Pulse repetition period	333 $\mu s$
Peak power	16 kW
Transmitter gain	1.585
Half-power beam width	0.07029 rad
Receive array gain	65.76
Distance from patch to transmitter	50 km
Distance from patch to receiver	50 km
Rough spherical earth attenuation	0.312
SNR	60 dB

## 5.6 Examples of Motion Compensation Results

Examples of motion compensation results under different sea states, developed using the deconvolution techniques found in Section 5.4, are shown in Figs. 5.3–5.8. The Doppler spectra for an antenna on a floating platform, and incorporating external white

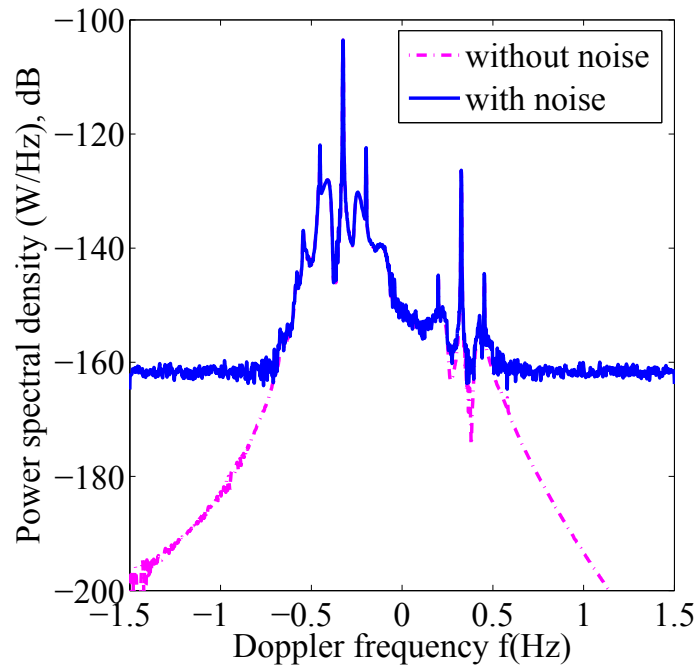


Fig. 5.2 A combined sea clutter and external noise Doppler spectrum. The radar operating frequency is 10 MHz with SNR = 60 dB.

noise, are simulated using the technique illustrated in Section 5.5. Spectra obtained in this manner are referred to as ‘before compensation’ in the following figures. Then, the platform motion compensation method is used on the simulated spectra to eliminate the effect of the platform motion and to obtain the compensation result, labeled as ‘after compensation’. Finally, the corresponding Doppler spectrum for a fixed antenna with external white noise (under the same simulation environment as for the floating platform case) is simulated and labeled as ‘fixed’ in these figures. By comparing the ‘fixed’ with the ‘after compensation’, the performance of the platform motion compensation method can be evaluated.

Fig. 5.3 shows an example of platform motion compensation results for the cases of a single-frequency platform motion model. The amplitude and radian frequency data of the platform motion in Fig. 5.3 are taken from Table 2.1, and these parameters are given for a sea state of 5 on the Beaufort scale with a wind speed of 10.3 m/s. The radar operating frequency is taken to be 15 MHz, and the SNR is about 65 dB. In this case, the condition

number  $P$  is 1.12, which means that the transformation matrix is well conditioned. For such a well-conditioned transformation matrix, it is mentioned in Section 5.4 that all four deconvolution techniques can be used to obtain the same compensation results. Here in Fig. 5.3, deconvolution method B of Section 5.4 is used.

As previously noted, the platform motion may cause additional peaks symmetrically distributed in the Doppler spectrum [50]. In Fig. 5.3 (a), some of the first-order motion-induced peaks are located in the region of the second-order Doppler spectrum. If the effect of the platform motion is ignored in interpreting the Doppler spectra, this will cause an overestimation of the significant wave height. This effect has also been observed in experimental data [9]. In addition, it may be clearly observed from Fig. 5.3 (b) that, due to the floating platform motion, a fraction of the energy is transferred from the Bragg peaks to the motion-induced peaks. This phenomenon has also been discussed in [66]. It may be observed from Fig. 5.3 that through platform motion compensation, the motion-induced peaks are completely removed from the radar Doppler spectra. Additionally, the energies of the Bragg peaks are simultaneously recovered, though this phenomenon is not obvious in Fig. 5.3 due to the small magnitude of the modulation index (which is related to the amplitude of platform motion in this study).

In [88], a floating platform with a mooring system was modeled and simulated. The time series of the surge motion were given for significant wave heights of 4 m and 8 m. Based on the surge motion curve (see [88]) for the  $H_s = 8$  m case, the platform motion parameters of the two main frequency components can be obtained as  $a_1 = 2$  m,  $\omega_{p1} = 0.05$  rad/s,  $a_2 = 0.9$  m and  $\omega_{p2} = 0.63$  rad/s. Taking into account the saturation limit on the significant wave height ( $H_{sat} = 2/k_0$ ) given in [72], the radar operating frequency is taken as 10 MHz. Based on the parameters shown above, the condition number  $P$  is calculated to be 1.03, which means the transformation matrix is well-conditioned. Fig. 5.4 shows the platform motion compensation results using these simulation parameters and deconvolution method B, resulting in an SNR of around 56 dB.

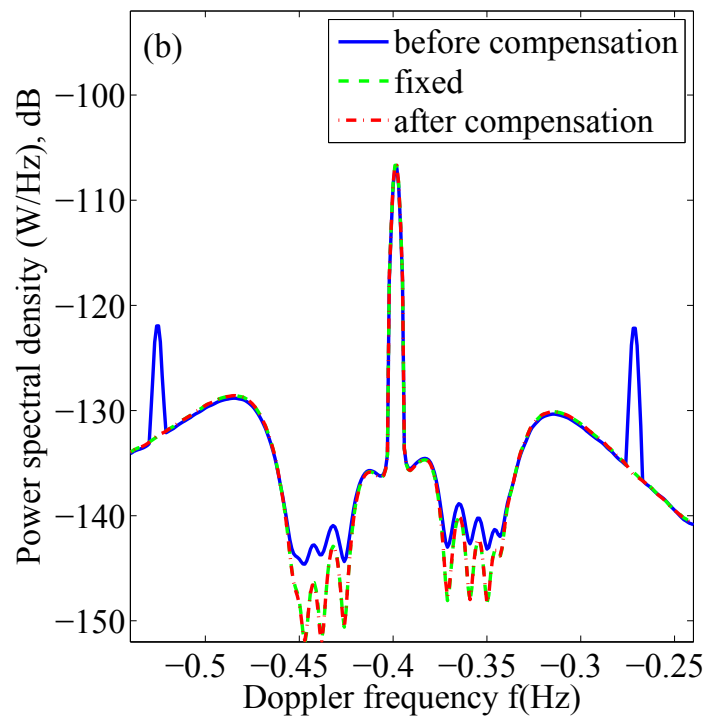
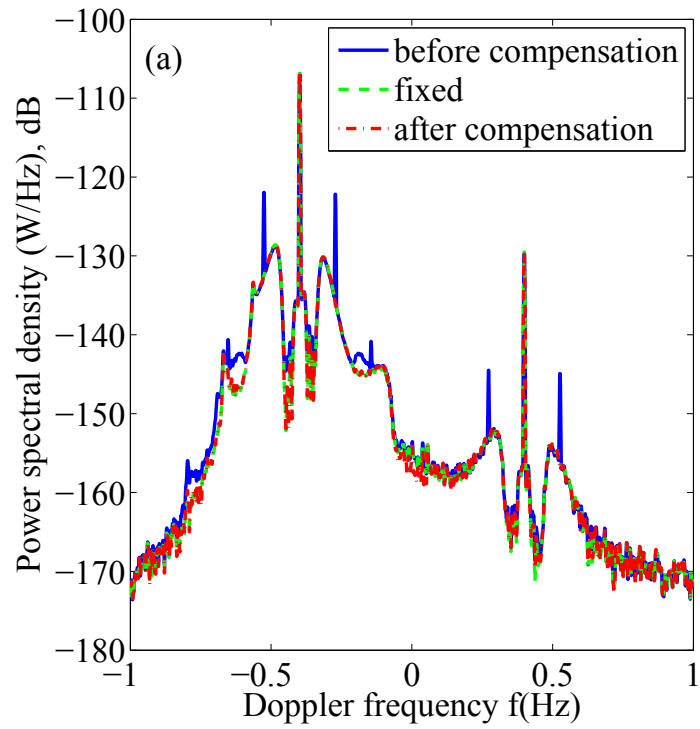


Fig. 5.3 An example of the platform motion compensation results for a single-frequency motion model having an amplitude of 1.228 m and a radian frequency of 0.127 Hz. (a) Comparison of the Doppler spectrum before compensation with that after compensation (b) A zoomed-in view of (a).

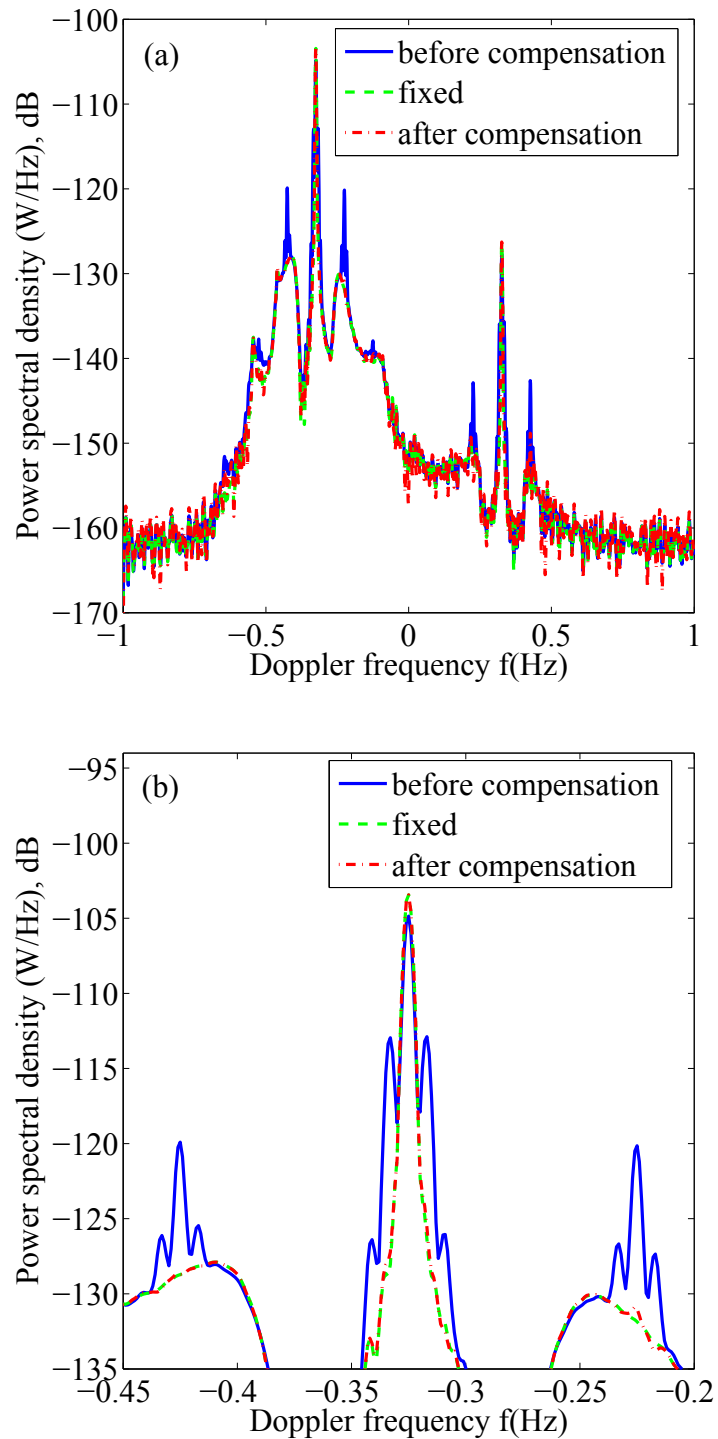


Fig. 5.4 An example of the platform motion compensation results for a dual-frequency motion model having amplitudes of 2 m and 0.9 m, and radian frequencies of 0.05 rad/s and 0.63 rad/s, respectively. (a) Comparison of the Doppler spectrum before compensation with that after compensation (b) A zoomed-in view of (a).

Through a number of simulated data tests, it is found that when  $P$  is less than 5, the matrix can be assumed to be well-conditioned. In this case, the deconvolution operation can be achieved by division in the time domain (method A) or the direct inversion of a transformation matrix (method B). When  $P$  is greater than 5, the compensation results may be acceptable, but are not ideal as compared to those when  $P$  is less than 5. From the experience in this study, the compensation results should be discarded for  $P > 10$ . In the case of  $P > 5$ , Tikhonov regularization (method C) or an iterative Tikhonov regularization (method D) is adopted to solve the ill-posed deconvolution problem.

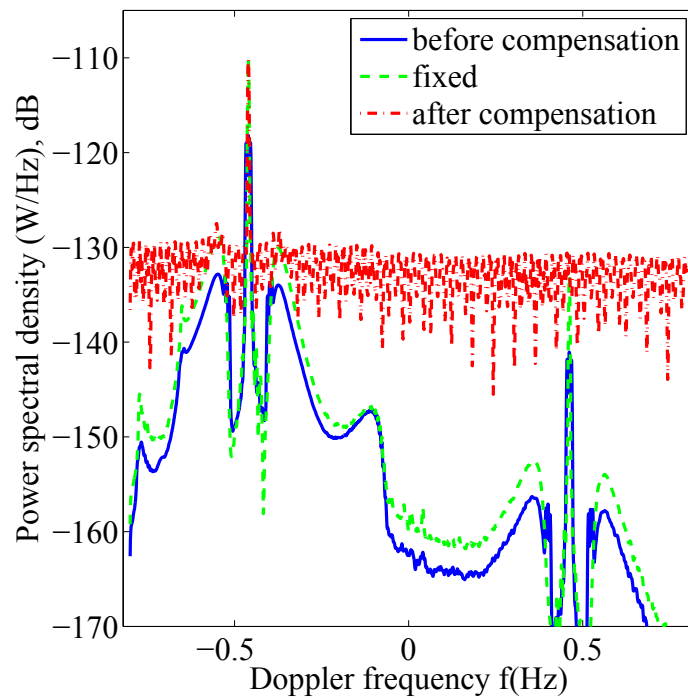


Fig. 5.5 An example of the platform motion compensation results for a dual-frequency motion model having amplitudes of 5.5 m and 0.4 m, and radian frequencies of 0.02 rad/s and 0.38 rad/s, respectively. This result is for an ill-conditioned transformation matrix by using the deconvolution technique A or B in Section 5.4.

The motion model of another floating platform with a mooring system was established and tested in [70]. The time series of the surge motion were recorded under a combined swell and wind sea condition. The significant wave height was 2.05 m and its peak wave period was 6.7 s. From [70], the platform motion data of the two main

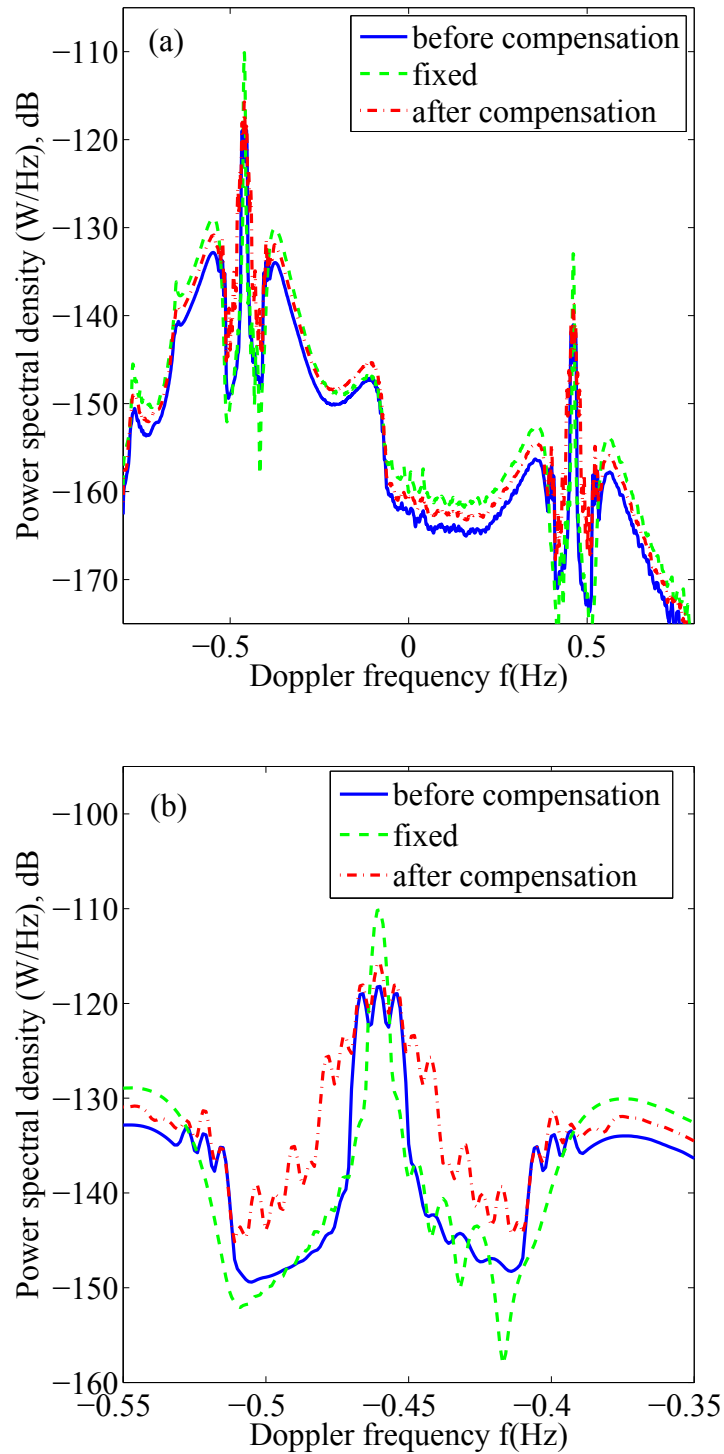


Fig. 5.6 An example of the platform motion compensation results for a dual-frequency motion model having amplitudes of 5.5 m and 0.4 m, and radian frequencies of 0.02 rad/s and 0.38 rad/s, respectively. This result is for an ill-conditioned transformation matrix by using the deconvolution technique of Tikhonov regularization. (a) Comparison of the Doppler spectrum before compensation with that after compensation (b) A zoomed-in view of (a).

frequency components were obtained as  $a_1 = 5.5$  m,  $\omega_{p1} = 0.02$  rad/s,  $a_2 = 0.4$  m and  $\omega_{p2} = 0.38$  rad/s. The radar operating frequency is taken as 20 MHz. In this case,  $P$  is calculated to be 3116, indicating that the transformation matrix is ill conditioned. By using these simulation parameters as an example, comparisons using different deconvolution techniques are made and shown in Figs. 5.5 to 5.7. The SNR in these figures is taken to be approximately 70 dB. It should be noted that it is meaningless to compare the amplitudes and radian frequencies of the platform motion for different floating platforms, even though they may be subject to the same environmental conditions. This is because the amplitudes and radian frequencies of the platform motion are determined by many factors, such as environmental conditions, and the size, weight and structure of the floating platform and its mooring system. It may be clearly observed from Figs. 5.5 to 5.7 that, due to the floating platform motion, a fraction of the energy is transferred from the Bragg peaks to the motion-induced peaks. This phenomenon has also been discussed in Chapter 4.

Fig. 5.5 shows the compensation results obtained by directly using “division in the time domain” (method A) or direct inversion of the transformation matrix (method B). It can be seen from the figure that the compensation results are poor for the case of an ill conditioned transformation matrix. The compensation results obtained using Tikhonov regularization or least-squares deconvolution techniques are shown in Fig. 5.6. The ill posed problem is partially solved, and a better compensation result is obtained. However, the compensation results in the region of the Bragg peak are unsatisfactory. The magnitude of the Bragg peak is not completely recovered and the region of the Bragg peak is still broadened. This is because there is a sharp low frequency cutoff at the boundaries of the Bragg peaks region where it meets the second-order region. As mentioned before, a smooth solution provided by Tikhonov regularization is not realistic for the case of a sharp cutoff, although the compensation results in the rest of the Doppler regions show a good performance. Considering these issues, Fig. 5.7 gives the motion compensation result obtained using iterative Tikhonov regularization. It may

be observed from Fig. 5.7 that the Doppler spectrum with antenna motion has been well compensated and recovered as compared to the corresponding simulated fixed Doppler spectrum. It can be observed that the platform motion compensation has completely removed motion-induced peaks from the radar Doppler spectra and the energies of the Bragg peaks have been recovered.

The motion compensation technique derived in Section 5.3 is for both the first-order and the second-order radar cross sections. The technique has the same impact on the second-order radar cross section as it does on the first-order. For example, there are additional second-order motion-induced peaks appearing in the Doppler spectrum, and a fraction of the energy is transferred from the second-order peaks to these motion-induced peaks. However, as discussed in [18] and [55], the motion-induced second-order peaks appearing in the spectrum are seen to have significantly less energy than those in the first-order case. Thus, the second-order motion-induced peaks are not obvious in the spectrum (see the peaks near -0.67 Hz labeled by the blue solid line in Fig. 5.7 (a)). From Fig. 5.7 (a), it is clear that the energies of the second-order peaks are also recovered through this compensation method.

The model of a floating platform with a mooring system was next considered for a storm condition associated with sea state 11 [89]. Time series of the surge motion were recorded under environmental conditions associated with a 100 year storm. For this extreme sea state, the significant wave height was 14 m and its peak wave period was 15.8 s. Based on the surge motion curve shown in [89], the platform motion data involving the two main frequency components are taken to be  $a_1 = 10$  m,  $\omega_{p1} = 0.08$  rad/s,  $a_2 = 5$  m and  $\omega_{p2} = 0.63$  rad/s. The radar operating frequency is taken to be 5 MHz and the SNR decreases to 40 dB. In this case,  $P$  is calculated to be 36876, which shows the transformation matrix defines a greatly ill-posed problem. Based on these simulation data, Fig. 5.8 shows the platform motion compensation results using the iterative Tikhonov regularization deconvolution method. In this extreme case, the trend of the compensation result is generally acceptable, and the curve in the Bragg peak

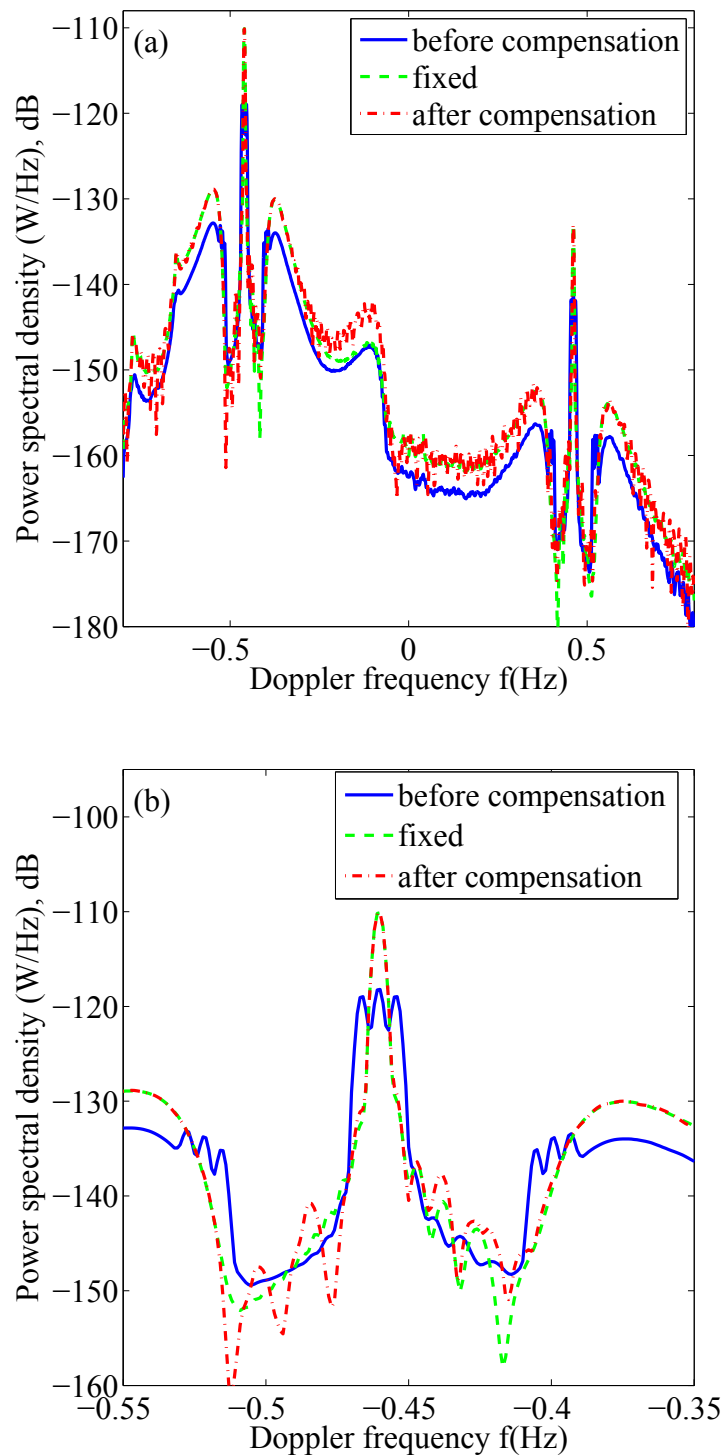
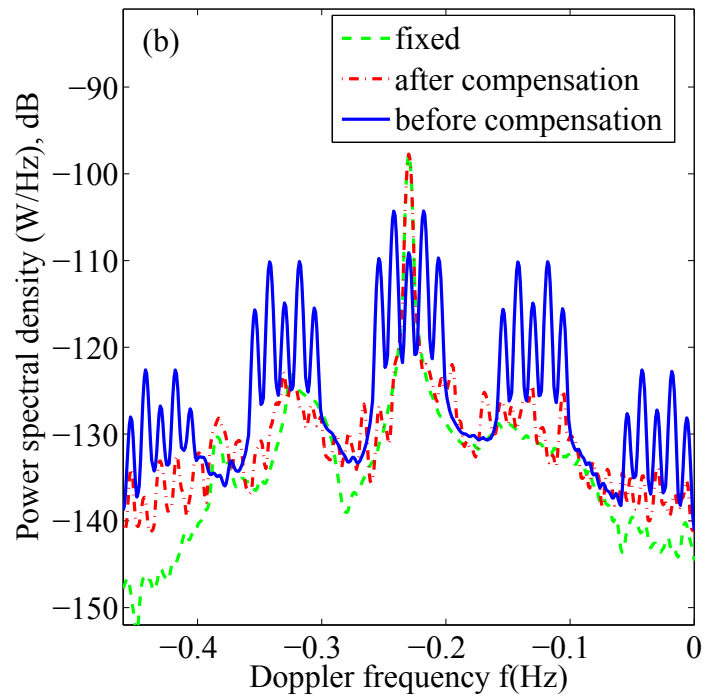
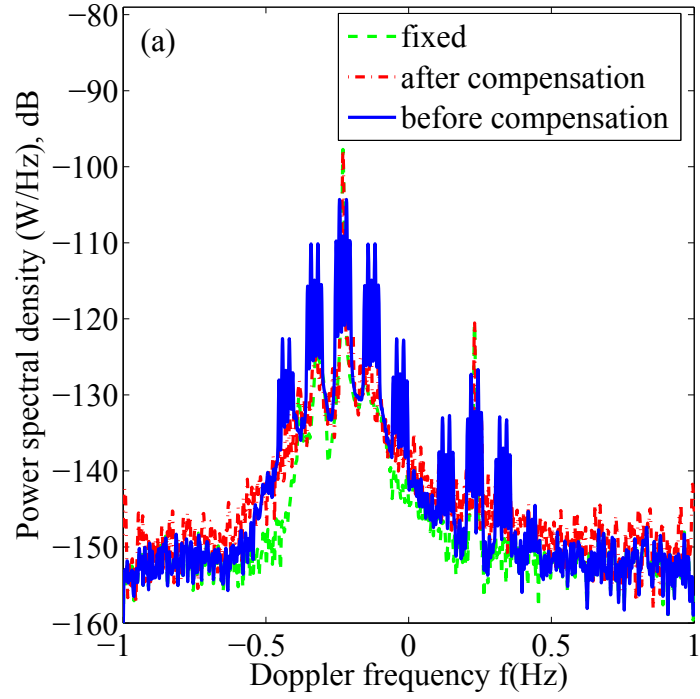


Fig. 5.7 An example of the platform motion compensation results for a dual-frequency motion model having amplitudes of 5.5 m and 0.4 m, and radian frequencies of 0.02 rad/s and 0.38 rad/s, respectively. This result is for an ill-conditioned transformation matrix by using the deconvolution technique D in Section 5.4. (a) Comparison of the Doppler spectrum before compensation with that after compensation (b) A zoomed-in view of (a).



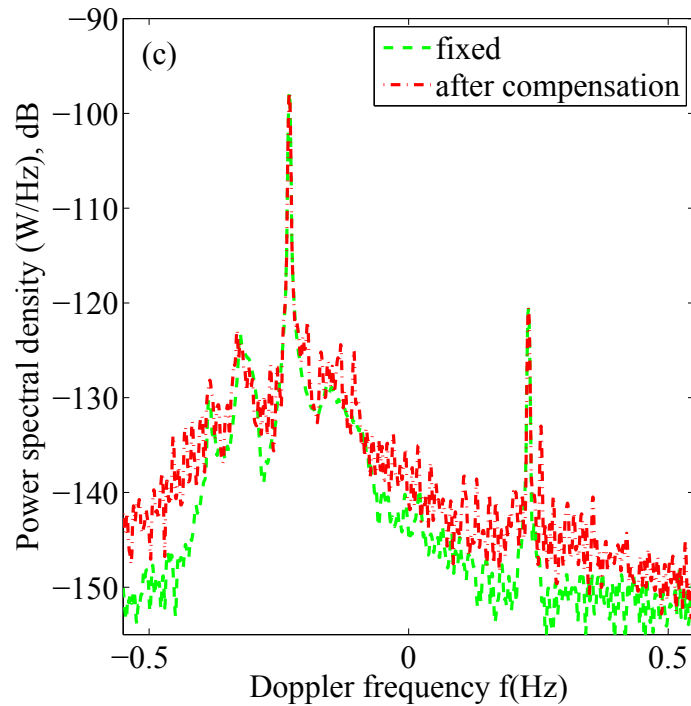


Fig. 5.8 An example of the platform motion compensation results for a dual-frequency motion model having amplitudes of 10 m and 5 m, and radian frequencies of 0.08 rad/s and 0.63 rad/s, respectively. (a) Comparison of the Doppler spectrum before compensation with that after compensation; (b) A zoomed-in view of (a); (c) Comparison of the compensation result with the Doppler spectrum for a fixed antenna.

region is well-compensated. However, for the low-energy peaks, like the second-order electromagnetic peaks, the compensation performance is not ideal.

To quantitatively show the performance of the motion compensation method, Table 5.2 illustrates the root-mean-square differences between the “after compensation” and “fixed” cases in Figs. 5.3- 5.8. As observed in the table, the worst performance is seen in Fig. 5.5, where an ill-posed problem occurs. By comparing the values of root-mean-square difference for Fig. 5.6 with that for Fig. 5.7, the performance of the motion compensation method is found to be improved by using an iterative Tikhonov regularization deconvolution technique. Through these motion compensation results, the motion compensation method proposed in this thesis is well examined and shows a satisfactory performance.

Table 5.2 Root-mean-square differences between the “after compensation” and “fixed” cases in Figs. 5.3- 5.8

Figures	Root-mean-square differences (dB)
Fig. 5.3	0.4163
Fig. 5.4	0.8402
Fig. 5.5	22.8646
Fig. 5.6	4.4696
Fig. 5.7	2.2171
Fig. 5.8	5.0757

It is worth noting that when calculating  $H(\omega_d)$  based on the information of  $h(t)$ , an integer number of periods should be used in the Fourier transform in order to avoid the spectral leakage problem and improve the performance of the deconvolution.

## 5.7 Chapter Summary

A compensation method has been proposed for the purpose of mitigating the platform motion effects on HFSWR Doppler spectra. The relationship between the HFSWR cross sections of the ocean surface for a fixed antenna and an antenna on a floating platform has been established. Through this relationship, motion compensation can be achieved by deconvolution procedures. The radar cross section incorporating external Gaussian white noise is developed and used to examine the compensation method. In this study, an iterative Tikhonov regularization deconvolution method is suggested for solving the ill-posed deconvolution problem. The compensation results under different sea states and SNRs obtained by using this deconvolution method show a satisfactory performance. This motion compensation method can also be extended for shipborne HFSWR.

Tikhonov regularization and iterative Tikhonov regularization are introduced to solve the problem caused by the ill-conditioned transformation matrix. Of course, in the case of a well-conditioned matrix, Tikhonov regularization and the iterative Tikhonov regularization can still be used. However, in order to minimize numerical uncertainties introduced by the computation software and to reduce the computation time, a simple

deconvolution method (method A or method B discussed in Section 5.4) can be used when the transformation matrix is well-conditioned.

# Chapter 6

## Conclusion

### 6.1 Summary

The objectives of this thesis have been: 1) to establish comprehensive HFSWR cross section models of the ocean surface in order to investigate the effect of antenna motion on the radar Doppler spectrum; and 2) to develop a compensation method to mitigate the platform motion effects that distort the Doppler spectrum such that ocean remote sensing parameters can be accurately extracted.

Based on the work of monostatic radar cross sections for a pulsed source involving an antenna on a floating platform [17] and [18], corresponding bistatic models are firstly developed by using elliptic coordinate transformation and the stationary phase method. The ocean surface is described by a Fourier series with the coefficients being random variables. The second-order radar cross section contains both hydrodynamic and electromagnetic contributions. A new bistatic electromagnetic coupling coefficient is derived, which unlike some earlier versions produces no non-physical singularities in the Doppler spectrum. The effect of the platform motion is found to result in a sum of Bessel functions of the first kind in the final cross section result, varying in order from zero to infinity. It is verified that by imposing the appropriate conditions, the new RCS models

reduce to the stationary bistatic models in [51] or to the monostatic models involving antenna motion in [17], [18].

Assuming a simple model in which the platform motion is caused by the dominant ocean wave, simulations are made to illustrate the motion-induced peaks under different sea states and to compare the bistatic model with the monostatic case. Simulation results show that the locations of the motion-induced peaks are symmetrically distributed in the spectrum and the magnitude decreases with increasing order of the Bessel functions. These motion-induced peaks have less energy in the second-order radar cross section than those in the first-order. In addition, the frequencies of the first-order, second-order and their corresponding motion-induced peaks are closer to zero Doppler frequency in the bistatic case than those in the monostatic case.

Following this work, the first- and second-order bistatic radar cross sections are then extended to investigate the impact of using an FMCW source which is subject to platform motion. Based on previous work in [50] and [55], the derivation begins with the general bistatic electric field in the frequency domain for the case of a floating antenna. Demodulation and range transformation are used to obtain the range information, distinguishing the process from that used for a pulsed radar. After Fourier transforming the autocorrelation function and comparing the result with the radar range equation, the radar cross sections are derived. The newly derived bistatic RCS models for an FMCW source are modulated with a sinusoidal platform motion model and compared with those for a pulsed source. It can be found that for the same radar operating parameters, the first-order radar cross section for the FMCW waveform is slightly lower than that for a pulsed source. The second-order radar cross section for the FMCW waveform reduces to that of the pulsed waveform when the scattering patch width approaches infinity. As expected, the sidelobe level is found to be reduced with increasing magnitude of the range bin. When the range bin approaches infinity, the first-order radar cross section for an FMCW waveform approaches a rectangular function and the second-order radar cross section model for the FMCW waveform reduces to that of the pulsed waveform.

The effect of platform motion on the radar cross sections for an FMCW waveform is investigated for a variety of sea states and operating frequencies, and, in general, is found to be similar to that for a pulsed waveform.

Next, a more complicated platform motion model, rather than the single-frequency sinusoidal function motion model as appears in earlier work, is established based on the investigations of the horizontal motion of a platform with a mooring system. In order to simplify the study, the platform motion model is reduced to a combination of two cosine functions in one direction, respectively representing low frequency motion and wave frequency motion. Monostatic and bistatic radar cross section models incorporating a dual-frequency platform motion model are derived. Then, the platform motion model is extended to include multiple frequencies and both surge and sway directions, and the corresponding radar cross sections are also developed. By comparing the signal modulation theory, such as appears in [71], it is found that the platform motion can be viewed as a modulator of the radar frequencies and the modulation indices are related to the amplitudes of the platform motions. This frequency modulation has a much greater effect on the first-order RCS than it does on the second-order. Simulation results show that a fraction of the energy is transferred from the Bragg peaks to the motion-induced peaks, which may be located in the region of the second-order radar cross section. If the effect of the platform motion is ignored in interpreting the Doppler spectra, these motion-induced peaks may raise the second-order radar cross section. This would result in an overestimation of the significant wave height, an effect which has been observed in experimental data [9]. With a larger amplitude of platform motion, more energy is transferred from the Bragg peaks to the motion-induced peaks, and more motion-induced peaks need to be considered. Simulations also find that the bistatic angle affects both the power of the second-order received Doppler spectra and the modulation level of the platform motion on the radar cross sections.

Finally, a method for mitigating antenna motion effects in HFSWR Doppler spectra developed from ocean backscatter is proposed. Based on the established radar cross sec-

tion models for a fixed antenna and for an antenna on a floating platform, the relationship between these models is developed. Through this relationship, motion compensation can be achieved by deconvolving the radar cross section data with the derived transfer function. Four different deconvolution methods (division in the time domain, transformation matrix, Tikhonov regularization and iterative Tikhonov regularization) are investigated and discussed in this thesis. The ill-posed problem occurs with different platform motion parameters, and the P condition number is used to evaluate the “health condition” of the system. Usually, ill-posedness appears when the amplitude of the platform motion is large or the radar operating frequency is high, both of which would result in an increase in the modulation indices. Tikhonov regularization is widely used to solve ill-posed problems by assuming a solution to be smooth. Iterative Tikhonov regularization is an improved method of Tikhonov regularization. To better mimic experimental data for use in the motion compensation method, the radar cross section model with external noise for an antenna on a floating platform model is developed. The external noise is characterized as a white Gaussian zero-mean process of finite variance. By using the four deconvolution techniques, the compensation results under different sea states and SNRs are shown. Through these compensation results, the compensation method using iterative Tikhonov regularization is seen to provide better performance. It is shown that this process significantly removes the motion-induced peaks and simultaneously recovers the energy of the first- and second-order peaks.

The main contribution of this work is the development of the various bistatic HFSWR cross section models of the ocean surface for the case of an antenna on a floating platform. Firstly, these radar cross section models can provide a theoretical foundation for a better understanding and utilization of HFSWR experimental data to extract accurate oceanic information. Secondly, the analysis of the motion effects on the Doppler spectrum brings valuable insights for future practical investigations to determine the feasibility of using HFSWR on a floating platform and suitable geometries for the deployment of a platform-mounted HFSWR. Finally, the compensation method proposed in this thesis

gives a technique to mitigate the motion effects and recover the Doppler spectrum. While the techniques suggested here show promise for improving ocean parameter estimation from platform-mounted HFSWR, the extent of their utility will only be determined by their future application to field data.

## **6.2 Suggestions for Future Work**

Based on the work presented in this thesis, several remaining problems are briefly discussed here with suggestions for future theoretical and experimental research work.

Firstly, it may be noted that the radar cross section models developed in this thesis are based on several assumptions, for example, a good conducting ocean surface, and small height and small slope of the ocean surface waves. These assumptions considerably simplify the analysis and development of the RCS models. However, in the real world, ocean surface waves may be far more complex. Thus, these assumptions restrict the class of ocean surfaces which HFSWR may be used to observe with the methods of this thesis. In the future, it would be worthwhile to investigate the effect of these assumptions on the RCS models and to develop new models by relaxing these assumptions.

Secondly, to date, there is no existing field data dedicated to the problem of HFSWR operating from a floating platform. It will be important, therefore, to evaluate the RCS models for data obtained under conditions of the motion discussed in this thesis.

Thirdly, it is known that radar experimental data is more complex to analyze because it contains a variety of other information, which are not considered in the RCS models derived in this thesis. For example, currents, swell, internal system noise, non-Gaussian external noise and so on will potentially impact the data and derived results. Thus, the motion compensation method proposed in this thesis may still encounter various problems when applied to experimental data. Simultaneously, this compensation method needs to be examined using field data and further improved so that the method could work effectively under a variety of sea states.

Finally, it is worth noting that the compensation method presented in this thesis is especially proposed for a large floating platform with a mooring system, in which case the horizontal motion of the platform motion is dominant. This motion compensation method can also be extended for shipborne HFSWR. However, for shipborne HFSWR operating under a high sea state, the pitch and roll angles of the ship would also need to be considered in the compensation method. It is expected that, in the future, the pitch and roll angles of the ship will be analyzed and incorporated in the compensation method.

The work presented in this thesis provides a solid theoretical basis for these and other extensions of the analysis of platform-mounted HFSWR. With this work, it is hoped that HF radar, as an ocean remote sensor, will become increasingly mature and successful.

## References

- [1] E. D. R. Shearman, "Radio science and oceanography," *Radio Sci.*, vol. 18, no. 3, pp. 299-320, 1983.
- [2] E. Gill, M. Khandekar, R. Howell, and J. Walsh, "Ocean surface wave measurement using a steerable high frequency narrow beam ground wave radar," *J. Atmos. Ocean. Technol.*, vol. 13, no. 3, pp. 703-713, 1996.
- [3] E. Gill, "The scattering of high frequency electromagnetic radiation from the ocean surface: An analysis based on a bistatic ground wave radar configuration," Ph.D. thesis, Mem. Univ. of Newfoundland, St. John's, Newfoundland, Canada, 1999.
- [4] E. Gill, W. Huang, and J. Walsh, "On the development of a second-order bistatic radar cross section of ocean surface: A high-frequency result for a finite scattering patch," *IEEE J. Oceanic Eng. Special Issue on HF/VHF Sea Surface Radar*, vol. 31, no. 4, pp. 740-750, 2006.
- [5] J. Zhang and E. Gill, "Extraction of ocean wave information from simulated noisy high frequency bistatic radar data," *IEEE J. Oceanic Eng. Special Issue on HF/VHF Sea Surface Radar*, vol. 31, no. 4, pp. 779-796, 2006.
- [6] B. Li and Y. Yuan, "A method for ship target extracting from broadened Bragg lines in bistatic shipborne SWR," in *Proc. 8th International Conference on Signal Processing (ICSP)*, Beijing, 2006.

- [7] W. Huang, E. Gill, X. Wu, and L. Li, "Measurement of sea surface wind direction using bistatic high-frequency radar," *IEEE Trans. Geosci. Remote Sens.*, vol. 50, no. 10, pp. 4117-4122, 2012.
- [8] C. J. Baker and H. D. Griffiths, "Bistatic and multistatic radar sensors for homeland security," in *Advances in sensing with security applications*, Springer Netherlands, pp. 1-22, 2006.
- [9] B. J. Lipa, D. E. Barrick, J. Isaacson, and P. M. Lilleboe, "CODAR wave measurements from a North Sea semisubmersible," *IEEE J. Oceanic Engr.*, vol. 15, no. 2, pp. 119-125, 1990.
- [10] K. W. Gurgel, "Shipborne measurement of surface current fields by HF radar," in *Proc. IEEE Oceans 94 Conf.*, vol. 3, pp. 23-27, 1994.
- [11] J. Xie, Y. Yuan, and Y. Liu, "Experimental analysis of sea clutter in shipborne HFSWR," *IEE Proc., Radar, Sonar Navig.*, vol. 148, no. 2, pp. 67-71, 2001.
- [12] J. El Khoury, R. Guinvarch, A. Bourges, and P. Flament, "An experimentation of a floating antenna for HF surface wave radar," Radiowave Oceanography Workshop (ROW 2009), Split, Croatia, May 2009.
- [13] M. Spillane, R. Crissman, M. Evans, D. Barrick, B. Lipa, and B. Braennstrom, "Results of the codar offshore remote-sensing project," in *Proc. Offshore Technology Conference*, 1986.
- [14] D. E. Barrick, "First-order theory and analysis of MF/HF/VHF scatter from the sea," *IEEE Trans. Antennas Propag.*, vol. 20, no. 1, pp. 2-10, 1972.
- [15] D. Barrick, "Remote sensing of sea state by radar," in *Remote Sensing of the Troposphere*, edited by V. Deft, chap. 12, pp. 1-46, U.S. Govt. Print. Off., Washington, D.C., 1972.

- [16] J. Walsh, "The effect of barge motion on HFSWR ocean clutter," Northern Radar Inc., St. Johns, NL, 2004. (Contract Report Prepared for Raytheon Canada Limited, Waterloo, ON).
- [17] J. Walsh, W. Huang, and E. Gill, "The first-order high frequency radar ocean surface cross section for an antenna on a floating platform," *IEEE Trans. Antennas Propag.*, vol. 58, no. 9, pp. 2994-3003, 2010.
- [18] J. Walsh, W. Huang, and E. Gill, "The second-order high frequency radar ocean surface cross section for an antenna on a floating platform," *IEEE Trans. Antennas Propag.*, vol. 60, no. 10, pp. 4804-4813, 2012.
- [19] J. Walsh, W. Huang, and E. Gill, "The second-order high frequency radar ocean surface foot-scatter cross section for an antenna on a floating platform," *IEEE Trans. Antennas Propag.*, vol. 61, no. 11, pp. 5833-5838, 2013.
- [20] J. El Khoury, R. Guinvarc'h, R. Gillard, and B. Uguen, "Sea-echo doppler spectrum perturbation of the received signals from a floating high-frequency surface wave radar," *IET Radar Sonar Navig.*, vol. 6, no. 3, pp. 165-171, 2012.
- [21] J. El Khoury, R. Gillard, and B. Uguen, "Simulator of high frequency surface wave radar (HFSWR) with offshore receiver," in *Proc. IEEE APS Symposium.*, pp. 3241-3244, 2011.
- [22] J. Xie, M. Sun, and Z. Ji, "First-order ocean surface cross-section for shipborne HFSWR," *Electron. Lett.*, vol. 49, no. 16, pp. 1025-1026, 2013.
- [23] M. Sun, J. Xie, Z. Ji, and W. Cai, "Second-order ocean surface cross section for shipborne HFSWR," *IEEE Antennas Wireless Propag. Lett.*, vol. 14, pp. 823-826, 2015.

- [24] M. Sun, J. Xie, Z. Ji, and W. Cai, "Remote sensing of ocean surface wind direction with shipborne high frequency surface wave radar," in *Proc. IEEE Radar Conference (RadarCon)*, pp. 0039-0044, 2015.
- [25] W. Huang, E. Gill, S Wu, B. Wen, Z. Yang, and J. Hou, "Measuring surface wind direction by monostatic HF ground-wave radar at the Eastern China Sea," *IEEE J. Ocean. Eng.*, vol. 29, no. 4, pp. 1032-1037, 2004.
- [26] Z. Wang, J. Xie, Z. Ji, and T. Quan, "Remote sensing of surface currents with single shipborne high-frequency surface wave radar," *Ocean Dynamics*, vol. 66, no. 1, pp. 27-39, 2015.
- [27] G. Chang, M. Li, J. Xie, L. Zhang, C. Yu, and Y. Ji, "Ocean Surface Current Measurement Using Shipborne HF Radar: Model and Analysis," *IEEE J. Ocean. Eng.*, vol. 41, no. 4, pp. 970-981, 2016.
- [28] J. Xie, Z. Wang, Z. Ji, and T. Quan, "High-resolution ocean clutter spectrum estimation for shipborne HFSWR using sparse-representation-based MUSIC," *IEEE J. Ocean. Eng.*, vol. 40, no. 3, pp. 546-557, 2015.
- [29] Z. Ji, X. Jiang, J. Xie, Y. Wang, and J. Ding, "Influence of bistatic shipborne HFSWOTHR platform oscillation on the sea clutter," in *Proc. 12th International Conference on Signal Processing (ICSP)*, pp. 2007-2012, 2014.
- [30] D. E. Barrick, M. W. Evans, and B. L. Weber, "Ocean surface currents mapped by radar," *Science*, vol. 198, pp. 138-144, 1977.
- [31] H. H. Essen, K. W. Gurgel, F. Schirmer, and T. Schlick, "Surface currents during NORCSEX'88, as measured by a land-and a ship-based HF-radar," in *Proc. IGARSS'89 Conference*, vol. 2, pp. 730-733, 1989.
- [32] K. W. Gurgel, "Experience with shipborne measurements of surface current fields by HF radar," *Oceanography*, vol. 10, no. 2, pp. 82-84, 1997.

- [33] K. W. Gurgel and H. H. Essen, "On the performance of a shipborne current mapping HF radar," *IEEE J. Oceanic Eng.*, vol. 25, no. 1, pp. 183-191, 2000.
- [34] R. Howell and J. Walsh, "Measurement of ocean wave spectra using a ship-mounted HF radar," *IEEE J. Oceanic Eng.*, vol. 18, no. 3, pp. 306-310, 1993.
- [35] X. Gao, and C. Zong, "Ship target detection for HF groundwave shipborne OTH radar," *IET Radar Sonar Navig.*, vol. 146, no. 6, pp. 305-311, 1999.
- [36] Z. Li, Z. Duan, J. Xie, and Y. Li, "STAP process of shipborne HFSWR motion compensation," in *Proc. 11th International Conference on Signal Processing (ICSP)*, vol. 3, pp. 1856-1860, 2012.
- [37] J. Xie, Y. Yuan, and Y. Liu, "Suppression of sea clutter with orthogonal weighting for target detection in shipborne HFSWR," *IET Radar Sonar Navig.*, vol. 149, no. 1, pp. 39-44, 2002.
- [38] J. Wang, R. Dizaji, and A.M. Ponsford, "An analysis of phase array radar system on a moving platform," in *Proc. IEEE Int. Radar Conf.*, pp. 316-320, 2005.
- [39] A. Bourges, R. Guinvarc'h, B. Uguen, and R. Gillard, "Swell compensation for high frequency antenna array on buoys," in *2006 IEEE Antennas and Propagation Society International Symposium*, pp. 4789-4792, 2006.
- [40] J. El. Khoury, A. Bourges, R. Guinvarc'h, R. Gillard, and B. Uguen, "Robustness of a correction method applied to a vertically deformed HFSWR on buoys," in *Proc. IEEE Radar Conference, Bordeaux, Oct. 2009*.
- [41] A. Bourges, R. Guinvarc'h, B. Uguen, and R. Gillard, "A simple pattern correction approach for high frequency surface wave radar on buoys," in *Proc. First European Conference on Antennas and Propagation*, pp. 1-4, 2006.

- [42] A. Bourges, R. Guinvarch, B. Uguen, and R. Gillard, "High-frequency surface wave radar based on a sea floating antenna concept," *IET Microw. Antennas Propag.*, vol. 3, no. 8, pp. 1237-1244, 2009.
- [43] J. Walsh and R. Donnelly, "A consolidated approach to two-body electromagnetic scattering problems," *Phys. Rev. A Gen. Phys.*, vol. 36, no. 9, pp. 4474-4485, 1987.
- [44] J. Walsh and E. Gill, "An analysis of the scattering of high-frequency electromagnetic radiation from rough surfaces with application to pulse radar operating in backscatter mode," *Radio Sci.*, vol. 35, no. 6, pp. 1337-1359, 2000.
- [45] R. King, "An introduction to electromagnetic surface wave propagation," *IEEE Trans. Educ.*, vol. 11, pp. 59-61, 1968.
- [46] A. M. Ponsford, "A comparison between predicted and measured sea echo Doppler spectra for surface wave radar," in *Proc. OCEANS '93*, Victoria, Canada, 1993.
- [47] A. Sommerfeld, "The propagation of waves in wireless telegraphy," *Ann. Phys.*, vol. 28, pp. 665-737, 1926.
- [48] K. Hasselmann, "On the nonlinear energy transfer in a gravity wave spectrum, part 1, general theory," *J. Fluid Mech.*, vol. 12, pp. 481-500, 1962.
- [49] E. W. Gill and J. Walsh, "Bistatic form of the electric field equations for the scattering of vertically polarized high frequency ground wave radiation from slightly rough, good conducting surfaces," *Radio Sci.*, vol. 35, no. 6, pp. 1323-1335, 2000.
- [50] Y. Ma, E. Gill, and W. Huang, "The first-order bistatic high frequency radar ocean surface cross section for an antenna on a floating platform," *IET Radar Sonar Navig.*, vol. 10, no. 6, pp. 1136-1144, 2016.
- [51] E. W. Gill and J. Walsh, "High-frequency bistatic cross sections of the ocean surface," *Radio Sci.*, vol. 36, no. 6, pp. 1459-1475, 2001.

- [52] J. Walsh and B. J. Dawe, "Development of a model for the first order bistatic ocean clutter radar cross section for ground wave radars," Northern Radar Systems Limited Contract Rep. Defence Research Establishment Ottawa, Dept. National Defence, Government of Canada, DSS Contract W7714-1-9569/01-ST, 1994.
- [53] Y. Ma, E. W. Gill, and W. Huang, "The first-order bistatic high frequency radar scattering cross section of the ocean surface for the case of floating platform," in *Proc. MTS/IEEE OCEANS*, Genova, Italy, 2015.
- [54] B. Kinsman, *Wind Waves – Their Generation and Propagation on the Ocean Surface*. New York: Courier Dover, 2002.
- [55] Y. Ma, W. Huang, and E. Gill, "The second-order bistatic high frequency radar ocean surface cross section for an antenna on a floating platform," *Can. J. Remote Sens.*, vol. 42, no. 4, pp. 332-343, 2016.
- [56] Y. Ma, W. Huang, and E. W. Gill, "The second-order bistatic high frequency radar scattering cross section of the ocean surface for the case of floating platform," in *Proc. MTS/IEEE OCEANS*, Washington DC, USA, 2015.
- [57] W. Pierson and L. Moskowitz, "A proposed spectral form for fully developed seas based upon the similarity theory of S. A. Kitaigorodskii," *J. Geophys. Res.*, vol. 69, no. 24, pp. 5181-5190, 1964.
- [58] D. E. Barrick, "FM/CW radar signals and digital processing," *NOAA Tech. Rep. ERL 283-WPL*, vol. 26, Jul. 1973.
- [59] A. Wojthiewicz, J. Misiurewicz, M. Nalecz, K. Jedrzejewski, and K. Kulpa, "Two dimensional signal processing in FMCW radars," in *Proc. Conf. on Circuit Theory and Electronics Circuits*, Kolobrzeg, Poland, pp. 474-480, Oct. 1997.

- [60] J. Walsh, J. Zhang, and E. W. Gill, "High-frequency radar cross section of the ocean surface for an FMCW waveform," *IEEE J. Ocean. Eng.*, vol. 36, no. 4, pp. 615-626, 2011.
- [61] Y. Ma, W. Huang, and E. Gill, "Bistatic high frequency radar ocean surface cross section for an FMCW source with an antenna on a floating platform," *Int. J. Antennas Propag.*, 2016.
- [62] B. J. Lipa and D. E. Barrick, "Extraction of sea state from HF radar sea echo: Mathematical theory and modelling," *Radio Sci.*, vol. 21, no. 1, pp. 81-100, 1986.
- [63] X. Chen, J. Zhang, and W. Ma, "On dynamic coupling effects between a spar and its mooring lines," *Ocean Engineering*, vol. 28, no. 7, pp: 863-887, 2001.
- [64] Y. M. Low and S. L. Robin, "A comparison of methods for the coupled analysis of floating structures," in *Proc. ASME 26th International Conference on Offshore Mechanics and Arctic Engineering*, American Society of Mechanical Engineers, 2007.
- [65] Kim, M. H., Koo, B. J., Mercier, R. M., and Ward, E. G., "Vessel/mooring/riser coupled dynamic analysis of a turret-moored FPSO compared with OTRC experiment," *Ocean Engineering*, vol. 32, no. 14, pp: 1780-1802, 2005.
- [66] Y. Ma, E. Gill, and W. Huang, "First-order high frequency radar ocean surface cross section incorporating a dual-frequency platform motion model," in *Proc. MTS/IEEE OCEANS*, Monterey, Sept. 2016.
- [67] M. Abramowitz and I. A. Stegun, *Handbook of Mathematical Functions*. New York: Dover, 1970.
- [68] Y. Ma, W. Huang, and E. W. Gill, "High frequency radar ocean surface cross section incorporating a dual-frequency platform motion model," *IEEE J. Oceanic Eng.*, 2017. (in press)

- [69] Y. Ma, E. W. Gill, and W. Huang, "Bistatic high frequency radar ocean surface cross section incorporating a dual-frequency platform motion model," *IEEE J. Oceanic Eng.*, 2017. (in press)
- [70] L. Zhang, H. Lu, J. Yang, T. Peng, and L. Xiao, "Low-frequency drift forces and horizontal motions of a moored FPSO in bi-directional swell and wind-sea offshore West Africa," *Ships Offshore Struc.*, vol. 8, no. 5, pp. 425-440, 2013.
- [71] F. E. Terman, *Radio Engineer's Handbook*. New York: McGraw-Hill, 1943.
- [72] B. J. Lipa and B. Nyden, "Directional wave information from the SeaSonde," *IEEE J. Oceanic Eng.*, vol. 30, no. 1, pp. 221-231, 2005.
- [73] E. Gill, W. Huang, and J. Walsh, "The effect of bistatic scattering angle on the high frequency radar cross sections of the ocean surface," *IEEE Geosci. Remote Sens. Lett.*, vol. 5, no. 2, pp. 143-146, 2008.
- [74] J. Walsh, B. Ryan, E. Gill, and J. El. Khoury, "Further analysis of the modulation of high frequency radar spectra due to sea-induced antenna platform motion," in *Proc. MTS/IEEE OCEANS*, Sydney, NSW, pp. 1-4, 2010.
- [75] J. Walsh, R. Howell, and B. Dawe, "Model development for evaluation studies of ground wave radar," contract report 90-C14, Cent. for Cold Ocean Resour. Eng., Mem. Univ. of Newfoundland, St. John's, Newfoundland, Canada, 1990.
- [76] E. W. Gill, Y. Ma, and W. Huang, "Motion compensation for high frequency surface wave radar on a floating platform," *IET Radar Sonar Navig.*, 2017. (in press)
- [77] Y. Ma, W. Huang, and E. W. Gill, "Motion compensation for platform-mounted high frequency surface wave radar," in *Proc. International Radar Symposium*, Prague, Czech Republic, 2017.
- [78] S. M. Riad, "The deconvolution problem: an overview," *Proc. IEEE*, vol. 74, no. 1, pp. 82-85, 1986.

- [79] S. Harsdorf and R. Reuter, "Stable deconvolution of noisy lidar signals," in *Proc. of EARSEL-SIG-Workshop LIDAR*, Dresden, June 2000.
- [80] J. Todd, "The condition of a certain matrix," *Mathematical Proceedings of the Cambridge Philosophical Society*, vol. 46, no. 01, pp. 116-118, 1950.
- [81] N. Mays, "Iterated regularization methods for solving inverse problems," Ph.D. thesis, University of Pittsburgh, USA, 2011.
- [82] S. Oraintara, W. C. Karl, D. A. Castanon, and T. Q. Nguyen, "A method for choosing the regularization parameter in generalized Tikhonov regularized linear inverse problems," in *Proc. of International Conference on Image Processing*, Vancouver, Canada, 2000.
- [83] B. Lipa, "Derivation of directional ocean-wave spectra by integral inversion of second-order radar echoes," *Radio Sci.*, vol. 12, no. 3, pp. 425-434, 1977.
- [84] E. W. Gill and J. Walsh, "A combined sea clutter and noise model appropriate to the operation of high-frequency pulsed Doppler radar in regions constrained by external noise," *Radio Sci.*, vol. 43, no. 4, pp. RS4012, 2008.
- [85] International Telecommunications Union, *Propagation in Ionized Media (ITU-R Recommendations, 1994 PI Series Volume)*, ITU, Geneva, Switzerland, 1994.
- [86] D. Barrick and J. Snider, "The statistics of HF sea-echo Doppler spectra," *IEEE Trans. Antennas Propag.*, vol. 25, no. 1, pp. 19-28, 1977.
- [87] W. Pierson, "Wind generated gravity waves," *Adv. Geophys.*, vol. 2, pp. 93-178, 1955.
- [88] H. Cao, X. Wang, Y. Liu and D. Wan, "Numerical prediction of wave loading on a floating platform coupled with a mooring system," in *Proc. of the Twenty-third International Offshore and Polar Engineering Anchorage*, Alaska, USA, 2013.

- [89] E. B. Hanssen, "Coupled analysis of a moored sevan hull by the use of OrcaFlex," Ph.D. thesis, Norwegian University of Science and Technology, Norway, 2013.
- [90] N. Bleistein and R. Handelsman, *Asymptotic Expansions of Integrals*. New York: Holt, Rinehart and Winston, 1975.
- [91] J. Walsh, "Asymptotic expansion of a Sommerfeld integral," *Electron. Lett.*, vol. 20, no. 18, 746-747, 1984.
- [92] J. Walsh and S. Srivastava, "Rough surface propagation and scatter, 1, General formulation and solution for periodic surfaces," *Radio Sci.*, vol. 22, no. 2, pp. 193-208, 1987.

# Appendix A

## A Stationary Phase Process for the First-Order Electric Field

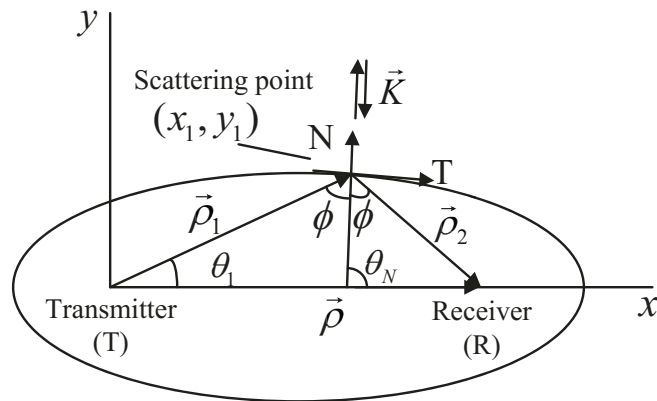


Fig. A.1 Depiction of the bistatic geometry associated with stationary phase condition.

In order to apply the stationary phase integration, an elliptic coordinate transformation should be performed. Firstly, the Cartesian  $(x, y)$  coordinate system is rotated anti-clockwise by  $\theta$  and then the origin is shifted to the center of the line segment defined by the transmitting and receiving points. The resultant Cartesian coordinate system is denoted by  $(x', y')$ , shown in A.1, where

$$\begin{aligned} x &= (x' + \frac{\rho}{2}) \cos \theta - y' \sin \theta, \\ y &= (x' + \frac{\rho}{2}) \sin \theta + y' \cos \theta. \end{aligned} \tag{A.1}$$

Then, the elliptic coordinate  $(\mu, \nu)$  can be defined in terms of  $(x', y')$  by using  $x' = \frac{\rho}{2} \cosh \mu \cos \nu$  and  $y' = \frac{\rho}{2} \sinh \mu \sin \nu$ . Thus,

$$\begin{aligned}
x_1 &= \frac{\rho}{2} [(1 + \cosh \mu \cos \nu) \cos \theta - \sinh \mu \sin \nu \sin \theta] \\
y_1 &= \frac{\rho}{2} [(1 + \cosh \mu \cos \nu) \sin \theta + \sinh \mu \sin \nu \cos \theta] \\
\rho_1 &= \frac{\rho}{2} (\cosh \mu + \cos \nu) \\
\rho_2 &= \frac{\rho}{2} (\cosh \mu - \cos \nu) \\
\theta_1 &= \tan^{-1} \left( \frac{y_1}{x_1} \right) = \tan^{-1} \left[ \frac{(1 + \cosh \mu \cos \nu) \sin \theta + \sinh \mu \sin \nu \cos \theta}{(1 + \cosh \mu \cos \nu) \cos \theta - \sinh \mu \sin \nu \sin \theta} \right] \\
dx_1 dy_1 &= \rho_1 \rho_2 d\mu d\nu.
\end{aligned} \tag{A.2}$$

Since  $x_1 = \rho_1 \cos \theta_1$  and  $y_1 = \rho_1 \sin \theta_1$ ,  $\cos(\theta_1 - \theta_K)$  in the exponential term of (1.2) can be expanded as

$$e^{j\rho_1 K \cos(\theta_1 - \theta_K)} = e^{j\frac{\rho}{2} K [(1 + \cosh \mu \cos \nu) \cos(\theta_K - \theta) + \sinh \mu \sin \nu \sin(\theta_K - \theta)]}. \tag{A.3}$$

In view of these transformations, (1.2) reduces to

$$\begin{aligned}
(E_n)_1 &\approx \frac{kC_0}{(2\pi)^2} \sum_{\bar{K}} P_{\bar{K}} K \int_0^{2\pi} \int_0^\infty \cos(\theta_1 - \theta_K) F(\rho_1) F(\rho_2) e^{jk\delta\rho_0 \cos(\theta_1 - \theta_0)} \\
&\quad \cdot e^{j\frac{\rho K}{2} [(1 + \cosh \mu \cos \nu) \cos(\theta_K - \theta) + \sinh \mu \sin \nu \sin(\theta_K - \theta)]} e^{-jk(\rho_1 + \rho_2)} d\mu d\nu.
\end{aligned} \tag{A.4}$$

From (A.2), it may be observed that  $\rho_1 + \rho_2 = \rho \cosh \mu$ , which means the scattering ellipse is determined by the value of  $\mu$ , if  $\rho$ , the distance between the transmitter and the receiver, is fixed. Then, (A.4) can be written as

$$\begin{aligned}
(E_n)_1 &\approx \frac{kC_0}{(2\pi)^2} \sum_{\bar{K}} P_{\bar{K}} K e^{j\frac{\rho K}{2} \cos(\theta_K - \theta)} \int_0^\infty e^{-jk\rho \cosh \mu} \int_0^{2\pi} \cos(\theta_1 - \theta_K) F(\rho_1) F(\rho_2) \\
&\quad \cdot e^{j\frac{\rho}{2} K [\cosh \mu \cos \nu \cos(\theta_K - \theta) + \sinh \mu \sin \nu \sin(\theta_K - \theta)]} e^{jk\delta\rho_0 \cos(\theta_1 - \theta_0)} d\nu d\mu.
\end{aligned} \tag{A.5}$$

Next, the  $v$  integral in (A.5) may be defined as

$$I(\mu) = \int_0^{2\pi} \cos(\theta_1 - \theta_K) F(\rho_1) F(\rho_2) \cdot e^{j\frac{\rho}{2}K[\cosh\mu \cos v \cos(\theta_K - \theta) + \sinh\mu \sin v \sin(\theta_K - \theta)]} e^{jk\delta\rho_0 \cos(\theta_1 - \theta_0)} dv. \quad (\text{A.6})$$

For bistatic operation,  $\rho$  is usually several tens of kilometers. Then,  $\frac{\rho}{2}K$  in the phase term will be a large value for a wide range of  $K$ . Also, it is known that for highly conductive surfaces, the values of  $F(\rho_1)$  and  $F(\rho_2)$  are slowly varying. Moreover,  $\delta\rho_0$  is a very small quantity compared to the other distance parameters. Under these conditions, (A.6) can be solved by the stationary phase method [90]. After applying the stationary phase integration, (A.6) reduces to

$$I(\mu) \approx \sqrt{2\pi} \cos(\theta_1 - \theta_K) F(\rho_1) F(\rho_2) e^{jk\delta\rho_0 \cos(\theta_1 - \theta_0)} \cdot e^{j\frac{\rho}{2}K[\cosh\mu \cos v \cos(\theta_K - \theta) + \sinh\mu \sin v \sin(\theta_K - \theta)]} \cdot \left\{ j\frac{\rho}{2}K[\cosh\mu \cos v \cos(\theta_K - \theta) + \sinh\mu \sin v \sin(\theta_K - \theta)] \right\}^{-\frac{1}{2}} \quad (\text{A.7})$$

with the stationary phase points given by

$$\tan v_s = \tanh \mu \tan(\theta_K - \theta). \quad (\text{A.8})$$

A final asymptotic form for  $I(\mu)$  may be written as

$$I(\mu) \approx \sqrt{2\pi} (\pm \sqrt{\cos \phi}) \frac{F(\rho_1) F(\rho_2)}{\sqrt{K\rho_s}} e^{jk\delta\rho_0 \cos(\theta_1 - \theta_0)} e^{\pm jK\rho_s \cos \phi} e^{\mp j\frac{\pi}{4}} \quad (\text{A.9})$$

where  $\rho_s = \frac{\rho_1 + \rho_2}{2} = \frac{\rho}{2} \cosh \mu$ . Gill [49] shows that the surface wavenumber,  $\vec{K}$ , is normal to the scattering ellipse (i.e.  $\theta_N = \theta_K$ ) and the ellipse normal bisects the angle between the transmitter and receiver, as viewed from the scattering point.  $\phi$  is the bistatic angle,

defined as each portion of this bisection, shown in Fig. A.1. Furthermore,

$$\begin{aligned}\cos(\theta_1 - \theta_0) &= \cos(\theta_K - \phi - \theta_0) \\ &= \cos \phi \cos(\theta_K - \theta_0) + \sin \phi \sin(\theta_K - \theta_0).\end{aligned}\tag{A.10}$$

Then, (A.9) may be written as

$$\begin{aligned}I(\mu) &\approx \sqrt{2\pi}(\pm\sqrt{\cos\phi})\frac{F(\rho_1)F(\rho_2)}{\sqrt{K\rho_s}}e^{\pm jK\rho_s\cos\phi} \\ &\cdot e^{\mp j\frac{\pi}{4}}e^{jk\delta\rho_0[\cos\phi\cdot\cos(\theta_K-\theta_0)+\sin\phi\cdot\sin(\theta_K-\theta_0)]}.\end{aligned}\tag{A.11}$$

Substituting (A.11) into (A.5) gives

$$\begin{aligned}(E_n)_1 &\approx \frac{kC_0}{(2\pi)^{3/2}}\sum_{\vec{K}}P_{\vec{K}}\sqrt{K}e^{j\frac{\rho_K}{2}\cos(\theta_K-\theta)} \\ &\cdot \int_0^\infty e^{-jk\rho\cosh\mu}e^{\mp j\frac{\pi}{4}}(\pm\sqrt{\cos\phi})\frac{F(\rho_1)F(\rho_2)}{\sqrt{\rho_s}} \\ &\cdot e^{jk\delta\rho_0[\cos\phi\cos(\theta_K-\theta_0)+\sin\phi\sin(\theta_K-\theta_0)]}e^{\pm jK\rho_s\cos\phi}d\mu.\end{aligned}\tag{A.12}$$

From the definition of  $\rho_s$ , it can be readily deduced that  $d\mu = \frac{1}{\sqrt{\rho_s^2 - (\rho/2)^2}}d\rho_s$ . Changing the  $\mu$  integration to a  $\rho_s$  integration gives

$$\begin{aligned}(E_n)_1 &\approx \frac{kC_0}{(2\pi)^{3/2}}\sum_{\vec{K}}P_{\vec{K}}\sqrt{K}e^{j\frac{\rho_K}{2}\cos(\theta_K-\theta)}\int_{\rho/2}^\infty \frac{F(\rho_1)F(\rho_2)}{\sqrt{\rho_s[\rho_s^2 - (\rho/2)^2]}}e^{\mp j\frac{\pi}{4}}(\pm\sqrt{\cos\phi}) \\ &\cdot e^{jk\delta\rho_0[\cos\phi\cos(\theta_K-\theta_0)+\sin\phi\sin(\theta_K-\theta_0)]}e^{j\rho_s[\pm K\cos\phi - 2k]}d\rho_s.\end{aligned}\tag{A.13}$$

## Appendix B

### $\langle M(K, \theta_K, \tau, t) \rangle$ for a Sinusoidal Antenna Motion Model

It is assumed that the sway motion  $\vec{\delta\rho}_0 = a \sin(\omega_p t) \hat{\rho}_p$  is caused by the dominant ocean wave. The sway frequency can be expressed as  $\omega_p = \sqrt{gK_p}$ , where  $K_p$  is the dominant ocean wavenumber, and  $a$  is the sway amplitude depending on the sea state. In addition,  $\omega_p$  and  $a$  are assumed to be constant during the sets of observations. Thus,

$$\begin{aligned}
 M(K, \theta_K, \tau, t) &= e^{j \frac{aK \cos(\theta_K - \theta_{K_p})}{2} [-\sin(\omega_p t) + \sin(\omega_p t + \omega_p \tau)]} \\
 &\cdot e^{j \frac{aK \tan \phi_0 \sin(\theta_K - \theta_{K_p})}{2} [-\sin(\omega_p t) + \sin(\omega_p t + \omega_p \tau)]} \\
 &= e^{jv \cos(\phi_p + \phi_1)}
 \end{aligned} \tag{B.1}$$

where

$$\begin{aligned}
 v &= aK [\cos(\theta_K - \theta_{K_p}) + \tan \phi_0 \sin(\theta_K - \theta_{K_p})] \sin\left(\frac{1}{2} \omega_p \tau\right) \\
 \phi_p &= \omega_p t \\
 \phi_1 &= \frac{1}{2} \omega_p \tau.
 \end{aligned} \tag{B.2}$$

Here, the Bessel function  $J_n$  of the first kind of order  $n$  is introduced and may be expressed as

$$J_n(z) = \frac{j^{-n}}{2\pi} \int_0^{2\pi} e^{jz \cos \theta} \cos(n\theta) d\theta \quad (\text{B.3})$$

where  $n$  can be any integer. The graphs of Bessel functions look roughly like oscillating sine or cosine functions that decay proportionally as  $1/\sqrt{z}$ . Again, using the definition of the zero-order Bessel function of the first kind, (B.1) reduces to

$$\begin{aligned} \langle M(K, \theta_K, \tau, t) \rangle &= \frac{1}{2\pi} \int_0^{2\pi} e^{jv \cos(\phi_p + \phi_1)} d\phi_p \\ &= \frac{1}{2\pi} \int_0^{2\pi} e^{jv \cos \mu} d\mu \\ &= J_0(v) \\ &= J_0\{aK[\cos(\theta_K - \theta_{K_p}) + \tan \phi_0 \sin(\theta_K - \theta_{K_p})] \sin(\frac{1}{2}\omega_p \tau)\}. \end{aligned} \quad (\text{B.4})$$

Considering the properties of the Bessel function, it can be shown that [17]

$$J_0[2x \sin(\frac{\phi}{2})] = J_0^2(x) + 2 \sum_{n=1}^{\infty} J_n^2(x) \cos(n\phi)$$

For the problem here, it can be observed that  $x = \frac{1}{2}aK[\cos(\theta_K - \theta_{K_p}) + \tan \phi_0 \sin(\theta_K - \theta_{K_p})]$  and  $\phi = \omega_p \tau$ . Thus,

$$\begin{aligned} \langle M(K, \theta_K, \tau, t) \rangle &= \\ &J_0^2\left\{\frac{aK}{2}[\cos(\theta_K - \theta_{K_p}) + \tan \phi_0 \sin(\theta_K - \theta_{K_p})]\right\} \\ &+ 2 \sum_{n=1}^{\infty} J_n^2\left\{\frac{aK}{2}[\cos(\theta_K - \theta_{K_p}) + \tan \phi_0 \sin(\theta_K - \theta_{K_p})]\right\} \cdot \cos(n\omega_p \tau). \end{aligned} \quad (\text{B.5})$$

## Appendix C

# A Stationary Phase Process for the Second-Order Electric Field

For the present analysis, it is useful to write (2.41) in elliptic coordinates  $(\mu, \delta)$  and to this end we note

$$\begin{aligned}\rho_2 &= \frac{\rho}{2}(\cosh \mu + \cos \delta) \\ \rho_{20} &= \frac{\rho}{2}(\cosh \mu - \cos \delta) \\ \rho_2 + \rho_{20} &= \rho \cosh \mu \\ x_2 &= \rho_2 \cos \theta_2 = \frac{\rho}{2}[(1 + \cosh \mu \cos \delta) \cos \theta - \sinh \mu \sin \delta \sin \theta] \\ y_2 &= \rho_2 \sin \theta_2 = \frac{\rho}{2}[(1 + \cosh \mu \cos \delta) \sin \theta + \sinh \mu \sin \delta \cos \theta] \\ \theta_2 &= \tan^{-1}\left(\frac{y_2}{x_2}\right) = \tan^{-1}\left[\frac{(1 + \cosh \mu \cos \delta) \sin \theta + \sinh \mu \sin \delta \cos \theta}{(1 + \cosh \mu \cos \delta) \cos \theta - \sinh \mu \sin \delta \sin \theta}\right] \\ dx_2 dy_2 &= \rho_2 \rho_{20} d\mu d\delta.\end{aligned}\tag{C.1}$$

With these transformations, it is straightforward to show that

$$\begin{aligned}K\rho_2 \cos(\theta_K - \theta_2) \\ = \frac{\rho}{2}K[\cos(\theta_K - \theta) + \cosh \mu \cos \delta \cos(\theta_K - \theta) + \sinh \mu \sin \delta \sin(\theta_K - \theta)]\end{aligned}\tag{C.2}$$

so that (2.41) may be written as

$$\begin{aligned}
(E_n)_{2bf} \approx & -\frac{kC_0}{(2\pi)^2} \sum_{\vec{K}_1} \sum_{\vec{K}_2} P_{\vec{K}_1} P_{\vec{K}_2} e^{j\frac{\rho}{2}K \cos(\theta_K - \theta)} \int_0^\infty e^{-jk\rho \cosh \mu} \\
& \cdot \int_0^{2\pi} (-k\chi) e^{jk\delta \vec{\rho}_0 \cdot \hat{\rho}_2} e^{j\frac{\rho}{2}K [\cosh \mu \cos \delta \cos(\theta_K - \theta) + \sinh \mu \sin \delta \sin(\theta_K - \theta)]} \\
& \cdot F(\rho_2) F(\rho_{20}) d\delta d\mu.
\end{aligned} \tag{C.3}$$

Then, a stationary phase approach may be used to reduce (C.3) to a single integration.

Setting

$$Z = \frac{\rho}{2} K$$

and noting

$$\begin{aligned}
F(\delta) &= (-k\chi) e^{jk\delta \vec{\rho}_0 \cdot \hat{\rho}_2} F(\rho_2) F(\rho_{20}) \\
f(\delta) &= \cosh \mu \cos \delta \cos(\theta_K - \theta) + \sinh \mu \sin \delta \sin(\theta_K - \theta),
\end{aligned}$$

the stationary phase points may be shown to be given by

$$\tan \delta_s = \tanh \mu \tan(\theta_K - \theta). \tag{C.4}$$

Thus, the inner integral in (C.3) may be written as

$$\begin{aligned}
I_\delta \approx & \sqrt{2\pi} (-k\chi) F(\rho_2) F(\rho_{20}) e^{jk\delta \vec{\rho}_0 \cdot \hat{\rho}_2} \\
& \cdot \frac{e^{j\frac{\rho}{2}K [\cosh \mu \cos \delta \cos(\theta_K - \theta) + \sinh \mu \sin \delta \sin(\theta_K - \theta)]}}{\sqrt{j\frac{\rho}{2}K [\cosh \mu \cos \delta \cos(\theta_K - \theta) + \sinh \mu \sin \delta \sin(\theta_K - \theta)]}}.
\end{aligned} \tag{C.5}$$

Following the same analysis as in [49], (C.5) may be reduced to

$$I_\delta \approx \sqrt{2\pi} \frac{(-k\chi) F(\rho_2) F(\rho_{20})}{\sqrt{K\rho_s \cos \phi}} e^{jk\delta \vec{\rho}_0 \cdot \hat{\rho}_2} e^{\pm jK\rho_s \cos \phi} e^{\mp j\frac{\pi}{4}} \tag{C.6}$$

where  $\rho_s = \frac{\rho_2 + \rho_{20}}{2}$ . Since

$$\begin{aligned}
\delta \hat{\rho}_0 \cdot \hat{\rho}_2 &= \cos(\theta_2 - \theta_0) \\
&= \cos(\theta_K - \phi - \theta_0) \\
&= \cos \phi \cos(\theta_K - \theta_0) + \sin \phi \sin(\theta_K - \theta_0)
\end{aligned} \tag{C.7}$$

(C.3) may be written as

$$\begin{aligned}
(E_n)_{2bf} &\approx \frac{-kC_0}{(2\pi)^{\frac{3}{2}}} \sum_{\vec{K}_1} \sum_{\vec{K}_2} P_{\vec{K}_1} P_{\vec{K}_2} e^{j\frac{\rho}{2}K \cos(\theta_K - \theta)} \int_0^\infty e^{-jk\rho \cosh \mu} \frac{(-k\chi)F(\rho_2)F(\rho_{20})}{\sqrt{K\rho_s \cos \phi}} \\
&\cdot e^{jk\delta\rho_0[\cos \phi \cos(\theta_K - \theta_0) + \sin \phi \sin(\theta_K - \theta_0)]} e^{\pm jK\rho_s \cos \phi} e^{\mp j\frac{\pi}{4}} d\mu.
\end{aligned} \tag{C.8}$$

Also, because  $\rho_s = \frac{\rho_2 + \rho_{20}}{2} = \frac{\rho}{2} \cosh \mu$  and  $d\rho_s = \frac{\rho}{2} \sinh \mu d\mu = \sqrt{\rho_s^2 - (\frac{\rho}{2})^2} d\mu$ , (C.8)

becomes

$$\begin{aligned}
(E_n)_{2bf} &= \frac{-kC_0}{(2\pi)^{\frac{3}{2}}} \sum_{\vec{K}_1} \sum_{\vec{K}_2} \frac{P_{\vec{K}_1} P_{\vec{K}_2}}{\sqrt{K}} e^{j\frac{\rho}{2}K \cos(\theta_K - \theta)} e^{\mp j\frac{\pi}{4}} \\
&\cdot \int_{\frac{\rho}{2}}^\infty \frac{(-k\chi)F(\rho_2)F(\rho_{20})}{\sqrt{\cos \phi}} \frac{e^{j\rho_s(\pm K \cos \phi - 2k)}}{\sqrt{\rho_s(\rho_s^2 - (\frac{\rho}{2})^2)}} \\
&\cdot e^{jk\delta\rho_0[\cos \phi \cos(\theta_K - \theta_0) + \sin \phi \sin(\theta_K - \theta_0)]} d\rho_s.
\end{aligned} \tag{C.9}$$

## Appendix D

### Symmetrical Coupling Coefficient

In order to derive a symmetrical electromagnetic coupling coefficient for (2.45), it is worthwhile to consider  $G[K_s(\hat{\rho}_2, \vec{K}_1)]$ , appearing in the  $\chi$  of (2.41), in more detail. Since  $F(\rho_{12})$  varies slowly with  $\rho_{12}$ ,  $\frac{d}{d\rho_{12}}[F(\rho_{12})]$  may be assumed to be negligible. Thus,

$$\begin{aligned}
 G[K_s(\hat{\rho}_2, \vec{K}_1)] &= \int_{\rho_{12}} F(\rho_{12}) e^{-jk\rho_{12}} J_1(\rho_{12}K_s) d\rho_{12} \\
 &= -\frac{1}{K_s} \int_{\rho_{12}} F(\rho_{12}) e^{-jk\rho_{12}} \frac{d}{d\rho_{12}} [J_0(\rho_{12}K_s)] d\rho_{12} \\
 &= -\frac{1}{K_s} \{ F(\rho_{12}) e^{-jk\rho_{12}} J_0(\rho_{12}K_s) |_0^\infty - \int_0^\infty \frac{d}{d\rho_{12}} [F(\rho_{12}) e^{-jk\rho_{12}}] J_0(\rho_{12}K_s) d\rho_{12} \} \\
 &= \frac{1}{K_s} \{ 1 - jk \int_0^\infty F(\rho_{12}) e^{-jk\rho_{12}} J_0(\rho_{12}K_s) d\rho_{12} \}.
 \end{aligned} \tag{D.1}$$

In [91], it is shown that  $\mathcal{F}[F(\rho) \frac{e^{-jk\rho}}{2\pi\rho}] = \frac{1}{u_0 + \frac{u_1}{n_0^2}}$ , where  $\mathcal{F}$  represents Fourier transformation,  $u_0 = \sqrt{K^2 - k^2}$ ,  $u_1 = \sqrt{K^2 - n_0^2 k^2}$ ,  $n_0^2 = \epsilon_r - j\frac{\sigma}{\omega\epsilon_0}$ , and  $n_0$  and  $\epsilon_r$  are the refractive index and the relative permittivity, respectively. For a good conducting surface (see [92]),

$$u_1 = \sqrt{K^2 - n_0^2 k^2} \sim jkn_0. \tag{D.2}$$

Defining a parameter  $\Delta = \frac{1}{n_0}$  as the intrinsic impedance of the surface gives

$$\mathcal{F}\left[F(\rho)\frac{e^{-jk\rho}}{2\pi\rho}\right] \approx \frac{1}{u_0 + jk\Delta}. \quad (\text{D.3})$$

Recalling that the zero-order Bessel function of the first kind may be defined as

$$J_0(z) = \frac{1}{2\pi} \int_0^{2\pi} e^{jz \cos \alpha} d\alpha, \quad (\text{D.4})$$

(D.3) becomes

$$\begin{aligned} \mathcal{F}\left[F(\rho)\frac{e^{-jk\rho}}{2\pi\rho}\right] &= \int_x \int_y F(\rho)\frac{e^{-jk\rho}}{2\pi\rho} e^{-jk_x x - jk_y y} dx dy \\ &= \frac{1}{2\pi} \int_0^\infty F(\rho) e^{-jk\rho} \int_0^{2\pi} e^{-jK\rho \cos(\phi_\rho - \theta_K)} d\phi_\rho d\rho \\ &= \int_0^\infty F(\rho) e^{-jk\rho} J_0(\rho K) d\rho \end{aligned} \quad (\text{D.5})$$

where  $\phi_\rho$  and  $\theta_K$  are directions of  $\vec{\rho} = (x, y)$  and  $\vec{K} = (k_x, k_y)$ , respectively. By applying (D.3), (D.5) to the integral in (D.1),

$$\int_0^\infty F(\rho_{12}) e^{-jk\rho_{12}} J_0(\rho_{12} K_s) d\rho_{12} = \frac{1}{u_0 + jk\Delta} = \frac{1}{\sqrt{K_s^2 - k^2} + jk\Delta}. \quad (\text{D.6})$$

Inserting (D.6) into (D.1) gives

$$G[K_s(\hat{\rho}_2, \vec{K}_1)] = \frac{1}{K_s} \left\{ 1 - \frac{jk}{\sqrt{K_s^2 - k^2} + jk\Delta} \right\}. \quad (\text{D.7})$$

$G[K_s(\hat{\rho}_2, \vec{K}_1)]$  should be zero when  $K_s$  approaches zero. In keeping with the same argument as for the time-varying electric field with a pulsed dipole source in [17], (D.7) can be modified as

$$G[K_s(\hat{\rho}_2, \vec{K}_1)] = \frac{1}{K_s} \left\{ 1 - j \frac{k_0(1 + \Delta)}{\sqrt{K_s^2 - k_0^2} + jk_0\Delta} \right\} \quad (\text{D.8})$$

Seeking a symmetrical form of the electromagnetic coupling coefficient  ${}_E\Gamma_P$  with respect to  $\vec{K}_1$  and  $\vec{K}_2$ , an expression for the symmetrical electromagnetic coupling coefficient can be written as

$$\begin{aligned}
& {}_{SE}\Gamma_P(\vec{K}_1, \vec{K}_2) \\
&= \frac{1}{2} [{}_E\Gamma_P(\vec{K}_1, \vec{K}_2) + {}_E\Gamma_P(\vec{K}_2, \vec{K}_1)] \\
&= \frac{jk_0}{2K \cos \phi_0} \{ (\vec{K}_1 \cdot \hat{\rho}_2) \\
&\quad \cdot [\hat{K}_s(\hat{\rho}_2, \vec{K}_1) \cdot \vec{K}_2] G[K_s(\hat{\rho}_2, \vec{K}_1)] + (\vec{K}_2 \cdot \hat{\rho}_2) [\hat{K}_s(\hat{\rho}_2, \vec{K}_2) \cdot \vec{K}_1] G[K_s(\hat{\rho}_2, \vec{K}_2)] \}
\end{aligned} \tag{D.9}$$

where  $\vec{K}_s(\hat{\rho}_2, \vec{K}_2) = k\hat{\rho}_2 - \vec{K}_2$ , with  $\hat{K}_s(\hat{\rho}_2, \vec{K}_2)$  and  $K_s(\hat{\rho}_2, \vec{K}_2)$ , respectively, being the direction and magnitude of  $\vec{K}_s(\hat{\rho}_2, \vec{K}_2)$ .